

EVALUATION OF DIFFERENT GNSS SOLUTIONS AND SFM SOFTWARE
WORKFLOWS FOR SURVEYING SHORELINES AND REMOTE AREAS USING UAS

A Thesis

by

JOSÉ ABEL PILARTES-CONGO JR

BS, Texas A&M University-Corpus Christi, 2020

Submitted in Partial Fulfillment of the Requirements for the Degree of

MASTER OF SCIENCE

in

GEOSPATIAL SYSTEMS ENGINEERING

Texas A&M University-Corpus Christi
Corpus Christi, Texas

May 2022

© José Abel Pilartes-Congo Jr

All Rights Reserved

May 2022

EVALUATION OF DIFFERENT GNSS SOLUTIONS AND SFM SOFTWARE
WORKFLOWS FOR SURVEYING SHORELINES AND REMOTE AREAS USING UAS

A Thesis

by

JOSÉ ABEL PILARTES-CONGO JR

This thesis meets the standards for scope and quality of
Texas A&M University-Corpus Christi and is hereby approved.

Michael J. Starek, PhD
Chair

Tianxing Chu, PhD
Committee Member

Yuxia Huang, PhD
Committee Member

May 2022

ABSTRACT

The emergence and modernization of Unoccupied Aircraft Systems (UAS), broadly known as drones, and Structure-from-Motion (SfM) photogrammetry have made significant contributions to the geospatial and surveying world. Traditionally, indirect georeferencing by using ground control points (GCPs) is used to georeference UAS imagery when high accuracy positioning is required. However, this approach is tedious and impractical when surveying remote or inaccessible coastal areas, or when desiring to map coastlines from shipborne UAS operations. The broad applicability of UAS and SfM technologies has led to a wide range of data collection and SfM processing workflows that can be utilized, enhanced further by the implementation of various Global Navigation Satellite Systems (GNSS) techniques for direct georeferencing of the imagery.

As part of an investigation conducted by the Office of Coast Survey (OCS) at the National Oceanic and Atmospheric Administration (NOAA), this study seeks to identify UAS-SfM data collection and processing workflows that maintain vertical accuracies at the decimeter-level without the aiding of GCPs. The study uses UAS imagery collected from two different UAS platforms at two different sandy beach study sites along the Southern Texas Gulf Coast. The objectives of the study are two-fold: (i) examine the applicability of Real-Time Kinematic (RTK), Post-Processed Kinematic (PPK), and Precise Point Positioning (PPP) GNSS solutions as plausible substitutes to ground control points (GCPs) for UAS-SfM shoreline mapping, and (ii) to evaluate the impact of three-commercial SfM software (Drone2Map, Metashape, and Pix4D) and one open-source software (Web OpenDroneMap) on the quantitative and qualitative characteristics of resulting mapping products.

Results showed that RTK and PPK can reach centimeter-level vertical accuracies, fulfill the requirements set forth for this project, and are the most suitable alternatives to GCPs for remote surveying when plausible. When using PPK, the highest accuracies were reached when using base stations within 30 kilometers of the survey site, especially when combined with higher percentages of PPK fix, a measure that explains the number of photos that successfully underwent PPK correction. PPP offers the best alternative for remote UAS surveying, given that it is a single-receiver method, but the results evaluated here did not meet desired vertical accuracy levels. However, enhancing convergence time techniques is likely to reach even better results. In terms of SfM software, Metashape and Pix4D proved to be the most robust software alternatives achieving repeatable centimeter-level vertical accuracies for derived mapping products. Several inconsistencies were observed with Drone2Map and ODM, which hinder its applicability for UAS surveying without GCPs.

The results and techniques discussed in this study help to optimize data acquisition and processing workflows for shoreline mapping and remote surveying.

DEDICATION

Self-determination alone would not have been enough to complete this project without the support of many great people. I dedicate this work to the Pilartes-Congo family (particularly to my parents Pilartes Sr. and Elisa) and Analtina for their unconditional support and motivation throughout this journey.

ACKNOWLEDGEMENTS

First and foremost, I want to thank Dr. Michael John Starek for his belief in me from the very beginning. Without his valuable mentorship, patience, and leadership, I could not have made it this far. His unparalleled expertise, excitement toward remote sensing, and advocacy for exposing students to fieldwork were determining factors in my decision to pursue graduate school at TAMUCC. To have come this far under his supervision has truly been a blessing.

I am also extremely grateful to Dr. Tianxing Chu and Dr. Yuxia Huang, who not only agreed without hesitation to serve as my committee members but also offered their guidance and assistance throughout my undergraduate and graduate journey at TAMUCC. I have been fortunate to not only work or take classes under their supervision but also learn about their passion for nature exploration and sports such as soccer and tennis.

Furthermore, a special thanks to Mr. Jacob Berryhill for all his help during my data acquisition and processing phases. The experience and opinions he shared certainly played a significant role in my learning. Words could not describe my gratitude to the entire Conrad Blucher Institute for their ongoing confidence in me since 2016. I have always given my best to represent the institute to the best of my ability, but no amount of effort suffices the learning that took place in all these years. Within the institute, I want to thank the MANTIS team for their warm reception of me during the beginning and for being always there to provide feedback on my methods.

Lastly, I want to acknowledge the Office of Coast Survey at NOAA for funding this project under contract number NCNJ1000-20-0123, allowing me to be part of their efforts to optimize coastal and shoreline mapping. My greatest desire is to make these efforts more achievable by my contributions to this project.

TABLE OF CONTENTS

	Page
ABSTRACT.....	iv
DEDICATION.....	vi
ACKNOWLEDGEMENTS	vii
TABLE OF CONTENTS.....	viii
LIST OF FIGURES	xiii
LIST OF TABLES	xix
CHAPTER I INTRODUCTION.....	1
1.1. Background.....	1
1.2. Summary of Objectives.....	1
1.3. Motivation	2
CHAPTER II REVIEW OF THE LITERATURE	4
CHAPTER III METHODOLOGY	14
3.1. Hardware	14
3.1.1. WingtraOne PPK UAS.....	14
3.1.2. DJI Phantom 4 RTK	16
3.1.3. Ground Control Targets	17
3.1.4. GNSS Receiver.....	18
3.1.5. Terrestrial Laser Scanner	19
3.1.6. TS15 P1 Robotic Total Station	20
3.1.7. Computational Hardware	21
3.2. Software.....	21

3.2.1. Software (GNSS Evaluation).....	21
3.2.2. Software (SfM Processing Evaluation)	21
3.3. Study Sites.....	22
3.3.1. North Packery Channel (September 4, 2020).....	22
Location.....	22
UAS Flight.....	23
Ground Control	24
3.3.2. Mustang Island State Park (July 13, 2021).....	25
Location.....	25
UAS Flights	26
Ground Control – RTK GNSS vs Total Station.....	27
SurvNET: Total Station (Least Squares Adjustment)	28
GNSS Planning	30
Ground Control – Terrestrial Laser Scanner.....	32
3.3.3. UAS Access Permission and Adherence to Laws	33
3.4. Study Limitations and Assumptions	33
3.5. Safety and Risk	34
3.6. Datasets	34
3.7. Methodology for GNSS Evaluation.....	34
3.7.1. Overview.....	34
3.7.2. Performance of the PPK Georeferencing Technique.....	35
PPK Workflow with Wingtra.....	35
Distance of Base Station	39

Observation Rate of Base Station	42
PPK Workflow with DJI Phantom 4 RTK	43
3.7.3. Performance of the RTK Georeferencing Technique	44
3.7.4. Performance of the PPP Georeferencing Technique	44
3.7.5. Data Processing.....	47
3.7.6. Accuracy Evaluation.....	47
3.8. Methodology for SfM Software Evaluation	49
3.8.1. Overview.....	49
3.8.2. Agisoft Metashape.....	49
3.8.3. Pix4Dmapper.....	50
3.8.4. Drone2Map	51
3.8.5. OpenDroneMap	52
3.8.6. Accuracy Evaluation.....	55
CHAPTER IV RESULTS AND DISCUSSION.....	57
4.1. GNSS Georeferencing Techniques	57
4.1.1. PPK Evaluation Results – WingtraOne UAS.....	57
Distance of Base Station	57
Observation Rate and PPK Fix Percentage	59
RTK GNSS vs Total Station	61
4.1.2. PPK Evaluation Results – DJI Phantom 4 RTK.....	63
4.1.3. RTK Evaluation Results.....	63
4.1.4. PPP Evaluation.....	63
4.1.5. Supplementary Results.....	66

DSM of Differences.....	66
DSM vs RTK GNSS.....	68
Autonomous vs GCPs.....	69
4.1.6. Summary of Results (GNSS Techniques).....	70
4.2. SfM Processing Software.....	72
4.2.1. Results Using Dataset from North Packery Channel (September 04, 2020)	72
4.2.2. Results Using Dataset from Mustang Island State Park (July 13, 2021).....	76
4.2.3. Summary of Results (SfM Software Comparison).....	79
CHAPTER V SUMMARY OF LESSONS LEARNED	82
5.1. Lessons Learned from GNSS Evaluation.....	82
5.2. Lessons Learned from SfM Software Evaluation	86
CHAPTER VI CONCLUSION AND FUTURE WORK.....	89
6.1. Conclusion.....	89
6.2. Recommendations.....	90
6.3. Future work.....	91
REFERENCES.....	92
APPENDIX A FIELD NOTES AND SUMMARY OF WORKFLOW	102
APPENDIX B GNSS DATA PREPARATION	106
APPENDIX C WINGTRAHUB OUTPUT FORMATS AND PROCESSING REPORTS	108
APPENDIX D PPK PROCESSING	113
APPENDIX E PRECISE POINT POSITIONING	117
APPENDIX F HEIGHT TRANSECT DIFFERENCES	120
APPENDIX G MULTI-STATION ADJUSTMENT REPORT	121

APPENDIX H UAS GENERATED DTMS, ORTHOMOSAICS, AND POINT CLOUDS	127
APPENDIX I PROCESSING REPORTS FROM SFM SOFTWARE	133

LIST OF FIGURES

	Page
Figure 1. Summary of the SfM workflow (Starek et al., 2019).....	5
Figure 2. WingtraOne UAS PPK platform (left) and as captured during the field survey (right).15	15
Figure 3. Action captures from operating the WingtraHub in a coastal environment.....	15
Figure 4. DJI Phantom 4 RTK platform.....	17
Figure 5. Example of a ground control target used during the survey.	18
Figure 6. Septentrio NR3 receiver static setup (left-most and middle) and Allegro data collector (right-most).....	19
Figure 7. Riegl VZ-2000i TLS.	20
Figure 8. TS15 P1 total station (left three) and reflector (right-most) used to survey the targets.20	20
Figure 9. Location of North Packery Channel.	23
Figure 10. Ground control distribution at North Packery Channel (~ 500 m spacing).....	24
Figure 11. Location of Mustang Island State Park.	25
Figure 12. Ground control distribution at Mustang Island State Park (~ 20 m spacing).	27
Figure 13. Differences between total station and RTK measured heights (absolute values).	30
Figure 14. DOP values during the survey period (source: Trimble GNSS Planning).....	31
Figure 15. Satellite availability during the survey period (source: Trimble GNSS Planning).	31
Figure 16. Workflow used for GNSS solutions experiments.	35
Figure 17. Screen capture of the WingtraHub interface.	36
Figure 18. Example of base file import in WingtraHub.	37
Figure 19. Coordinate information used in WingtraHub for the local base in this project.	38

Figure 20. Example of a WingtraHub processing report (using the local base, 30s sampling rate, GLONASS, and GPS navigation files, with the WingtraOne UAS flight at 120 m AGL).....	39
Figure 21. Local base and remote stations used for baseline distance assessment.	40
Figure 22. Example of command-line prompt used for TEQC decimation.....	42
Figure 23. Screen capture of the REDtoolbox interface after importing all required files.	43
Figure 24. Screen capture of raw GNSS import wizard in Inertial Explorer.....	45
Figure 25. Inertial Explorer interface with uncorrected (left) and PPP corrected (right) points, using imagery from the WingtraOne UAS at 120m AGL.	46
Figure 26. “blast2dem” command to generate DSMs in LAStools.	47
Figure 27. Path of height transects measured using RTK GNSS overlayed on top of WingtraOne UAS orthomosaic (75m AGL).	48
Figure 28. Workflow used for the SfM software experiment.....	49
Figure 29. Screen capture of the Interface of ODM.	53
Figure 30. Example of ODM screen showing some of the processing parameters.	54
Figure 31. Example of ODM interface during processing.	54
Figure 32. Example of <i>LAStools</i> prompt to calculate vertical RMSEs from the point cloud. ..	56
Figure 33. Vertical RMSEs for base stations located at different distances (WingtraOne UAS, 120m AGL, PPK only solutions, at 1s sampling rate. This chart is not scaled to account for the spatial distance between the stations). RMSEs from Pix4D processing report, accuracies relative to total station checkpoints.....	57
Figure 34. Trendlines for RMSE vs Distance (WingtraOne UAS, 120m AGL, PPK only solutions, 30s sampling rate). RMSEs from Pix4D processing report, accuracies relative to total station checkpoints.	58

Figure 35. Linear and exponential fits for RMSE vs Distance with the local base excluded (WingtraOne UAS, 120m AGL, PPK only solutions, 30s sampling rate). RMSEs from Pix4D processing report, accuracies relative to total station checkpoints.	59
Figure 36. RMSEs results for different base stations and sampling rates (WingtraOne UAS, 120m AGL, PPK only solutions). RMSEs from Pix4D processing report, accuracies relative to total station checkpoints.....	60
Figure 37. Influence of PPK fix percentage on vertical RMSEs (WingtraOne UAS, 120m AGL, PPK only solutions). RMSEs from Pix4D processing report, accuracies relative to total station checkpoints.	61
Figure 38. RMSEs for total station vs RTK surveyed control (WingtraOne UAS, 120m AGL, PPK only at 1s and 30s). Results from Pix4D processing report.....	62
Figure 39. PPP results for WingtraOne UAS flights at altitudes 75m and 120m AGL. RMSEs from Pix4D processing report, accuracies relative to total station checkpoints.....	64
Figure 40. Number of satellites available during flight time (generated in Inertial Explorer).....	64
Figure 41. PDOP measure throughout flight time. Graph generated in Inertial Explorer.	65
Figure 42. Height profile throughout flight time. Graph generated in Inertial Explorer.	66
Figure 43. WingtraOne UAS DSM (75 m AGL) vs TLS DSM. DSMs of 5 cm resolution.	67
Figure 44. DSM of Differences (5 cm resolution).	67
Figure 45. Height difference among four RTK GNSS transects compared to the WingtraOne UAS flight (75 m AGL).....	69
Figure 46. Accuracy comparison of autonomous, PPK, and PPP GNSS techniques using WingtraOne UAS imagery (75 m and 120 m AGL). RMSEs from Pix4D processing report, relative to total station checkpoints.....	71

Figure 47. Comparison of PPK vs RTK accuracies using DJI Phantom 4 RTK imagery (59 m AGL). RMSEs obtained from Pix4D processing report, relative to total station checkpoints.	72
Figure 48. Vertical RMSEs for different SfM software for North Packery Channel dataset (WingtraOne UAS, 100 m AGL, RMSEs relative to RTK GNSS checkpoints).	73
Figure 49. Resulting DSMs for North Packery Channel (WingtraOne UAS, 100 m AGL).	74
Figure 50. Unmasked vs masked DSMs for North Packery Channel (WingtraOne UAS, 100 m AGL, RMSEs relative to RTK GNSS checkpoints).....	75
Figure 51. Screen capture of Metashape interface showing the point cloud before masking (left) and after masking (right) of water features at North Packery Channel.....	76
Figure 52. Processing results for different SfM software using data from Mustang Island State Park (WingtraOne UAS, 75 m AGL, RMSEs relative to total station checkpoints, although there are two examples of using GCPs for ODM).....	77
Figure 53. Resulting DSMs from Mustang Island State Park (WingtraOne UAS, 75 m AGL)...	78
Figure 54. Mustang Island State Park survey field notes.....	102
Figure 55. Precise OPUS solution using the local base station at Mustang Island State Park. ..	106
Figure 56. Command-line capture of 1s data decimation for TXPO and TXCC stations.....	107
Figure 57. Command-line capture of 1s data merge for the GNSS Trimble Antenna at TAMUCC's NRC Building.....	107
Figure 58. Metashape and Pix4D geotag WingtraHub output formats.	108
Figure 59. Lat/Lon/Alt (top) vs Long/Lat/Alt vs Custom geotag WingtraHub output formats.	108
Figure 60. WingtraHub processing report using dataset from WingtraOne UAS at 120 m AGL, 1-second sampling rate, local base.....	109

Figure 61. WingtraHub processing report using dataset from WingtraOne UAS at 120 m AGL, 5-second sampling rate, local base.....	110
Figure 62. WingtraHub processing report using dataset from WingtraOne UAS at 120 m AGL, 15-second sampling rate, local base.....	111
Figure 63. WingtraHub processing report using dataset from WingtraOne UAS at 120 m AGL, 30-second sampling rate, local base.....	112
Figure 64. Map of all base stations used for PPK processing of the Mustang Island State Park dataset.....	113
Figure 65. Base stations located within 30 km of the Mustang Island State Park survey site. ..	114
Figure 66. Settings used for PPP processing (Inertial Explorer)	117
Figure 67. Interface of CSRS-PPP.....	119
Figure 68. Epochs recorded WingtraOne UAS PPK (WingtraOne UAS at Mustang Island State Park, 120 m AGL, CSRS-PPP report).....	119
Figure 69. Excerpt of Python script used to plot transect height differences.	120
Figure 70. Page 1 of the MSA report from the TLS (at Mustang Island State Park).	121
Figure 71. Page 2 of the MSA report from the TLS (at Mustang Island State Park).	122
Figure 72. Page 3 of the MSA report from the TLS (at Mustang Island State Park).	123
Figure 73. Page 4 of the MSA report from the TLS (at Mustang Island State Park).	124
Figure 74. Page 5 of the MSA report from the TLS (at Mustang Island State Park).	125
Figure 75. Page 6 of the MSA report from the TLS (at Mustang Island State Park).	126
Figure 76. North Packery Channel DTMs (WingtraOne UAS dataset at 100 m AGL).	127
Figure 77. North Packery Channel orthomosaics (WingtraOne UAS dataset at 100 m AGL). ..	128

Figure 78. North Packery Channel point clouds (WingtraOne UAS dataset at 100 m AGL, screenshot from CloudCompare).	129
Figure 79. Mustang Island State Park DTMs (WingtraOne UAS dataset at 75 m AGL).	130
Figure 80. Mustang Island State Park orthomosaics (WingtraOne UAS dataset at 75 m AGL).131	
Figure 81. Mustang Island State Park point clouds (WingtraOne UAS dataset at 75 m AGL, screenshot from CloudCompare).	132
Figure 82. Checkpoint accuracies from Drone2Map processing report (uses Mustang Island State Park local base at 1 s, WingtraOne UAS at 75 m AGL). RMSEs relative to total station checkpoints.	133
Figure 83. Checkpoint accuracies from Metashape processing report (uses Mustang Island State Park local base at 1 s, WingtraOne UAS at 75 m AGL). RMSEs relative to total station checkpoints.	134
Figure 84. Checkpoint accuracies from Pix4D processing report (uses Mustang Island State Park local base at 1 s, WingtraOne UAS at 75 m AGL). RMSEs relative to total station checkpoints.	135

LIST OF TABLES

	Page
Table 1. Vertical accuracy/quality example for digital elevation data (ASPRS, 2015).....	13
Table 2. Recommended number of checkpoints based on survey area (ASPRS, 2015).....	13
Table 3. WingtraOne UAS PPK specifications.....	15
Table 4. DJI Phantom 4 RTK specifications.	17
Table 5. Notes about Septentrio NR3 GNSS receivers.....	18
Table 6. Riegl VZ-2000i TLS specifications.....	19
Table 7. TS15 P1 specifications.	20
Table 8. Software and tools used for the GNSS evaluation test.....	21
Table 9. Software used for SfM evaluation test.....	22
Table 10. Summary of flight plan for North Packery Channel.....	23
Table 11. Summary of flight plan for Mustang Island State Park.	26
Table 12. Results from the least-squares adjustment on SurvNET.....	29
Table 13. Differences between total station and RTK ground control measurements [Total Station - RTK].....	29
Table 14. Number of satellites observed during the survey time (Trimble GNSS Planning).	32
Table 15. Overall TLS scan details MSA report.....	32
Table 16. General information for different TLS scan positions (MSA report).	32
Table 17. List of the stations used for PPK data processing and their respective sources that provided information about them.....	41
Table 18. PPP processing settings in Inertial Explorer.....	46
Table 19. Processing parameters that were changed during ODM processing.....	53

Table 20. Statistic measures for Total Station and RTK surveyed ground control using the local base station. Uses imagery of WingtraOne UAS flight at 120m AGL. Results from Pix4D processing report, accuracies relative to total station checkpoints.	62
Table 21. Statistic measures for DJI flight in PPK mode. Uses local base station, results from Pix4D processing report, accuracies relative to total station checkpoints.....	63
Table 22. Statistic measures for DJI flight in RTK mode. Uses results from Pix4D processing report, accuracies relative to total station checkpoints.	63
Table 23. Statistics of DSM of Differences.....	68
Table 24. Height differences between WingtraOne UAS DSM (75m AGL) and RTK GNSS measurements.....	68
Table 25. Mean, standard deviation, and RMSEs of height differences between WingtraOne UAS DSM (75m AGL) and RTK GNSS.....	69
Table 26. Difference in vertical RMSEs for autonomous and PPK-corrected imagery (WingtraOne UAS imagery at 120 m AGL) before and after adding GCPs for georeferencing. RMSEs from Pix4D processing report, relative to total station checkpoints.....	70
Table 27. Difference in vertical accuracies for North Packery Channel dataset (WingtraOne UAS, 100 m AGL, RMSEs relative to RTK GNSS checkpoints).	73
Table 28. Difference in vertical accuracies for Mustang Island State Park (WingtraOne UAS, 75 m AGL, RMSEs relative to total station checkpoints).	76
Table 29. Comparison between Drone2Map and Pix4D.	79
Table 30. Comparison between Metashape, ODM and Pix4D.....	80
Table 31. Strengths and weaknesses of Drone2Map, Metashape, ODM, and Pix4D.	81

Table 32. WingtraHub and Pix4D PPK processing accuracies (Mustang Island State Park, 1 s sampling rate WingtraOne UAS at 120 m AGL, RMSEs relative to total station control).	115
Table 33. WingtraHub and Pix4D PPK processing accuracies (Mustang Island State Park, 5 s sampling rate WingtraOne UAS at 120 m AGL, RMSEs relative to total station control).	115
Table 34. WingtraHub and Pix4D PPK processing accuracies (Mustang Island State Park, 15 s sampling rate WingtraOne UAS at 120 m AGL, RMSEs relative to total station control).	116
Table 35. WingtraHub and Pix4D PPK processing accuracies (Mustang Island State Park, 30 s sampling rate WingtraOne UAS at 120 m AGL, RMSEs relative to total station control).	116

CHAPTER I

INTRODUCTION

1.1. Background

In recent times, advancements in Unoccupied Aircraft Systems (UAS), broadly known as drones, and Structure-from-Motion (SfM) photogrammetry have allowed for more optimized methods to collect survey data for topographic mapping, particularly when surveying remote areas. Historically, said surveys were conducted with the aid of instruments such as total stations and level rods, which proved inefficient due to the substantial time they needed for completion.

The emergence of UAS-SfM has drastically reduced the amount of time required to acquire topographic data and generate maps with such data. As UAS-SfM continues to expand, there has been an increasing interest in evaluating the accuracy of UAS-generated products as influenced by the georeferencing technique utilized. Traditionally, the imagery used for UAS-SfM processing is georeferenced through a technique known as indirect georeferencing, in which ground control points (GCPs) are used to tie the UAS imagery to a given point on earth. Though accurate and popular, the use of GCPs for georeferencing UAS imagery can be impractical for reasons such as difficulty to implement in areas of limited physical access, additional time needed to use these points during the survey and post-processing, and potential movement of the GCPs by pedestrians, water, or even wind. The modern alternatives to these challenges have been direct georeferencing techniques, which use onboard Global Navigation Satellite Systems (GNSS) technologies to georeference the UAS imagery used for mapping.

1.2. Summary of Objectives

This study evaluates pertinent workflows associated with field data acquisition and post-processing. The two principal contributions of this study are summarized as follows:

1. Perform UAS field data collection tests to evaluate the following three different GNSS kinematic solutions as alternatives to GCPs for georeferencing UAS imagery and derived mapping projects: Real-Time Kinematic (RTK), Post-Processed Kinematic (PPK), and Precise Point Positioning (PPP). Supplementary testing is conducted to assess the influence of GNSS sampling rate, PPK fix percentage, GNSS baseline distance, and UAS flying height on vertical accuracy of SfM data products. Accuracy results are compared to ground control data acquired using RTK GNSS, a total station survey, and a terrestrial laser scanner.
2. Process data in multiple commercial and open source SfM processing software and provide a comparative assessment. The commercial software evaluated are Drone2Map (maintained by the USA's Environmental Systems Research Institute – ESRI), Agisoft Metashape (or simply Metashape, formerly PhotoScan, by Russian organization Agisoft LLC), Pix4Dmapper (or simply, Pix4D, part of the Swiss suite Pix4D). The open source software evaluated is Web OpenDroneMap (or simply ODM, a web-based SfM software engineered by geospatial developers based in the USA). The comparative assessment includes a quantitative assessment of positional accuracy of point cloud outputs from each of the software as well as a qualitative assessment on the appearance of the generated point clouds, orthomosaics, DSMs, and DTMs. Moreover, assessments are made to outline the limitations of each software as well as their advantages and disadvantages.

1.3. Motivation

This study is in alignment with a project led by the Office of Coast Survey (OCS), a branch of the National Oceanic and Atmospheric Administration (NOAA). This project is concerned with

exploring different post-processing kinematic solutions for surveying regions of limited physical access, including shoreline mapping from nautical vessels. The project relies on collaborative efforts by agencies and institutions such as Texas A&M University-Corpus Christi, Oregon State University, and NOAA.

The post-processing solutions assessed in this study would serve as alternatives to using GCPs while still maintaining survey-grade accuracy for such surveys. Additional motivations from this project include assessing take-off and landing repeatability of UAS platforms and the creation of standard operating procedures adaptable to shipboard operations.

Furthermore, the results obtained from this study could have a significant positive impact on coastal monitoring efforts, particularly in regions prone to natural disasters. The material explored in this study improves UAS survey efficiency and increases awareness about different processing and georeferencing techniques that can be employed. Ultimately, these can facilitate studies by agencies dedicated to a variety of tasks ranging from coastal mapping to temporal monitoring, thus benefiting all parties concerned with promptly acquiring and processing UAS data for their business activities.

Lastly, the author of this thesis desires a professional career as a geospatial scientist and intends to partake in projects related to coastal and offshore applications of Remote Sensing, all of which rely heavily on the methods explored herein.

CHAPTER II

REVIEW OF THE LITERATURE

Unoccupied Aircraft Systems are platforms that are “uninhabited and reusable motorized aerial vehicles which are remotely controlled, semi-autonomous, or have a combination of these capabilities” (Uysal et al., 2015). Applications of UAS include activities such as environmental monitoring (Tmušić et al., 2020), land use development, (Halls & Magolan, 2019), morphology change (Duo et al., 2021 and Hastaoğlu et al., 2019), mapping of marine litter (Gonçalves et al., 2020), disaster management (Xu et al., 2014), archeological studies (Naanouh & Stanislava, 2020), and topographic surveys (James et al., 2017 and Chuyen et al., 2019). They are also used every day for casual activities such as photography and fishing. Specific applications of UAS are determined by the type of sensors that are mounted on the platform. Two of the most used sensors in geospatial engineering are RGB cameras (Red Green Blue) and Light Detection and Ranging (LiDAR) sensors. Sometimes professionals and researchers use both sensors separately to collect data from a single location (i.e., Bandini et al., 2020), or they may even utilize a system that has both RGB and LiDAR capabilities (i.e., Kalacska et al., 2021).

Structure-from-Motion (SfM) photogrammetry is a method of remote sensing that uses overlapping images to reconstruct an area of interest (Kalacska et al., 2021). Figure 1 describes the SfM process. In short, it consists of acquiring overlapping images and using computer vision technology to detect and match unique points in various images which are ultimately used to create a point cloud and three-dimensional models of the mapped area. The accuracy of UAS-SfM is affected by factors such as the quality of the camera used, georeferencing technique (Fraser, 2013 and Sanz-Ablanedo et al., 2018), distribution of GCPs, image overlap, object motion, modeling of lens distortion (Slocum & Parish, 2017), turbulence and wind speeds (Chu et al., 2021), the UAS

used (Mugnai & Tucci, 2022), and the altitude at which the system is flown (Thomas et al., 2020). Starek et al. (2019) define the ground sample distance (GSD) as the “projected pixel width on the ground” and explain that it is a function of the focal length of the camera used, the characteristics of the sensor, and the altitude at which the photos are taken. Higher GSDs usually lead to high-quality imagery. Tmušić et al. (2020) recommend excluding low-quality images from processing.

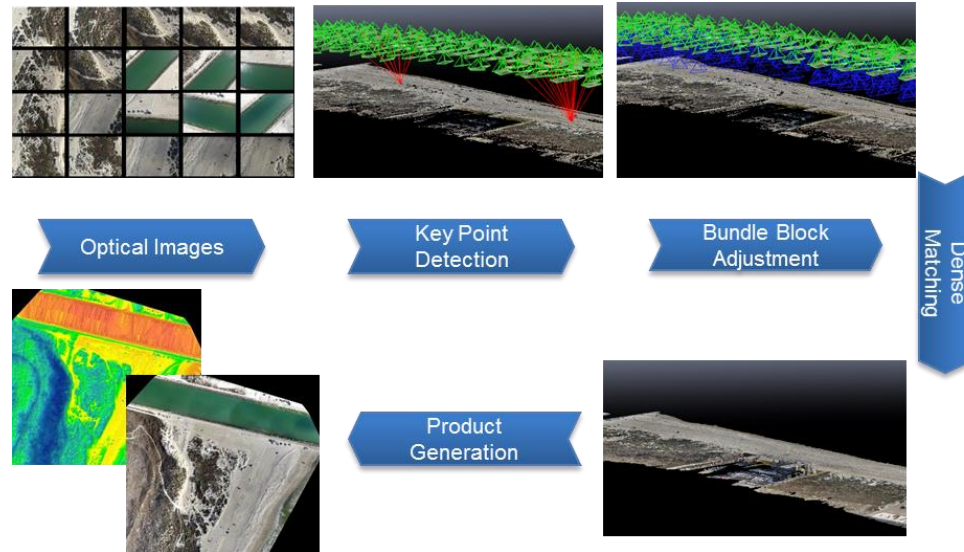


Figure 1. Summary of the SfM workflow (Starek et al., 2019).

There are various software options used for SfM processing. Some are commercial options (i.e., Metashape, Drone2Map, Pix4D) and others are open-source (i.e., COLMAP, OpenMVG, and ODM). They have varying advantages and disadvantages as well as levels of performance, depending on the environment at hand. Schwind & Starek (2017) are only one of the numerous studies that evaluate different SfM software. In their study, several land covers/uses were surveyed using a UAS and processed using PhotoScan (before it became Agisoft Metashape) and Pix4D. Results suggested better performance for Pix4D when surveying marsh and beach, and PhotoScan for oblique-oriented objects such as houses.

Digital Elevation Models (DEMs) are one of the most common products generated using SfM photogrammetry. DEMs are a pixel geometric representation of the topography in a surveyed

area. They can be categorized into Digital Surface Models (DSMs) and Digital Terrain Models (DTMs). DSMs are topographic representations of the earth that include features elevated above the earth such as buildings and trees, while DTMs include only topography void of surface features (Rogers et al., 2020).

Georeferencing techniques are the tools used to assign an x and y coordinate value to an object. In the context of UAS-SfM, to georeference an image means to assign the image a pair of coordinates such that it can be located on the Earth's surface. As Wolf et al. (2014) explain, the process of georeferencing, also known as ground registration, sees that the imagery used is aligned with a northing and easting in a given coordinate system. The georeferencing methods can be categorized into Indirect Georeferencing and Direct Georeferencing (Sanz-Ablanedo et al., 2018). Coordinate systems are extremely important for UAS-SfM surveys. In short, they are frameworks that assign a horizontal and vertical coordinate value to a feature of interest. They can be subdivided into geographic and projected coordinate systems. The former is a framework that defines features of interest on a model of the earth. The latter converts geographic units into a flat-like frame, which is commonly defined through mathematical algorithms (Smith, 2020).

Traditionally, UAS imagery used is georeferenced using GCPs (Rabah et al., 2018), a process known as Indirect Georeferencing, in which the GCPs are used to help with Aero-Triangulation (AT) and can reach accuracies of 0.02 meters (Padró et al., 2019). Although usually the most accurate of methods (Forlani et al., 2018), Indirect Georeferencing can be unfeasible at times due to reasons such as the substantial overhead needed to compensate for the manufacturing (painting and materializing) of GCPs and the difficulty of physical access to remote areas (Padró et al., 2019). In addition, this method is often time-consuming, subject to potential inconsistencies due to targets moving between the time they were placed and the time they were surveyed (Wolf

et al., 2014), inappropriate when surveying non-flat surfaces (Lillesand et al., 2015), and incurs significant labor expenses, especially when surveying larger geographic areas (Ghilani, 2017). Oniga et al. (2018) also discuss that the use of GCPs can be tedious in the field and after a survey, especially when using them excessively. These issues have coaxed organizations into seeking other ways to conduct UAS surveys without having to rely on GCPs for georeferencing.

Developments in GNSS technology now allow UAS surveys to be georeferenced using built-in geopositional capabilities, in a process that is commonly known as Direct Georeferencing. Alongside GNSS, the emergence of Inertial Navigation Systems (INS) has facilitated the determination of the external orientation parameters needed for georeferencing: coordinate values X, Y, and Z, as well as camera rotation angles Omega (ω), Phi (ϕ), and Kappa (κ). This eliminates the need for GCPs (Turner et al., 2014), which are used to determine the external orientation parameters through AT (Rabah et al., 2018). GNSS does not provide the angular orientation of the exposure of each photo (Wolf et al., 2014), hence INS is so important because it does provide that information (Lillesand et al., 2015). While there has been substantial research about the use of GNSS technology in UAS-SfM georeferencing, more assessment is needed that evaluates how different GNSS collection methods affect the accuracy of UAS-SfM-generated data.

Direct Georeferencing occurs when UAS-SfM data is georeferenced using onboard GNSS technology built within the UAS platform. It is highly dependent on the quality of the receiver and flying altitude. Turner et al. (2014) emphasize that the accuracy of Direct Georeferencing can decrease with increasing altitudes. When directly georeferencing imagery, loss of accuracy is frequent with cheap navigation-grade Global Positioning System (GPS) units, and in the presence of imprecise time synchronization between the capture of the imagery and the GNSS receiver. The effects of this delayed time synchronization have been addressed in studies such as Turner et al.

(2014) and Daakir et al. (2017). Turner et al. (2014) explain that the effects of the delayed synchronization between the camera shutter and the GNSS receiver are more noticeable as the speed of the UAS platform increases. There are tools available to improve this synchronization, even up to 1 millisecond, but minimal delays should still be expected and accounted for if the margin of error is known. In some cameras, this delay is given by the maximum shutter speed, a value usually provided in the manufacturer's specifications. Moreover, the impact of synchronization can be minimized by using a sampling GPS receiver in conjunction with plausible interpolation techniques (Daakir et al., 2017).

Available literature (Padró et al., 2019 and Turner et al., 2014) explains that the accuracy of Direct Georeferencing can be enhanced by using a dual-frequency differential receiver. Because GNSS encompasses constellations from across the world (i.e., USA's GPS, Russia's GLONASS), it helps to work with receivers that can detect signal frequencies from different constellations. Users of Direct Georeferencing workflows must account for biases such as satellite and clock errors, ionospheric and tropospheric refraction (Sickle, 2015), ephemeris, multipath, instrumental miscentering, antenna height measurements, and satellite geometry (Ghilani, 2017).

GNSS correction techniques are used to improve the solutions from GNSS measurements. In the context of UAS-SfM, these techniques are extremely important because they ensure that each image has the most accurate pair of vertical and horizontal coordinates. Three of the most common GNSS correction techniques are Real-Time Kinematic (RTK), Post-Processed Kinematic (PPK), and Precise Point Positioning (PPP).

RTK provides immediate solutions (Ghilani, 2017) by accounting for positional errors through the continuous collection of differential information about an area of interest. It uses a combination of a base station and a rover receiver (Rokaha et al., 2019) for that purpose, where

the location of the base is known, and the rover receiver is of unknown location and is constantly moving. Solution differences between the base and the rover receiver are then used to solve the unknown integer ambiguities (Wolf et al., 2014). RTK is efficient when uninterrupted synchronization between the base and the receiver occurs. Loss of signal leads to inaccurate solutions. RTK has been reported to produce errors 5-7 cm larger than GCPs (Forlani et al., 2018).

PPK is similar to RTK in the sense that a base receiver is used in coordination with a moving rover receiver. However, instead of making real-time corrections, solutions are obtained after the survey has taken place. Both RTK and PPK are often associated with Real-Time Networks (RTNs), the name given to a set of networks used for real-time differential satellite corrections (Sickle, 2015). When employing UAS surveys, the rover station is usually the aircraft being flown and the base station can be either a temporary station occupied by a GPS (i.e., static survey) or a nearby base station that logs GNSS information, such as Continuous Operating Reference Stations (CORS). CORS are perceived as a subset of RTNs. They are often used in GNSS surveys because their position is known very accurately, and they are occupied by a receiver that continuously collects satellite data about them. Thus, CORS are conceivable base stations to use when performing RTK or PPK surveys (Ghilani, 2017). Higher accuracies are possible when using base stations as close to the survey site as possible (Bisnath et al., 2004). In other words, the accuracy of solutions is inversely proportional to the distance between the base station and rover receiver.

Static surveys or observations are a common GNSS aiding technique in which a stationary GNSS receiver collects GNSS measurements for an extended period, which then serve as the foundation for subsequent GNSS corrections. Static observations are often processed using the NGS Online Positioning User Service (OPUS) tool. According to the NGS (2020), OPUS allows submissions of observations of 15 minutes minimum and 48 hours maximum. The accuracy of

results is directly proportional to the length of observations. OPUS's current structure allows only static observations recorded in intervals of 1, 2, 3, 5, 10, or 30 seconds. Regardless of the interval chosen, OPUS automatically decimates the input data to 30 seconds before processing. Results are sent to an email of the user's choice. Jamieson & Gillins (2018) and Alkan et al. (2017) list alternative services for processing static observations, including AUSPOS, GNSS Analysis and Positioning Software, and Trimble Real Time eXtended.

When utilizing PPP, GNSS solutions undergo extensive processing to solve ambiguities related to ephemeris and clock data (Sickle, 2015 and Angrisano et al., 2020). These include detailed information about satellite location, timing, and health. Some of the errors considered when using PPP are the ionospheric and tropospheric delays, relativity effect, satellite and receiver clock corrections, and the satellite antenna offset (Lu & Li, 2011). PPP has been available for several years and commonly offers broadcast, ultra-rapid, rapid, and final solutions. Though most accurate (can reach sub-centimeter accuracies), final solutions require extensive time to solve for ambiguities (12-18 days) thus making them unfeasible when working under time constraints. PPP is broadly categorized into static or kinematic. Static PPP occurs when solutions are required for a single point, and Kinematic PPP occurs when solutions are required for a moving receiver (i.e., UAS platform). PPP requires no support from base stations (Angrisano et al., 2020 and NovAtel, 2015), making it extremely convenient for surveying remote areas (Choy & Harima, 2020).

Common services available for PPP processing today include, but are not limited to, the Canadian Spatial Reference System PPP Service (CSRS-PPP), RTKLIB, GNSS Analysis and Positioning Software (GAPS), Automatic Precise Positioning Service (APPS), Real-Time Proprietary Correctors, and Applanix PP-RTX. PPP continues to gain popularity due to advantages such as ease of use and cost-effectiveness (Alkan et al., 2020), especially when using web-based

services, which are often free, require little to no GNSS knowledge, and can provide solutions very rapidly. Some of the disadvantages of using PPP include the initial convergence time, multipath (Henkel et al., 2016 and Alkan et al., 2017), the limitation in the allowable data volume that can be uploaded and processed using PPP services (Alkan et al., 2020), and the inaccessibility of services due to being out of service or schedule for maintenance (Alkan et al., 2017). Chen & Chang (2020) proposed PPPLib as a PPP processing software written in C/C++, which provides additional features such as better efficiency.

The issue of convergence time when using PPP has been discussed at length in several works such as Alkan et al. (2017), Martín et al. (2011), and Li & Zhang (2013). In simple, convergence is the period it takes for a GNSS observation to gather the right combination of parameters that affect the PPP solutions, such as satellite geometry, user environment, sampling rate, quality of observation, and most importantly, to address the corrupted initial fractional non-integer receiver- and satellite-dependent uncalibrated phase delays (Martín et al., 2011). The most accurate results are obtained during long surveys, and centimeter-level accuracies were achieved under convergence times of as little as 30 minutes (Li & Zhang, 2013) or as much as 70 minutes (Alkan et al., 2017). These studies agree that multi-frequency GNSS and less float GPS solutions contribute to a faster convergence rate. There is also evidence that Kinematic PPP is generally less accurate than Static PPP (Berber et al., 2021).

Padró et al. (2019) assess four different UAS georeferencing techniques: (i) Direct Georeferencing using on-board raw GNSS data, (ii) Direct Georeferencing using PPK single frequency carrier-phase using information from a reference station located 4 km from the survey site, (iii) Direct Georeferencing using PPK with dual-frequency carrier-phase GNSS data and differential GPS to correct for errors, and (iv) Indirect Georeferencing using GCPs. Their findings

showed that the use of GCPs yielded the best accuracies, followed by PPK using dual-frequency GNSS data. However, these two were also the most expensive surveys to conduct.

Generally, higher positional accuracies can be achieved when using GNSS to collect multiple epochs over a given point on earth. However, this is practically impossible to achieve when using Direct Georeferencing (without GCPs) to georeference UAS imagery because the platform is constantly moving (Sanz-Ablanedo et al., 2018). When using GCPs, the accuracy of the survey depends highly on the number of GCPs used. Martínez-Carricondo et al. (2018) focus on the impact of the number of GCPs on the accuracy of SfM models. Their research fulfilled expectations by concluding that the accuracy of the models increases as the number of GCPs increases, until saturation is reached, and continued increase may adversely affect the accuracy. They also discussed the importance of placing GCPs on the edge of the survey site to improve results.

GCPs can sometimes be used as checkpoints. This happens when instead of using for georeferencing purposes, they are used solely to measure the accuracy of the survey. The American Society for Photogrammetry and Remote Sensing (ASPRS) has one of the most widely followed standards for UAS surveying. In terms of vertical checkpoints, ASPRS (2015) standards require that they be surveyed on flat or uniformly sloped open terrain, with slopes of 10% or less. Table 1 outlines the vertical standards for vertical digital data and Table 2 shows the recommended number of checkpoints according to the survey area (ASPRS, 2015). Error budget considerations outlined by the Office of Coastal Survey (OCS) require horizontal positional accuracies within 5 m, and 0.5 m vertically (in depths less than 100 m or 1 m in depths greater than 100 m), at the 95% confidence level (OCS, 2022). The allowable uncertainty is dictated by the depth at which the survey is being conducted, and higher uncertainties become allowable as depth increases.

Finally, to determine whether the accuracy has been met, the product of the Root Mean Square Error (RMSE) and a factor of 1.96 need to be less than or equal to the required accuracies. For example, the product of a 20 cm RMSE with a factor of 1.96 equals 39.2 cm, which means that this accuracy would satisfy the requirements. Conversely, an RMSE of 40 cm leads to a product of 78.4 cm, which does not meet the expected accuracies. Thus, only RMSEs of 25.5 cm or less would be acceptable.

Table 1. Vertical accuracy/quality example for digital elevation data (ASPRS, 2015)

Vertical Accuracy Class	Absolute Accuracy			Relative Accuracy (where applicable)		
	RMSEz Non-Vegetated (cm)	NVA at 95% Confidence Level (cm)	VVA at 95th Percentile (cm)	Within-Swath Hard Surface Repeatability (Max Diff) (cm)	Swath-to-Swath Non-Veg Terrain (RMSDz) (cm)	Swath-to-Swath Non-Veg Terrain (Max Diff) (cm)
1-cm	1.0	2.0	3	0.6	0.8	1.6
2.5-cm	2.5	4.9	7.5	1.5	2	4
5-cm	5.0	9.8	15	3	4	8
10-cm	10.0	19.6	30	6	8	16
15-cm	15.0	29.4	45	9	12	24
20-cm	20.0	39.2	60	12	16	32
33.3-cm	33.3	65.3	100	20	26.7	53.3
66.7-cm	66.7	130.7	200	40	53.3	106.7
100-cm	100.0	196.0	300	60	80	160
333.3-cm	333.3	653.3	1000	200	266.7	533.3

Table 2. Recommended number of checkpoints based on survey area (ASPRS, 2015).

Project Area (Square Kilometers)	Horizontal Accuracy Testing of Orthoimagery and Planimetrics	Vertical and Horizontal Accuracy Testing of Elevation Data sets		
	Total Number of Static 2D/3D Checkpoints (clearly-defined points)	Number of Static 3D Checkpoints in NVA ⁹	Number of Static 3D Checkpoints in VVA	Total Number of Static 3D Checkpoints
≤500	20	20	5	25
501-750	25	20	10	30
751-1000	30	25	15	40
1001-1250	35	30	20	50
1251-1500	40	35	25	60
1501-1750	45	40	30	70
1751-2000	50	45	35	80
2001-2250	55	50	40	90
2251-2500	60	55	45	100

CHAPTER III

METHODOLOGY

3.1. Hardware

3.1.1. WingtraOne PPK UAS

The WingtraOne PPK UAS (Figure 2 and Figure 3) was the primary platform used for this study. It weighs approximately 3.7 kg and has a wingspan of 125 cm (Wingtra, n.d.). The platform can fly up to 59 minutes under favorable conditions and operates at air temperatures ranging between -10° C and 40° C. The WingtraOne is equipped with a multi-frequency PPK GNSS receiver which uses GPS and GLONASS constellations and is ready for Galileo and BeiDou. The platform sensor used for all data collection in this study is a full-frame Sony RX1 RII full-frame digital camera of 42-megapixel resolution and focal length of 35 mm. It has a global shutter that operates at a maximum shutter speed of 1/2000 seconds. Sony (n.d.) outlines some of these specifications. Flight control is performed using the WingtraPilot application, and PPK processing of the acquired imagery is done using WingtraHub. This platform is manufactured by Swiss company Wingtra, with sales offices distributed across the world. The platform is attractive to NOAA because of its flight and PPK capabilities and is not currently under any foreign restriction.

According to the published manual, the WingtraOne can reach absolute accuracies of 1 cm horizontally, and about two to three times that factor in vertical accuracy (Wingtra, n.d.). While this platform operates as a fixed-wing, it can take off and land vertically with its rotary system, an ability commonly known as Vertical Take-Off and Landing (VTOL). This VTOL ability reduces damage caused by belly landings, which are common in some fixed-wing platforms such as the eBee Plus. This enables the platform to be operated in more confined spaces (i.e., maritime vessels). The WingtraOne is powered by a pair of Li-on, UN3481 complaint, 99 Wh batteries.

The platform has an automatic landing accuracy of less than 5 m. Tipping barely occurs at wind speeds ranging from 0-5 m/s and might occur at 5-8 m/s. Flying at wind speeds over 8 m/s is strongly discouraged. Wingtra highlights three levels of speeds attainable with the WingtraOne: operational cruise speed (16 m/s), sink cruise speed (3 m/s), and sink hover speed (2.5 m/s). The current market price for this platform without advanced add-ons is estimated at \$30,000. Table 3 summarizes the WingtraOne UAS specifications as outlined in its user manual (Wingtra, n.d.).

Table 3. WingtraOne UAS PPK specifications.

Classification	VTOL (Vertical Take-Off and Landing)
Battery	Li-on, UN3481 complaint, 99 Wh
Weight	3.7 kg
Approximate flight time	59 minutes
Maximum speed	58 km/hr
Maximum winds sustained	30 km/hr
Temperatures	-10° C to 40° C
Receiver	Multi-frequency PPK GNSS receiver
Camera/Sensor	Sony RXI RII, 42-megapixel, 35 mm focal length
Estimated price	\$30,000 without advanced add-ons



Figure 2. WingtraOne UAS PPK platform (left) and as captured during the field survey (right).



Figure 3. Action captures from operating the WingtraHub in a coastal environment.

3.1.2. DJI Phantom 4 RTK

The DJI Phantom 4 RTK (Figure 4) is a quadcopter platform measuring 35 cm diagonally, can fly up to 58 km/h and up to 6,000 meters above sea level. It can operate at temperatures ranging from 0° C to 40° C. The platform has an approximate flight time of 30 minutes and is equipped with an RTK/PPK GNSS receiver. According to DJI (2021), the onboard RTK capability can reach positional accuracies at the centimeter level and yields higher accuracies than standard compass sensors even with magnetic interference of metal structures that might exist nearby.

The Phantom 4 RTK weighs approximately 1.4 kg with the battery and propellers included. It has a sensor composed of a built-in FC6310R 20-megapixel digital camera (1-inch, CMOS sensor type), with a focal length of precisely 8.8 mm (commonly rounded up to 9 mm in user manuals and other sources). The sensor has both a mechanical and an electronic shutter. The mechanical shutter has a minimum speed of 8 seconds and a maximum speed of 1/2000 seconds (equivalent to 0.5 milliseconds). The electronic shutter also has a minimum speed of 8 seconds, but a much faster maximum speed, sitting at 1/8000 seconds (equivalent to 0.125 milliseconds).

Flight control is performed using the GS RTK application with aid of a flight controller that has a transmission range of 7 km. DJI (2021) discourages flying in severe weather conditions (snow, rain, fog, and wind speeds exceeding 10 m/s). The Phantom 4 RTK is powered by a DJI Intelligent Flight Battery of LiPo 4S type with a capacity of 5870 mAh and a voltage of 15.2 V.

PPK processing for this study was done using REDtoolbox, an external non-DJI commercial software. RTK processing requires no additional software given that the imagery is corrected during flight. Therefore, its imagery is readily available for processing when RTK is desired. The current price for the standard build of this platform could reach up to \$10,000. Refer to Table 4 for a summary of the Phantom 4 RTK specifications provided within its user manual.

Table 4. DJI Phantom 4 RTK specifications.

Classification	Quadcopter
Battery	LiPo 4S, 5870 mAh, 15.2V
Weight	1.4 kg
Approximate flight time	30 mins
Maximum winds sustained	36 km/hr
Temperatures	0° C to 40 ° C
Receiver	RTK/PPK GNSS receiver
Camera/Sensor	FC6310R, 20-megapixel, 8.8 mm focal length
Estimated price	At least \$10,000 for the standard build



Figure 4. DJI Phantom 4 RTK platform.

3.1.3. Ground Control Targets

This study used a series of ground control targets as checkpoints (see example in Figure 5). The targets used have a dimension of 0.6 m x 0.6 m (2 ft x 2 ft) and are made of wood material with a white painted cross and marked by dark circle in the middle of the target center. For more precise target measurements, white stickers were placed at the center of each target, and target numbers were painted on the targets used. Not only would this allow a more central placement of the RTK GNSS and total station reflector during measurements, but also made it easier to identify each of the targets when processing in the SfM software. Furthermore, survey stakes were used in each of the targets when processing in the SfM software. Furthermore, survey stakes were used in a handle-like hole purposely carved on each of the targets to minimize potential movement by water, wind, or even pedestrians. The stakes make it easier to spot the targets from a distance, and the hole was made to facilitate the carrying of the targets.



Figure 5. Example of a ground control target used during the survey.

3.1.4. GNSS Receiver

Ground truth GNSS data was collected using a pair of survey-grade Septentrio NR3 GNSS receivers. These were run on-site by an Allegro 2 data collector running Carlson SurvCE. One receiver was used to record static observations while the other was tied to the Texas Department of Transportation (TxDOT) RTN and used as a rover to collect ground control data. The static observations were of a 1-second sampling rate. Generally, the TxDOT RTN network can achieve horizontal accuracies within 2 cm, and vertical within 4 cm. However, studies such as Smith et al. (2014) have shown results having longitudinal accuracies at the sub-centimeter level, 2 cm in latitude, and 3 cm in vertical (see summary in Table 5). All ground control was collected using the North American Datum 1983 (NAD83), epoch of 2011, Texas South, in ellipsoid heights. Figure 6 shows the setup of the base station receiver as well as the Allegro data collector.

Table 5. Notes about Septentrio NR3 GNSS receivers

Connectivity	TxDOT RTN
Estimated accuracies	2 cm horizontal, 4 cm vertical (dependent on factors such as network coverage, satellites, and equipment calibration)
Reference	NAD83 (2011), ellipsoid heights

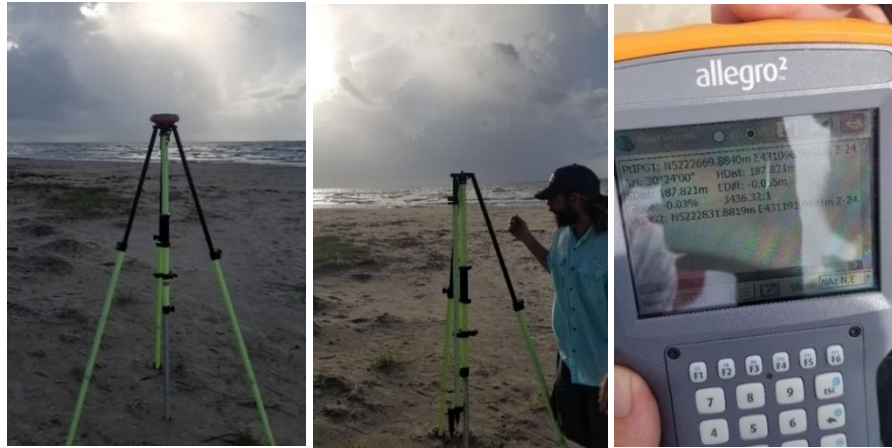


Figure 6. Septentrio NR3 receiver static setup (left-most and middle) and Allegro data collector (right-most).

3.1.5. Terrestrial Laser Scanner

A Riegl VZ-2000i geodetic-grade terrestrial laser scanner (TLS) was used for additional ground measurements. See instrument in Figure 7. The TLS has an effective range of 2 km, a laser pulse repetition rate of up to 1200 kHz and operates in the near-infrared range with a 1500 nm wavelength. The scanner is integrated with a Nikon D810 36-megapixel camera and 20 mm focal length for point cloud colorization. It has an RTK-enabled receiver, microelectromechanical systems IMU, and a compass for obtaining accurate position and orientation estimates. This includes the ability to connect to the TxDOT RTN to receive a fixed solution correction and perform automatic scan-to-scan registration and georeferencing. The scanner can be operated using the onboard screen module or through a laptop connected via Wi-Fi. Table 6 summarizes the specifications of the laser scanner.

Table 6. Riegl VZ-2000i TLS specifications.

Maximum range	2 km
Maximum laser pulse	1200 kHz
Wavelength	1500 nm (near-infrared)
Camera integration	Nikon D810, 36-megapixel, 20 mm focal length
Receiver	RTK enabled receiver
Correction	Scan-to-scan registration and georeferencing or Wi-Fi



Figure 7. Riegl VZ-2000i TLS.

3.1.6. TS15 P1 Robotic Total Station

Ground control was also surveyed using a TS15 P1 robotic Leica total station. The total station was used in combination with a GPR111 Leica prism mounted on a pole and supported by a bipod. Figure 8 shows the combination of the total station and reflector. The instrument has a laser wavelength of 658 nm, pulse repetition frequency of 100 MHz, pulse duration of 800 ps, and a nominal ocular hazard distance of 44 m.

Table 7. TS15 P1 specifications.

Model	TS15 P1
Laser wavelength	658 nm
Pulse duration	800 ps
Pulse repetition frequency	100 MHz
Nominal ocular hazard distance	44 m



Figure 8. TS15 P1 total station (left three) and reflector (right-most) used to survey the targets.

3.1.7. Computational Hardware







All processing was performed on a Windows 10 desktop computer, 64-bit, Intel(R), Core i7 – 6970X CPU at 3.00 GHz, 64 GB RAM. This computer satisfied the recommended hardware requirements for large projects when using Metashape (Over et al., 2021), Drone2Map (ESRI, n.d.), ODM (Toffanin, 2020), and Pix4D (Pix4D, 2017).

3.2. Software

3.2.1. Software (GNSS Evaluation)

Different GNSS software were used to determine whether the GNSS techniques of interest can reach the vertical accuracies stipulated for this project. The main software and tools used for the GNSS evaluation are Inertial Explorer, LAStools, REDtoolbox, TEQC, and WingtraHub. Table 8 shows the list of these software and their corresponding versions.










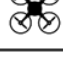
Table 8. Software and tools used for the GNSS evaluation test.

	Inertial Explorer (v8.80)
	LAStools
	Pix4Dmapper (v4.6.4)
	REDtoolbox (v2.82)
	TEQC by UNAVCO (09/25/2019 release)
	WingtraHub (v2.2.0)

3.2.2. Software (SfM Processing Evaluation)

As mentioned previously, the SfM processing software employed in this study were Drone2Map, Agisoft Metashape, ODM, and Pix4D. Supplementary software (i.e., ArcGIS Pro and CloudCompare) were used to aid in the SfM software evaluation in terms of data preparation and visualization. Table 9 shows all the software used for this evaluation.

Table 9. Software used for SfM evaluation test.

	Agisoft Metashape (v1.7.2)
	ArcGIS Pro (v2.9.0)
	Docker (v4.3.0)
	CloudCompare (v2.10.2)
	Drone2Map (v2.3.2)
	GIT Hub (v2.9.0)
	LAStools
	Pix4Dmapper (v4.6.4)
	Python (v3.8)
	WebODM (v1.9.11)

3.3. Study Sites

3.3.1. North Packery Channel (September 4, 2020)

Location

Preliminary testing was performed using UAS imagery that had been acquired by the MANTIS (Measurement and Analytics) Lab at North Packery Channel (approximate coordinates: 27.6230° N, 97.1988° W - Figure 9) on September 4, 2020. This location encompassed a stretch of beach of roughly 1 km² that is commonly known as JP Luby Beach. Although a more rigorous survey at a different location would later be conducted, this dataset proved suitable for preliminary processing and evaluative purposes. Furthermore, it eased the need to collect field data right at the beginning of the project, while allowing the researchers to formulate the most convenient flight plan for the subsequent datasets. Data from this site was used only for SfM software evaluation.

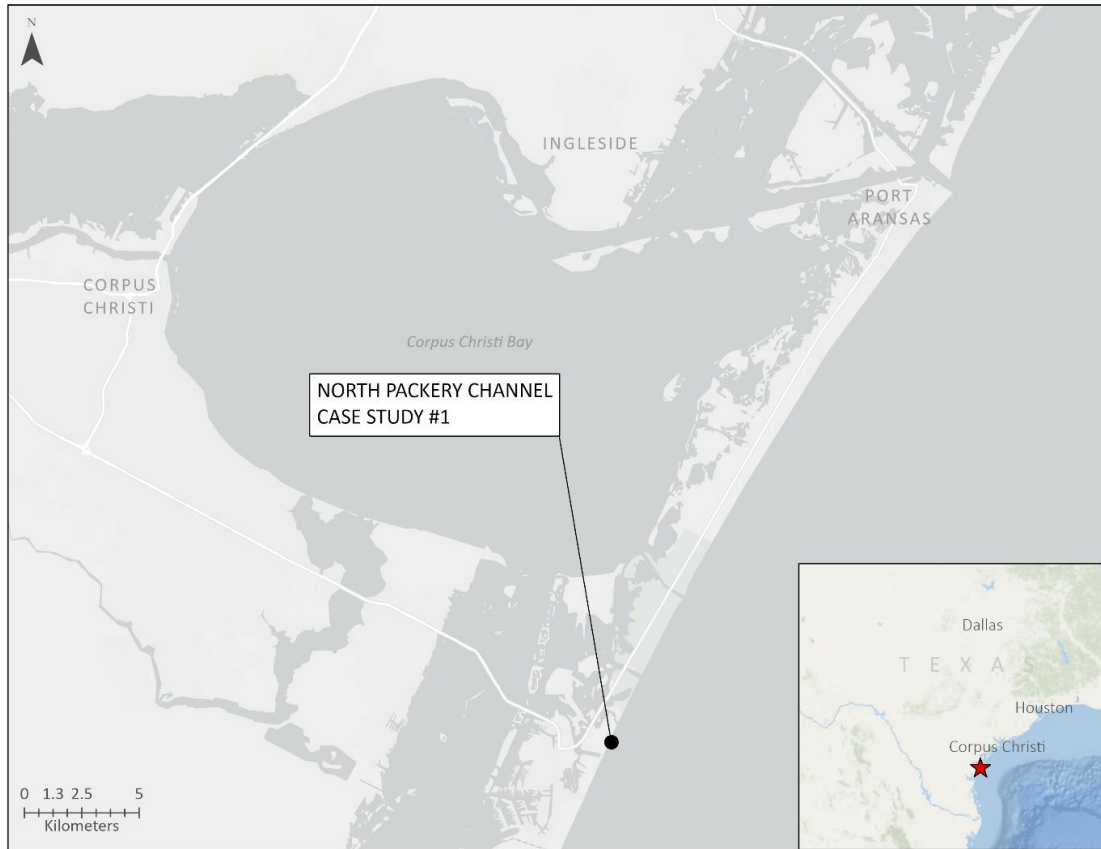


Figure 9. Location of North Packery Channel.

UAS Flight

Only the WingtraOne UAS PPK was used to acquire imagery over North Packery Channel. There were 550 photos in total, which were collected at a flying height of approximately 100 m above ground level (AGL), and a GSD of 1.30 cm/px. The flight was designed with 75% sidelap and 70% endlap. The imagery was collected in NAD83 (2011), ellipsoid heights. See Table 10 for a summary of the flight plan for this study site.

Table 10. Summary of flight plan for North Packery Channel.

Platform	WingtraOne UAS PPK
Mode	PPK
Number of photos	550
Flying height (m AGL)	100
GSD (cm/px)	1.30
Design	75% sidelap, 70% endlap
Imagery coordinate system	NAD83 (2011), ellipsoid heights

Ground Control

There were 7 aerial targets used as checkpoints within this site. They were distributed in a staggered pattern across the study area (Figure 10, point 37 in this image was not used in processing because it could only be accurately identified in one image during processing and multiple are needed for good results). These targets were surveyed using RTK GNSS differentially corrected with the TxDOT RTN, referenced to NAD83 (2011) Texas South, and using ellipsoid heights.

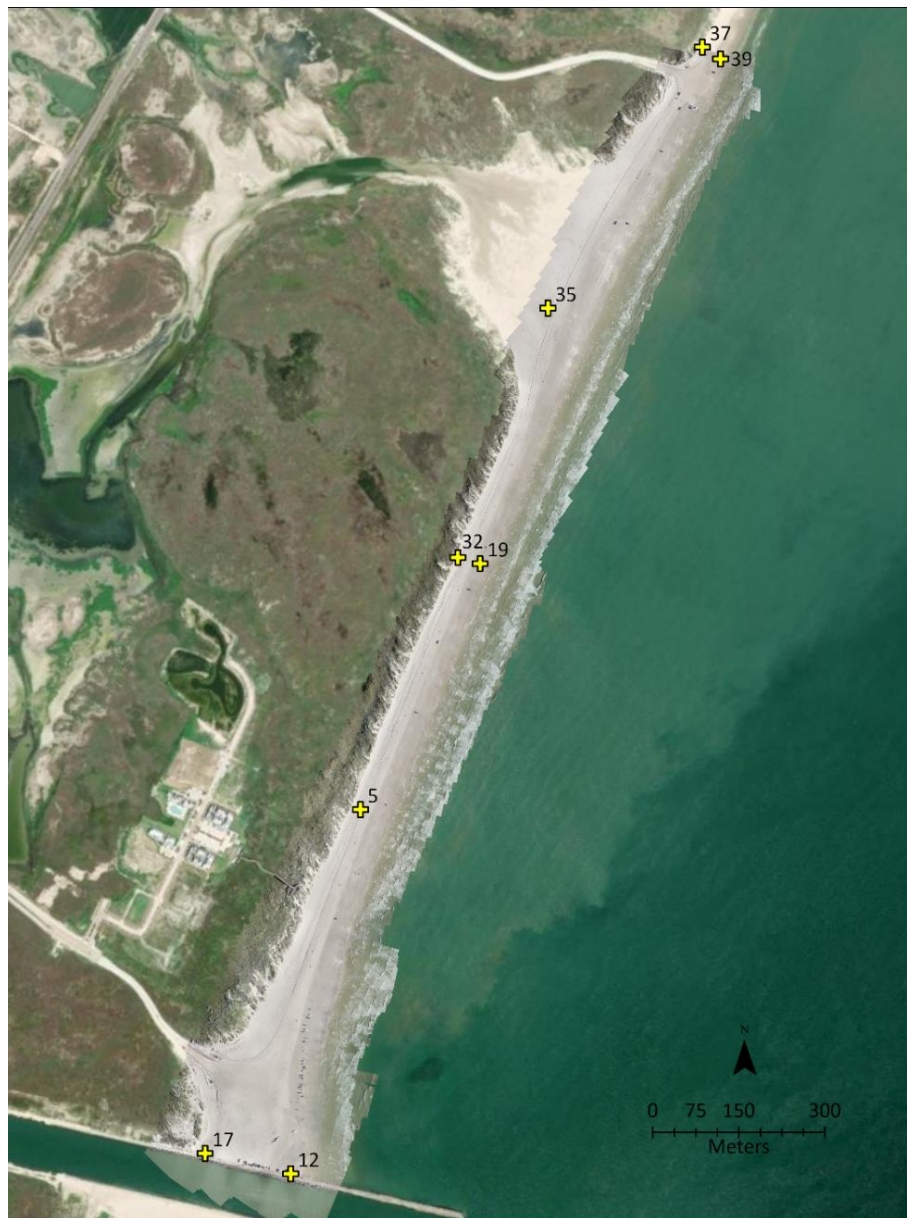


Figure 10. Ground control distribution at North Packery Channel (~ 500 m spacing).

3.3.2. Mustang Island State Park (July 13, 2021)

Location

Mustang Island State Park (Figure 11) was the principal site for this study. A rigorous survey plan was delineated and conducted on this site to ensure that a suitable workflow would be determined from processing this dataset. The data was acquired over a pedestrian stretch of beach located at the park (approximate coordinates: 27.6706° N, 97.1709° W) on July 13, 2021. The stretch of beach is approximately 0.05 km². This location was surveyed upon familiarization with the previous dataset and the SfM processing workflows that it employed. This survey was much more thorough in terms of the data collected and the redundant observations acquired. Data from this location was used both in the GNSS techniques and SfM comparison sections of this thesis.

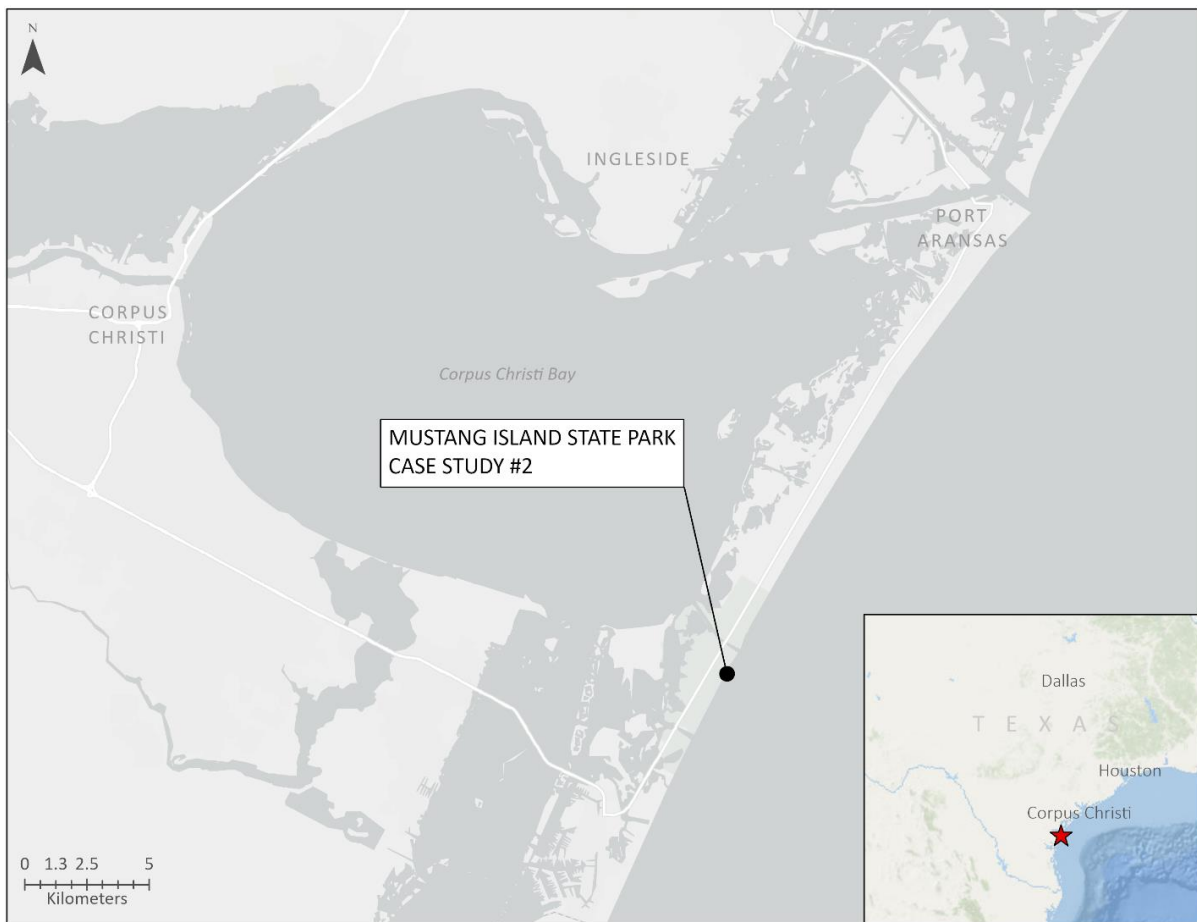


Figure 11. Location of Mustang Island State Park.

UAS Flights

Both the WingtraOne PPK UAS and the DJI Phantom 4 RTK were used to collect imagery at this location. The WingtraOne was flown twice: at 75 m AGL and 120 m AGL. The two WingtraOne flights were designed to have 80% sidelap and 70% endlap. The lower altitude flight yielded 271 photos (1 cm/px GSD) and the higher altitude yielded 120 photos (1.6 cm/px GSD).

The Phantom 4 RTK was also flown twice, first in RTK mode, and then in PPK mode. Both the RTK and the PPK modes were flown at 59 m AGL, using a double grid flight design, and yielded 610 photos (1.6 cm/px GSD) each time. The RTK flight was conducted by connecting to the TxDOT RTN, which allowed for RTK corrected imagery to be generated on-site without the need for further post-processing. The RTK mode then was disabled, and the platform was relaunched to collect imagery that would later be corrected using PPK GNSS.

There were four flights in total, conducted under favorable weather conditions with temperatures of roughly 28° C and onshore wind speeds measured at 3.35 m/s. All imagery was collected in NAD83 (2011), ellipsoid heights. See Table 11 for a summary of the flight plan for this study site. Although the Phantom 4 RTK imagery is labeled as being collected using the World Geodetic System of 1984 (WGS84), this is simply a labeling issue as that is the nature of DJI. However, because the data was collected using the TxDOT RTN, the files use the default NAD83 (2011). Tests showed that this labeling does not affect the accuracy of the resulting models.

Table 11. Summary of flight plan for Mustang Island State Park.

	WingtraOne UAS PPK		DJI Phantom 4 RTK UAS	
Mode	PPK	PPK	RTK	PPK
Number of photos	271	120	610	610
Flying height (m AGL)	75	120	59	59
GSD (cm/px)	1	1.6	1.6	1.6
Design	80% sidelap 75% endlap	80% sidelap 75% endlap	Double grid	Double grid
Imagery Coordinate System	NAD83 (2011) Ellipsoid heights	NAD83 (2011) Ellipsoid heights	NAD83 (2011) Ellipsoid heights	NAD83 (2011) Ellipsoid heights

Ground Control – RTK GNSS vs Total Station

There were 25 aerial targets (Figure 12) distributed in a staggered pattern used as checkpoints within this site. They were spaced in intervals of roughly 20 m and surveyed using both RTK GNSS and a total station. While this may seem redundant at first, this study is interested in evaluating which of these two options provided the most consistent and accurate results.

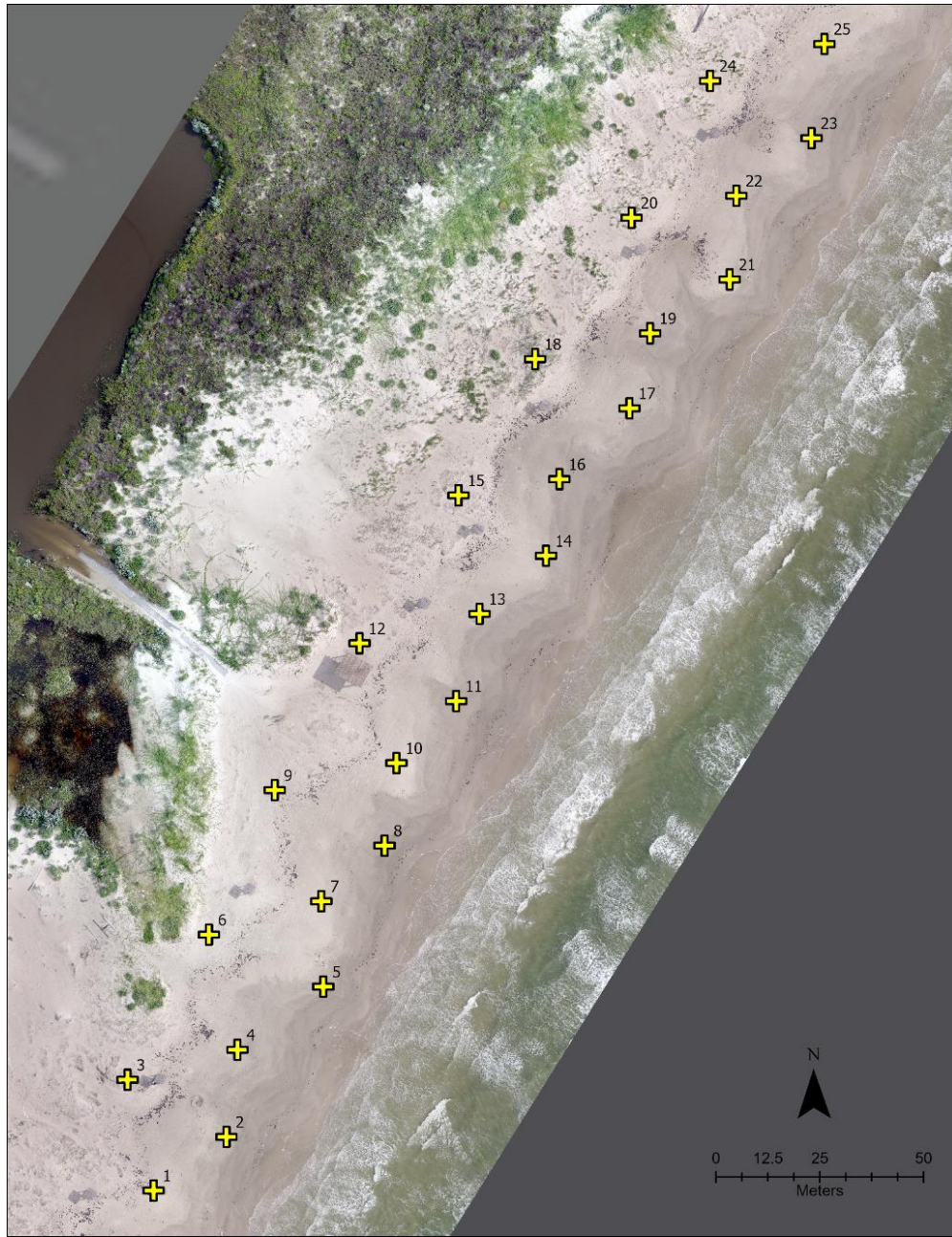


Figure 12. Ground control distribution at Mustang Island State Park (~ 20 m spacing).

Ground control measurements using RTK GNSS were conducted using TxDOT RTN, and an average of 10-second observations on each target. The total station measurements employed a resection technique in which each target was observed from two different setups and later corrected using a least-squares adjustment. Temporary survey rebars were used on the ground, which served as the base for the total station measurements. The location of these two points (IPT1 and IPT2) was determined via RTK GNSS. Here, all measurements were relative to the temporary points. All ground control was surveyed in NAD83 (2011), ellipsoid heights.

SurvNET: Total Station (Least Squares Adjustment)

The least-squares adjustment on angle and distance measurements acquired using the total station was performed using SurvNET. During the survey, observations were made with the forward and reverse face of the total station with two electronic measurements performed per face of the equipment. This addressed the systematic errors in the instrument. Next, immediately before importing the points into SurvNET, the raw data were inspected so that blunders were detected and fixed. After formatting the data as per SurvNET requirements, the remaining random errors were adjusted out of the final point coordinates to create mathematically suitable geometric conditions. The a priori standard errors provided by the instrument manufacturer were used for setting up the adjustment. A chi-squared test was performed on the adjustment to check the “goodness of fit” and failed on the low end with a value of 54.62 being less than 60.7, which meant that the data was better than expected compared to the a priori standard errors at a 95% significance level. The standard error of unit weight for the adjustment was 1.16. After differencing the adjusted total station and the RTK GNSS measurements, it was observed that the differences were very minimal. The mean height residual and the absolute maximum height residual were -0.42 cm, and 3.39 cm, respectively, with a standard deviation of 1.59 cm. Table 12 shows the results from the

least-squares adjustment as generated by SurvNET. Table 13 and Figure 13 summarize the minimal differences between the total station and the RTK GNSS measurements.

Table 12. Results from the least-squares adjustment on SurvNET.

```

Statistics
=====

Solution converged in 2 iterations

Total Observations:158
Total Unknowns:81
Degrees of Freedom:77

Observation Count      Sum Squares      Error
                        of StdRes      Factor
Coordinate              6           0.090      0.176
Angles:                 50          11.575      0.689
Distances:              51          83.733      1.835 (Mark-to-Mark)
VertAngles              51           8.211      0.575 (Mark-to-Mark)

Total:                  158          103.610      1.160

Reference Variance:1.346
Standard Error Unit Weight: (+/-)1.160
Failed the Chi-Square test at the 95.00 significance level
54.623 <= 103.610 <= 103.158

```

Table 13. Differences between total station and RTK ground control measurements [Total Station - RTK].

TOTAL STATION CONTROL				RTK CONTROL				Differences			
GCP	Northing (m)	Easting (m)	Elevation (m)	GCP	Northing (m)	Easting (m)	Elevation (m)	GCP	Northing (m)	Easting (m)	Elevation (m)
1	5222609.685	431057.277	-24.748	1	5222609.668	431057.2686	-24.7319	1	0.0170	0.0084	-0.0161
2	5222622.582	431074.831	-24.979	2	5222622.563	431074.8261	-24.9545	2	0.0190	0.0049	-0.0245
3	5222636.315	431050.998	-24.276	3	5222636.289	431051.0001	-24.2537	3	0.0260	-0.0021	-0.0223
4	5222643.528	431077.47	-24.801	4	5222643.509	431077.4672	-24.7758	4	0.0190	0.0028	-0.0252
5	5222658.719	431098.124	-25.026	5	5222658.715	431098.1107	-24.9921	5	0.0040	0.0133	-0.0339
6	5222671.235	431070.605	-24.512	6	5222671.223	431070.6155	-24.5116	6	0.0120	-0.0105	-0.0004
7	5222679.277	431097.656	-24.785	7	5222679.262	431097.674	-24.7794	7	0.0150	-0.0180	-0.0056
8	5222692.656	431112.887	-25.06	8	5222692.639	431112.8981	-25.0374	8	0.0170	-0.0111	-0.0226
9	5222705.997	431086.446	-24.557	9	5222705.984	431086.4633	-24.5318	9	0.0130	-0.0173	-0.0252
10	5222712.528	431115.76	-24.756	10	5222712.509	431115.77	-24.7463	10	0.0190	-0.0100	-0.0097
11	5222727.412	431130.136	-24.987	11	5222727.389	431130.1475	-24.9798	11	0.0230	-0.0115	-0.0072
12	5222741.344	431106.867	-24.423	12	5222741.314	431106.8765	-24.4335	12	0.0300	-0.0095	0.0105
13	5222748.393	431135.781	-24.827	13	5222748.367	431135.7791	-24.8369	13	0.0260	0.0019	0.0099
14	5222762.378	431151.769	-24.893	14	5222762.351	431151.7579	-24.9036	14	0.0270	0.0111	0.0106
15	5222776.925	431130.707	-24.473	15	5222776.889	431130.7096	-24.4793	15	0.0360	-0.0026	0.0063
16	5222780.832	431155.002	-24.863	16	5222780.797	431154.9975	-24.873	16	0.0350	0.0045	0.0100
17	5222797.851	431171.862	-24.805	17	5222797.818	431171.8526	-24.8173	17	0.0330	0.0094	0.0123
18	5222809.704	431149.167	-24.359	18	5222809.682	431149.1705	-24.3743	18	0.0220	-0.0035	0.0153
19	5222815.915	431176.852	-24.79	19	5222815.886	431176.8366	-24.8138	19	0.0290	0.0154	0.0238
20	5222843.71	431172.383	-24.403	20	5222843.658	431172.3775	-24.4118	20	0.0520	0.0055	0.0088
21	5222828.863	431195.985	-24.81	21	5222828.821	431195.9544	-24.8303	21	0.0420	0.0306	0.0203
22	5222849.003	431197.622	-24.754	22	5222848.939	431197.6031	-24.7466	22	0.0640	0.0189	-0.0074
23	5222862.876	431215.723	-24.973	23	5222862.805	431215.7031	-24.9635	23	0.0710	0.0199	-0.0095
24	5222876.63	431191.29	-24.21	24	5222876.556	431191.2815	-24.1965	24	0.0740	0.0085	-0.0135
25	5222885.51	431218.826	-24.733	25	5222885.435	431218.8131	-24.7229	25	0.0750	0.0129	-0.0101
Mean			-24.71212	Mean			-24.707904	Mean	0.0320	0.0029	-0.0042
Max			-24.21	Max			-24.1965	Max (abs)	0.0750	0.0306	0.0339
								Std dev	0.0198	0.0122	0.0159

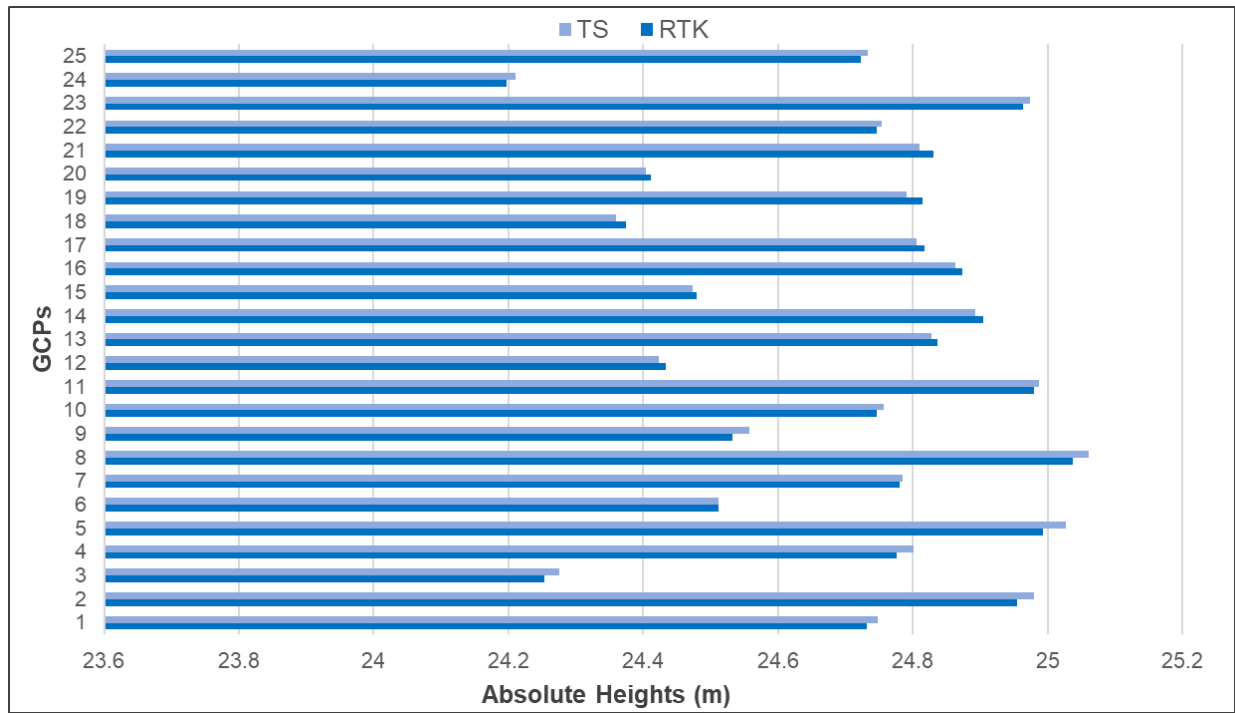


Figure 13. Differences between total station and RTK measured heights (absolute values).

GNSS Planning

An important aspect of this research was surveying the study area on a day with favorable GNSS signal reception. Because this study is heavily reliant on GNSS accuracy, Trimble GNSS Planning online tool (Trimble, 2018) was used to ensure that the survey was scheduled for a day that provided suitable conditions for surveying, particularly in terms of satellite geometry and observability. The data collection phase took place between 07:30 and 19:00 CST. Figure 14 shows a fitting dilution of precision (DOP) during the survey period, particularly with a position dilution of precision (PDOP) that was at 1.1 or less during the fieldwork. The PDOP is indicated by the green line in the middle, and PDOPs lower than 2 generally indicate good satellite geometry. The suitability of these low DOP values is further supported by Sickles (2015), who also discusses the relationship between DOP values and the distribution of satellites.

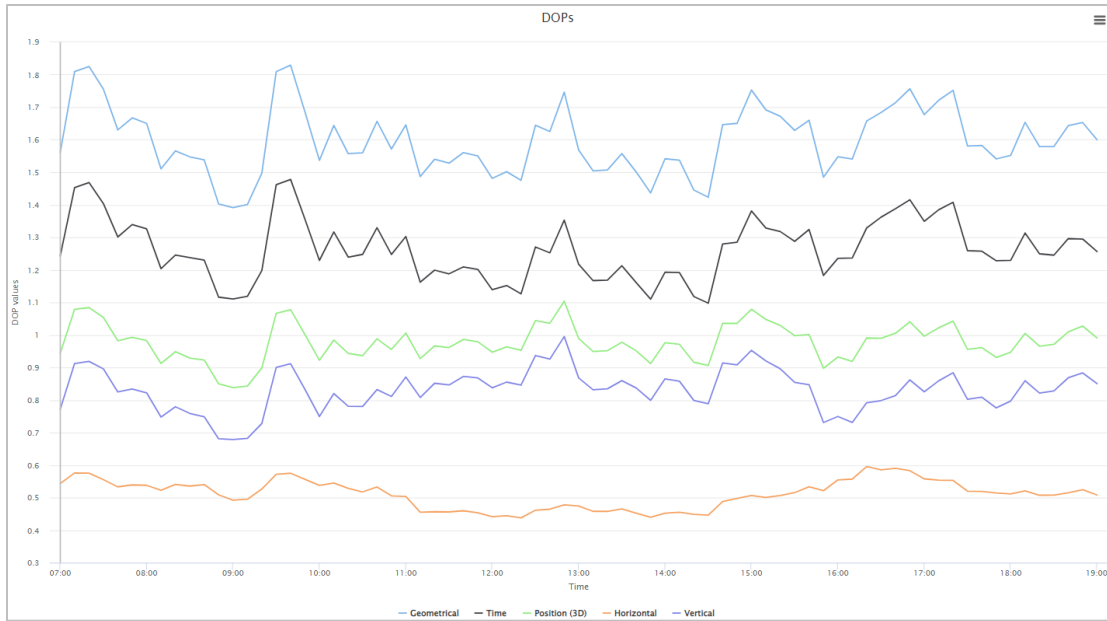


Figure 14. DOP values during the survey period (source: Trimble GNSS Planning).

Good observability of satellites was also important as the lack thereof can have a negative impact on results. Figure 15 shows the availability of GPS, GLONASS, Galileo, BeiDou, and QZSS satellites, and Table 14 shows the number of satellites observed during the survey time. Observe that the total number of satellites was no less than 26 at all times.

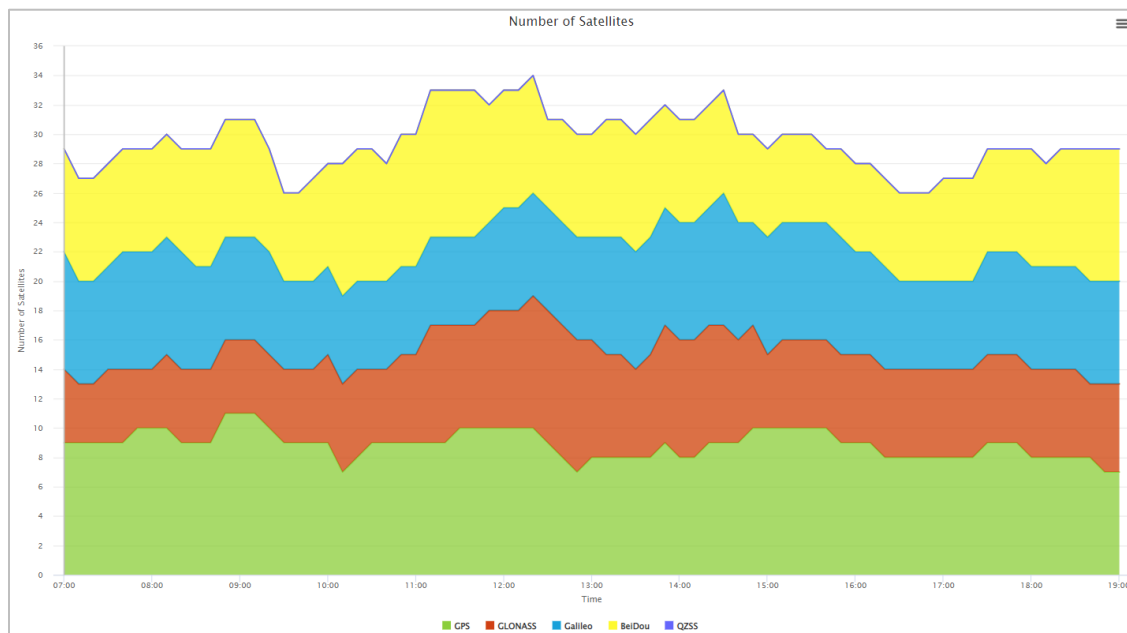


Figure 15. Satellite availability during the survey period (source: Trimble GNSS Planning).

Table 14. Number of satellites observed during the survey time (Trimble GNSS Planning).

System	Number of satellites
GPS	31
GLONASS	23
Galileo	24
BeiDou	49
QZSS	4

Ground Control – Terrestrial Laser Scanner

Lastly, a TLS survey was performed to allow for a comparison between DSMs generated with the WingtraOne UAS and that generated using the TLS. The scanner was operated using the onboard screen module and employed three setup positions at a stepping angle of 20 millidegrees, a horizontal field of view of 360°, and a vertical field of view of 70° (+30°, -40°). The scans had a total point cloud of 108,385,456. The horizontal and vertical accuracies for GNSS measurements were within 0.015 m. Table 15 and Table 16 summarize the details obtained from the scanner multi-station adjustment (MSA) report.

Table 15. Overall TLS scan details MSA report.

Coordinate system	NAD83 (2011) Texas South, ellipsoid heights
Laser pulse rate	1,200 kHz
Field of view	Horizontal (360°), vertical 70° (+30°, -40°)
Stepping angle	20 millidegrees
Gap closure distance	0.250 m
Adjustment effort	Standard
Adjustment matches	Planes to planes
Project plane patches	879
Scan position plane patches	3,449

Table 16. General information for different TLS scan positions (MSA report).

Scan	Point Count	Latitude	Longitude	GNSS acc. (horizontal)	GNSS acc. (vertical)
#1	35,707,924	N27° 40' 10.7451"	W97° 10' 16.8361"	0.014 m	0.015 m
#2	37,027,225	N27°40' 14.0043"	W97° 10' 14.1445"	0.014 m	0.014 m
#3	35,650,307	N27° 40' 16.6647"	W97° 10' 12.8554"	0.014 m	0.014 m
Total	108,385,456				

3.3.3. UAS Access Permission and Adherence to Laws

All use of UAS requires conducting surveys either in non-restricted areas or in restricted areas for which the necessary waivers and approvals have been submitted and granted. Also, UAS operators must be able to maintain visual sight of the aircraft throughout the survey. In addition, the use of UAS for non-recreational use, as was the case in this study, requires that the aircraft be registered with the Federal Aviation Administration (FAA) and operated by, or under the supervision, of a Certified Small UAS (sUAS) pilot. This study adhered to these by conducting flight missions in a non-restricted site (North Packery Channel) and acquiring the necessary permission to fly at Mustang Island State Park. The permit to fly at the park was granted by the Texas Park and Wildlife Department on November 11, 2020, and the UAS platforms utilized were registered with the FAA. All flights were conducted by registered and experienced sUAS pilots, who were able to maintain visual sight of the platforms at all times, as required by the FAA.

3.4. Study Limitations and Assumptions

This study is limited by the accuracy and efficiency of the hardware and software used, and the conditions found in the surveyed sites (i.e., weather, land cover). Also, as mentioned earlier, the study focuses on optimized UAS-SfM workflows and explores various combinations of existing techniques to examine the combination that yields the most accurate results. Although the results obtained herein can be replicated in different locations, small discrepancies should be expected when certain factors differ (i.e., weather, equipment accuracy, base stations).

The workflows employed herein assume that (i) all hardware and software are well-calibrated and performing to the best of their ability, including local and remote base station receivers, (ii) all stations are free of any bodies that may prompt signal obstruction such as buildings, and that (iii) the weather conditions were the same in all pertinent locations.

3.5. Safety and Risk

Safety and risk management are important considerations for all types of work, particularly when it involves fieldwork. Complications with such work might pose a threat to the well-being of those involved and potentially lead to unbudgeted expenses. This study addressed safety concerns by following adequate measures while on the field such as scheduling the survey for an early weekday to avoid heavy traffic (vehicular and human), maintaining continuous visual sight of the UAS platforms, ensuring that parties involved were well hydrated throughout the day, and use of proper attire for the survey day.

3.6. Datasets

The raw datasets used in this study are the imagery collected using the pair of UAS, the GNSS measurements obtained through the base and rover stations, and the point cloud acquired using the TLS. The list of processed datasets includes the Receiver Independent Exchange Format (RINEX – both observation and navigation) files created from the raw GNSS measurements, the DSMs, DTMs, orthomosaics, and the point clouds created using the various SfM software. Ancillary data includes text files, reports, tables, and graphs generated after processing the data such as flight path plots, processing reports, and height profile differences.

3.7. Methodology for GNSS Evaluation

3.7.1. Overview

This section explains the GNSS techniques and workflows used for georeferencing UAS imagery used in this study, precisely RTK, PPK, PPP, and the accuracies that these techniques can provide in comparison to autonomous or uncorrected imagery. These methods were implemented to determine whether they can reach the vertical accuracies stipulated by the OCS (2018). RTK evaluations used only imagery from the Phantom 4 RTK because the WingtraOne UAS does not

currently offer RTK capabilities. PPK evaluations used imagery from both the WingtraOne UAS and the Phantom 4 RTK. All PPP processing relied only on WingtraOne UAS imagery. Figure 16 shows the general workflow utilized for the GNSS experiment.

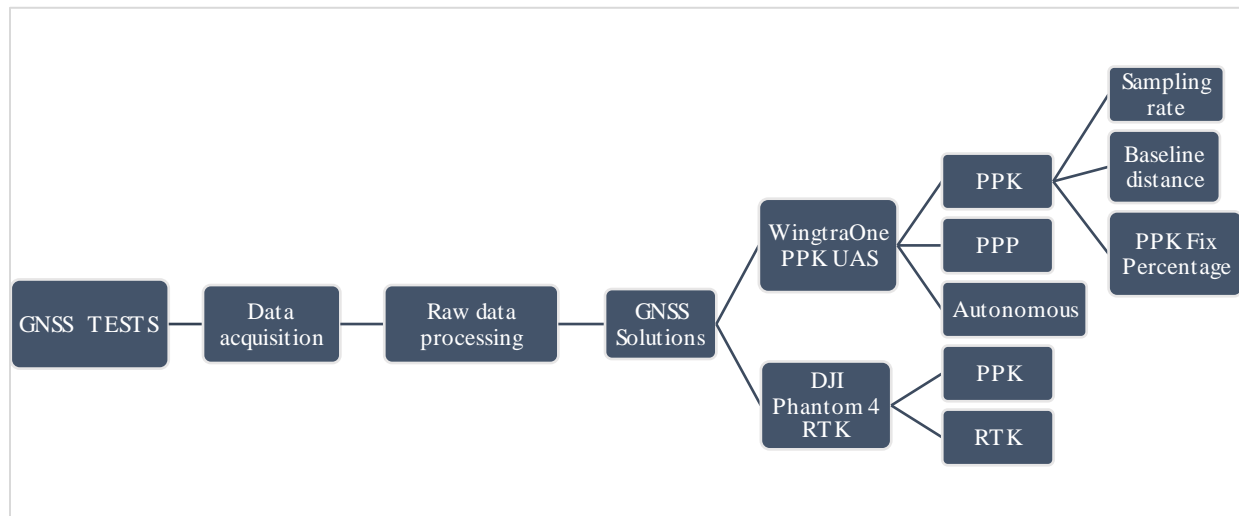


Figure 16. Workflow used for GNSS solutions experiments.

3.7.2. Performance of the PPK Georeferencing Technique

The PPK evaluation portion of this study was subdivided into the standard PPK workflow with Wingtra and the effects of different baseline distances, sampling rates, and PPK fix percentage of vertical accuracies.

PPK Workflow with Wingtra

WingtraHub was used for all WingtraOne UAS PPK processing. The software requires an observation file and at least GLONASS and GPS navigation files for accurate correction. The first step for PPK processing using the WingtraOne is to copy the binary raw GNSS file from the static receiver into a computer and use software that convert binary data into RINEX format. This study used SBF Converter to generate three RINEX files: an observation file, a GPS navigation file, and a GLONASS navigation file. The observation file was used as input on the NGS Online Positioning User Service (OPUS), to obtain precise coordinates for the base station. Although

OPUS can take observation files at several rates (1s, 2s, 3s, 5s, 10s, 15s, 30s), it automatically decimates the observation file to 30s. Also, the service is only able to process files up to 60-65 megabytes in size. If exceeded, supplementary tools are needed to decimate the observation rates. This becomes important when using observation files that cover longer periods, as they are more likely to exceed 60-65 megabytes

The next step is to work with WingtraHub. One must ensure that the computer is connected to the internet and that the WingtraOne dongle is plugged into the computer. Within WingtraHub, the user needs to navigate to the directory that contains the folder with the imagery (the directory selected is not the one containing the imagery, but rather the one that immediately precedes it). After confirming the selection, an interface opens that prompts the user to enter base files, select the type of processing, and select the base location. See Figure 17 for an example of the interface.



The screenshot shows a web interface for WingtraHub. At the top, it says "You have chosen to geotag the following project:". Below this, there is a dropdown menu showing "21_06_15_Wingtra_Low_2 Flight 01". To the right of the dropdown, there are two checkboxes: "Output geotagged images" (unchecked) and "PPK processing" (checked). Below the dropdown, there are two buttons: "Base file(s)" and "Base location". The "Base file(s)" button has a folder icon and the text "3 files selected" next to it. The "Base location" button has a location pin icon.

Figure 17. Screen capture of the WingtraHub interface.

Once the base files have been added, select the “PPK processing” option and click the base location button. It is imperative to select the PPK processing because otherwise the option to add base files will disappear and the generated products will be autonomous and referenced to WGS84 and EGM96. WingtraHub automatically creates copies of the RINEX files used for processing into the respective image folders and inevitably adds them as base files input to subsequent processing runs, even if the software is restarted. Therefore, to avoid mistakes, it is highly recommended to remove all base files before each processing run, adding only the ones that are needed, and always ensuring that there are no more than only the intended observation and navigation files at each

processing run. This means that if using the standard processing workflow, there should be no more than three base files in total, corresponding to the observation file for the base station in use, its GPS navigation file, and its GLONASS navigation file. WingtraHub does allow for other types of navigation files (i.e., BeiDou) to be added. However, GLONASS and GPS are the most widely used, and the two alone are sufficient for obtaining accurate solutions. Figure 18 shows an example of the WingtraHub interface after loading the observation and navigation files.

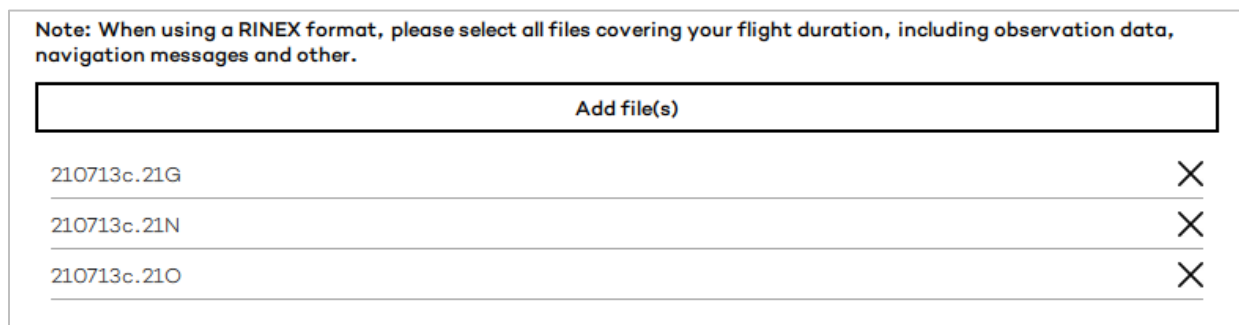


Figure 18. Example of base file import in WingtraHub.

The following step consists of creating a base location using the precise coordinates retrieved from OPUS. Figure 19 shows a completed base location in WingtraHub. The software saves every entry of a base location for future use, which is advantageous for projects that require different PPK runs for imagery collected under the same base station. WingtraHub recommends that the base station be referenced to WGS84 coordinates with ellipsoid heights. However, due to the nature of this study, NAD83 was chosen instead. The version of WingtraHub used for this project does not discern between different realizations of NAD83 (i.e., NAD83 2011), hence the use of NAD83, without specifying the 2011 epoch. Because different coordinate systems are available, it is equally important to certify that the desired system is being used and avoid undesired and potentially poor results caused by the use of the wrong coordinate systems.

Geodetic

Cartesian ECEF

21_07_13_Mustang_NOAA

Geodetic ellipsoidal height (NAD83 (EPSG:6318))

?

Location

27° 40' 10.2199100" N, 97° 10' 19.0929400" W, -22.46900 m

(27.6695055306°, -97.1719702611°, -22.46900 m)

☐ Specify base station antenna offset

Name

1_07_13_Mustang_NOAA

Latitude

27.669505530555558

Longitude

-97.17197026111111

Altitude

-22.469

m

Coordinate system

NAD83 (EPSG:6318) ▼

Figure 19. Coordinate information used in WingtraHub for the local base in this project.

Lastly, select the desired output format for the PPK corrected geotags. WingtraHub allows the user to export geotags in five different formats: Pix4D, Agisoft Metashape, Lat/Lon/Alt, Lon/Lat/Alt, and custom. The user must ensure the selection of the correct format as it will affect processing in the SfM software. This project used the Agisoft Metashape and Pix4D formats. WingtraHub runs took approximately 30 seconds. Geotags are generated as a Comma-Separated Value (CSV) file added to their respective imagery folder. A WingtraHub processing report is also added to the same folder. The report contains information such as the base files and location used, flight and processing information, and the PPK fix percentage and accuracies. See the example in Figure 20 (pertaining to the WingtraOne at 120m AGL processed using the local base at a sampling rate of 30s). It is recommended to inspect this report, as it can help to identify mistakes that may have taken place during PPK processing in WingtraHub, such as the selection of the wrong base files. Moreover, the report also alerts the user of potential errors that may lead to bad results. One of the common warnings observed during processing in WingtraHub, and also shown in Figure 20, occurs when using base files with sampling rates larger than 25 seconds.

Processing Report



Generated by WingtraHub v2.2.0

Project summary

Project	21_06_15_Wingtra_High Flight 01
Flown	2021/07/13 14:03 UTC
Processed	2021/10/12 03:46 UTC
Camera	RX1RII
Images	120

Geotagging summary

Output coordinate system	Geodetic ellipsoidal height (NAD83 (EPSG:6318))
PPK processed	Yes
Base file(s)	210713c.21G 210713c.21N localbase_30sec.21o
Base	21_07_13_Mustang_NOAA
Base location	Geodetic ellipsoidal height (NAD83 (EPSG:6318)) 27° 40' 10.2199100" N, 97° 10' 19.0929400" W, -22.46900 m 27.6695055306°, -97.1719702611°, -22.46900 m
Base antenna offset	Not specified.
Detected base antenna type	SEPALTUS_NR3 NONE

Quality Summary

Matching	120 images tagged.
PPK fix	100.00%
Mean accuracy	0.03 m horizontal, 0.04 m vertical
Warnings	- The base file update interval is larger than 25s.
Infos	None

Figure 20. Example of a WingtraHub processing report (using the local base, 30s sampling rate, GLONASS, and GPS navigation files, with the WingtraOne UAS flight at 120 m AGL).

Distance of Base Station

The first PPK assessment of interest to this research evaluated the impact of increasing baseline distances on UAS survey accuracies. This phase followed the same workflow as the preceding subsection, with the only difference being that it also used remote stations as opposed to only the static base station. A total of 22 stations were used (one local base and 21 remote base

stations). Figure 21 shows the location of the different base stations used. This includes all 1-second CORS located within an approximate radius of 200 km from the study site.

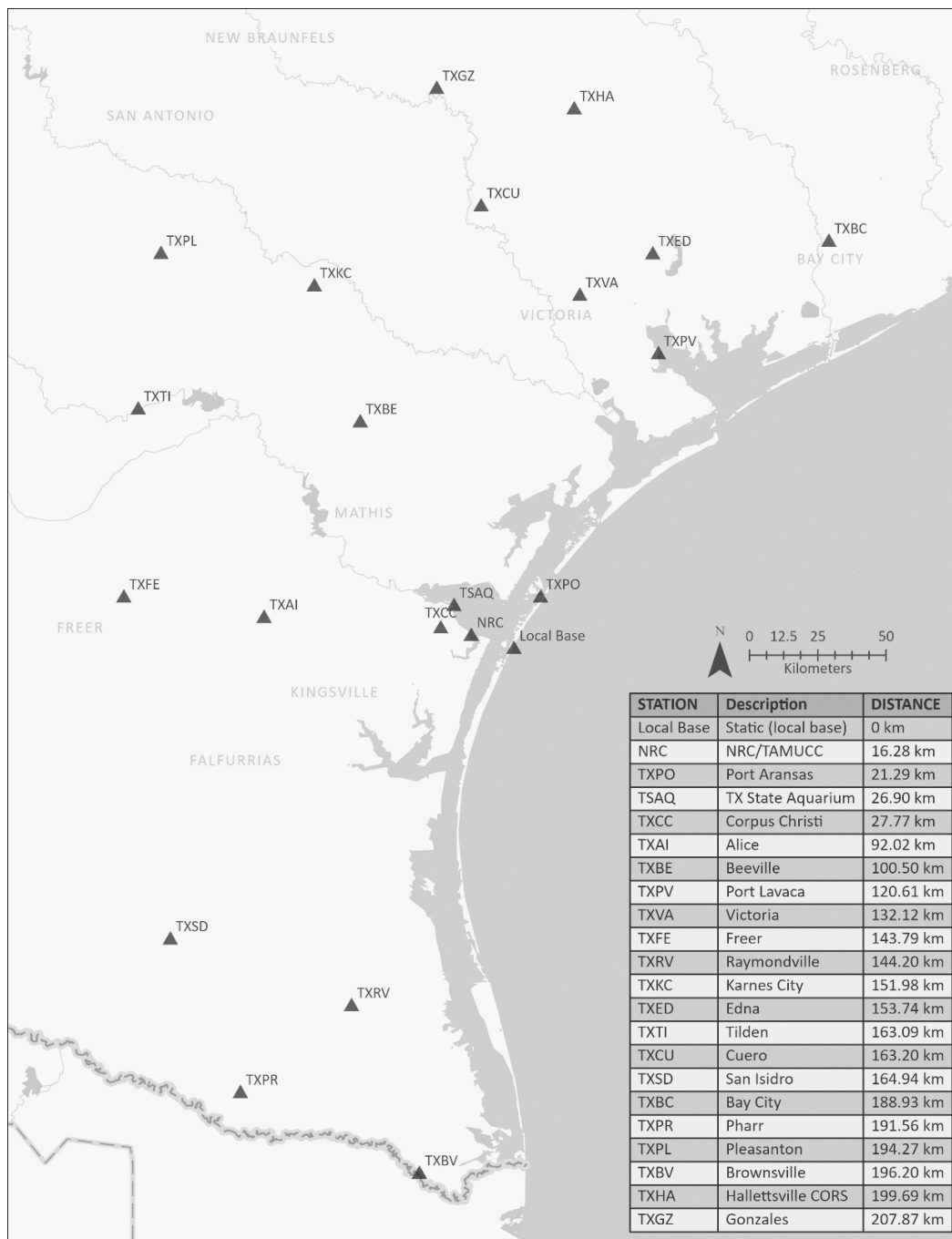


Figure 21. Local base and remote stations used for baseline distance assessment.

When using remote base stations, the source of RINEX files depends mainly on whether they are part of the CORS network or not. CORS data is usually downloaded from the User

Friendly CORS (UFCORS) online tool. However, they are automatically decimated to 30 seconds after one month as observed during this experiment and emphasized by Sickle (2015). This becomes relevant when processing GNSS data at higher sampling rates (i.e., 1 second), in which case the original files will need to be downloaded from less common sources such as the NOAA Comprehensive Large Array-Data Stewardship System (CLASS). CLASS is a free-of-charge alternative that requires the user to register an account. Table 17 shows the source of GNSS data for the base stations used in this project.

Table 17. List of the stations used for PPK data processing and their respective sources that provided information about them.

Station	Description	Distance	Source
Local Base	Local Base Static	-	GNSS Receiver
NRC	Natural Resources Center Trimble Antenna (at Texas A&M University-Corpus Christi)	16.28 km	TAMUCC GNSS Server
TXPO	Port Aransas CORS	21.29 km	CLASS
TSAQ	Texas State Aquarium Continuous GPS (cGPS)	26.90 km	LSU
TXCC	Corpus Christi CORS	27.77 km	CLASS
TXAI	Alice CORS	92.02 km	CLASS
TXBE	Beeville CORS	100.50 km	CLASS
TXPV	Port Lavaca CORS	120.61 km	CLASS
TXVA	Victoria CORS	132.12 km	CLASS
TXFE	Freer CORS	143.79 km	CLASS
TXRV	Raymondville CORS	144.20 km	CLASS
TXKC	Karnes City CORS	151.98 km	CLASS
TXED	Edna CORS	153.74 km	CLASS
TXTI	Tilden CORS	163.09 km	CLASS
TXCU	Cuero CORS	163.20 km	CLASS
TXSD	San Isidro CORS	164.94 km	CLASS
TXBC	Bay City CORS	188.93 km	CLASS
TXPR	Pharr CORS	191.56 km	CLASS
TXPL	Pleasanton CORS	194.27 km	CLASS
TXBV	Brownsville CORS	196.20 km	CLASS
TXHA	Hallettsville CORS	199.69 km	CLASS
TXGZ	Gonzales CORS	207.87 km	CLASS

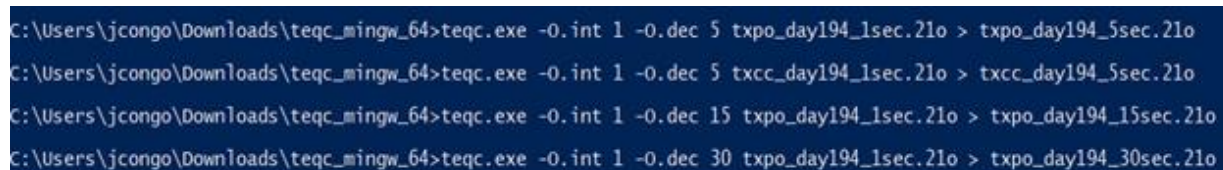
Similarly, the RINEX files that are downloaded from these sources were observation and navigation files (GLONASS and GPS). These were used in OPUS to obtain precise base location

coordinates and in WingtraHub for PPK processing. Therefore, apart from using a distinct set of base files and different base location coordinates, the overall process for the base station distance evaluation was the same as described in the previous section. All stations utilized for this test were at a 1s sampling rate and the set imagery used was the WingtraOne 120 m AGL flight. Results consist of graphs that best describe the relationship between distance and vertical accuracies.

Observation Rate of Base Station

The second PPK measure evaluated the influence of observation or sampling rate on vertical accuracies. This was accomplished by observing how these accuracies varied across different stations when using observation files at different sampling rates. The imagery used for this evaluation was also that of the WingtraOne 120 m AGL flight. This assessment followed the same general PPK workflow as the prior sections, including the implementation of both local base and remote stations. In addition, UNAVCO's TCEQ tool was used to decimate the 1s (1 Hz) observation files for each of the stations into 5s, 15s, and 30s (0.2 Hz, 0.067 Hz, and 0.033 Hz, respectively) using a TEQC tutorial drafted by Estey & Wier (2014). See Figure 22 for an example of the decimation prompt using the command line.

When performing the decimation, it is important to ensure that the command line is active, a step often overlooked when using the command line through Windows PowerShell. Also, the command must be run within the folder in which the TEQC executable is stored, and the resulting decimated files will be stored within the same directory. Results from the sampling rate evaluation consist of charts that represent the relationship between the sampling rate and vertical accuracies.



```
C:\Users\jcongong\Downloads\teqc_mingw_64>teqc.exe -0.int 1 -0.dec 5 txpo_day194_1sec.21o > txpo_day194_5sec.21o
C:\Users\jcongong\Downloads\teqc_mingw_64>teqc.exe -0.int 1 -0.dec 5 txcc_day194_1sec.21o > txcc_day194_5sec.21o
C:\Users\jcongong\Downloads\teqc_mingw_64>teqc.exe -0.int 1 -0.dec 15 txpo_day194_1sec.21o > txpo_day194_15sec.21o
C:\Users\jcongong\Downloads\teqc_mingw_64>teqc.exe -0.int 1 -0.dec 30 txpo_day194_1sec.21o > txpo_day194_30sec.21o
```

Figure 22. Example of command-line prompt used for TEQC decimation.

PPK Workflow with DJI Phantom 4 RTK

REDtoolbox was used for PPK processing using the DJI Phantom 4 RTK UAS. The workflow followed the same steps outlined in the “DJI Phantom 4 RTK GNSS Processing and Geotagging Tutorial” by AEROTAS (2018). The Phantom 4 RTK automatically creates a new folder for each set of batteries used. In this case, because two sets of batteries were used for the PPK flights, there were two folders that had to be processed through REDtoolbox, thus a total of four REDtoolbox geotagging runs. On top of the images, the base files used here are the same RINEX files used in WingtraHub (observation, GLONASS, and GPS), the timestamp file from the rover, and the observation file from the rover. The manual base position option was chosen in order to use the base station information obtained from OPUS. Results from REDtoolbox are added to a new folder within the original imagery directory. Note that restarting the program is needed if using images that require more than one battery, otherwise REDtoolbox may output all geotagged files into a single folder (the first one used), which can cause confusion and affect results. Figure 23 shows the REDtoolbox interface after adding the required files and information.

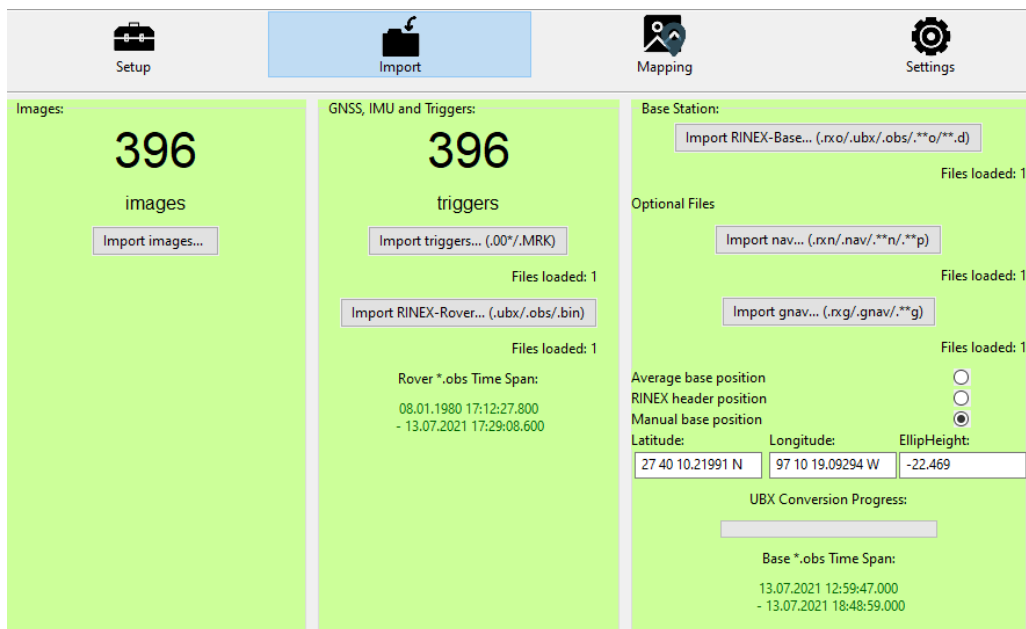


Figure 23. Screen capture of the REDtoolbox interface after importing all required files.

3.7.3. Performance of the RTK Georeferencing Technique

DJI Phantom 4 RTK data was processed in both RTK and PPK mode. This allowed for determining whether the platform could achieve plausible vertical accuracies. When operating in RTK mode, the user connects to the TxDOT RTN through a Networked Transport of RTCM via an Internet Protocol connection. In a typical situation, the platform's remote controller is connected to the Internet through a Wi-Fi hotspot or cellular modem connection. This study used the cellular approach with an AT&T SIM card. Regardless of the default WGS84 datum stated in the Exchangeable Image Format (EXIF) of the images, which the DJI populates, the TxDOT RTN uses NAD83 (2011) with ellipsoid heights. When operating in PPK mode, the RTK functionalities were disabled, and images were post-processed using PPK. Flight control was performed using the GS RTK application and PPK processing using REDtoolbox.

Because the Phantom 4 RTK was first flown in RTK mode, its resulting imagery already included RTK solutions within the imagery EXIF. Therefore, no intermediary tool is needed, and the imagery is readily processable through the SfM software.

3.7.4. Performance of the PPP Georeferencing Technique

PPP processing was performed using mainly Inertial Explorer, a software that belongs to NovAtel's Waypoint suite. The first step is to start a new project using the project wizard and saving the project under the desired folder. The user is then prompted to select the GNSS file. Unlike other PPP software such as CSRS-PPP and RTKLIB, Inertial Explorer does not require the use of SBF Converter to create an observation file. While the software can indeed use observation files, it can also work with raw GNSS files. Therefore, uploading the raw GNSS file from the rover can optimize processing and eliminate potential blunders that may occur in generating an observation file. Another benefit of using the raw file is that the rover receiver has camera events

encoded within the file, which Inertial Explorer can decode and use for PPP corrections, a functionality that is lost when using observation files instead. This is therefore another advantage of using Inertial Explorer as opposed to other PPP services such as CSRS-PPP and RTKLIB. Figure 24 shows the project wizard interface upon loading the GNSS file.

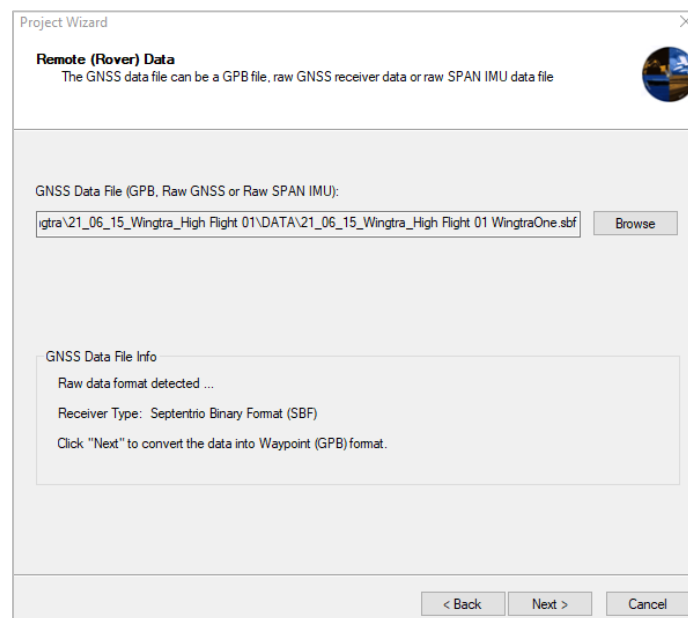


Figure 24. Screen capture of raw GNSS import wizard in Inertial Explorer.

Next, the user is prompted to specify parameters such as the antenna type, and optionally a base station file. When processing PPP, only the rover receiver data is needed. Base station information can be imported regardless, but Inertial Explorer ignores it when performing PPP processing. The WingtraOne UAS from both the 75 m and the 120 m AGL flights were used for the PPP evaluation. When the wizard steps are complete, an uncorrected map is displayed on the screen. Then, using the process tab, the user can select to process GNSS. The settings used for this test were PPP, Multi-Pass, GNSS UAV, and NAD83 (2011). These are summarized in Table 18. The Multi-Pass option maximizes convergence by passing converging Kalman filter sequentially between the various flying directions (NovAtel, 2020). This makes it possible to estimate float carrier phase ambiguities and reach better convergences. After initialization, the processing time

for a project of this size was under 20 seconds, and the software interface then shows the map with corrected points. Figure 25 shows the uncorrected and corrected maps.

Table 18. PPP processing settings in Inertial Explorer.

Processing method	Precise Point Positioning (PPP)
Processing direction	Multi-Pass
Profile	GNSS UAV
Datum	NAD83 (2011)

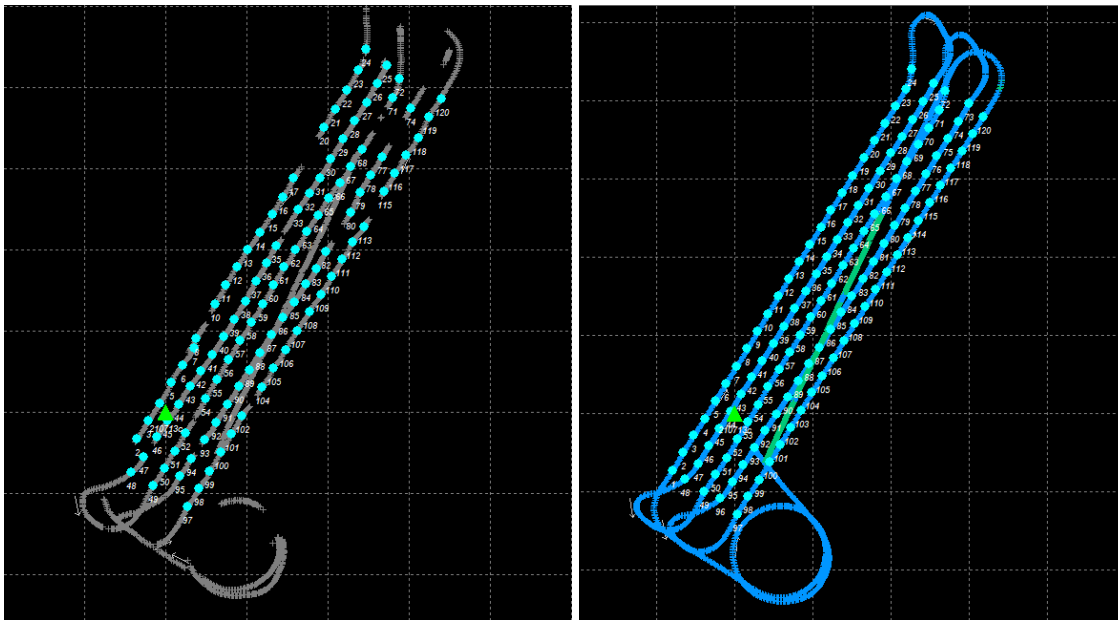


Figure 25. Inertial Explorer interface with uncorrected (left) and PPP corrected (right) points, using imagery from the WingtraOne UAS at 120m AGL.

The Export Coordinates Wizard was utilized to export the corrected coordinates. The wizard allows the user to select the information that will be included in the output and their respective formats (i.e., latitude and longitude in decimal degrees, ellipsoid heights). The output file is of text (.txt) format and can be converted into a CSV for use in the SfM software. By the time these steps are complete, the working directory will contain several files such as precise clock data, precise orbit data, and flight trajectory that the software directly downloads from either a publicly available server or a provider known as TerraStar Near Real-Time (NRT). However,

Access to TerraStar files requires additional licensing, which was not used during this study. Therefore, the publicly available precise products were used for PPP processing.

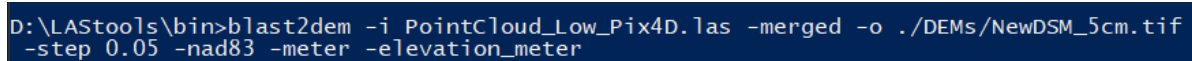
3.7.5. Data Processing

All GNSS evaluations were performed using Pix4D. The workflow essentially consisted of importing the imagery and respective geotags, setting the input coordinate system to NAD83 (2011) and the output coordinate system to NAD83 (2011) Texas South. Ellipsoid heights were used for both input and output. The template used for processing within Pix4D was the 3D Maps Template, and default settings were used that included full image scale, aerial grid, and standard calibration method. The Pix4D workflow is discussed in more detail Section 3.8.

3.7.6. Accuracy Evaluation

The accuracy of evaluation for the GNSS test was performed using ground control as checkpoints in Pix4D. These varied in terms of RTK GNSS surveyed control and total station surveyed control. Furthermore, accuracy measures were obtained from Pix4D processing reports as well as using the *LAScontrol* module of LAStools. RMSEs from the processing report are based on how well the SfM bundle adjustment fits to the tagged checkpoints within the software. *LAScontrol* provides a direct measure of the vertical accuracy of the exported dense cloud. For efficiency purposes, the use of LAStools is discussed in more detail later in this thesis.

Finally, DSMs were created using data from the WingtraOne UAS (at 75m AGL) and that of the TLS, which allowed for generating a DSM of Difference (DoD) between the two systems. Original DSMs were created using the “blast2dem” command (Figure 26) on LAStools and clipped to the same extent before being differenced against each other.



```
D:\LAStools\bin>blast2dem -i PointCloud_Low_Pix4D.las -merged -o ./DEMs/NewDSM_5cm.tif
-step 0.05 -nad83 -meter -elevation_meter
```

Figure 26. “blast2dem” command to generate DSMs in LAStools.

Another general method employed consisted of comparing ellipsoid height values from the UAS against those observed using RTK GNSS natural ground measurements. This was assessed by differencing the RTK GNSS measured value from the DSM. These measurements were acquired over four cross-shore transects (Figure 27) along the beach, running from the water line to the dune toe. The transects were spaced roughly 100 m apart alongshore, and cross-shore measurements collected at a spacing of approximately 5 meters.

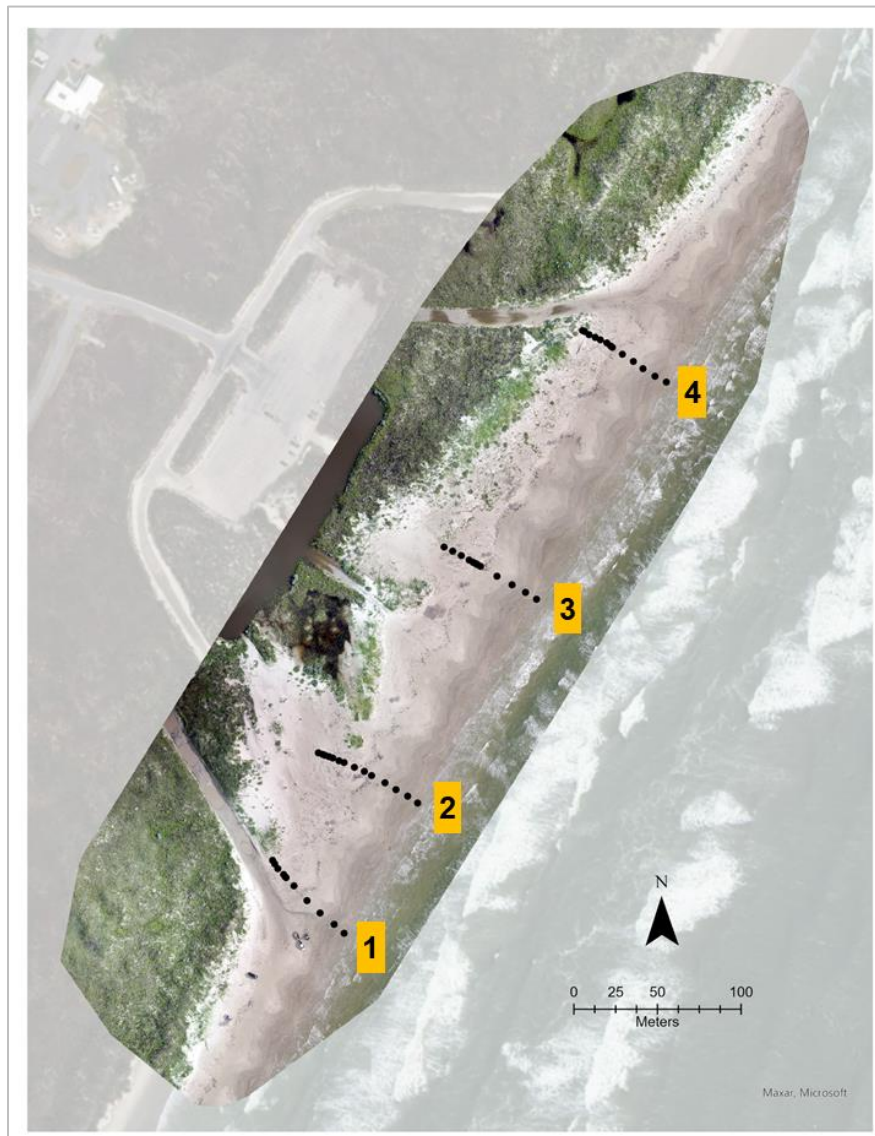


Figure 27. Path of height transects measured using RTK GNSS overlaid on top of WingtraOne UAS orthomosaic (75m AGL).

3.8. Methodology for SfM Software Evaluation

3.8.1. Overview

This section explains the influence of SfM software on UAS-SfM. It discusses the methods implemented with the SfM software tested: Drone2Map (v2.3.2), Metashape (v1.7.2), ODM (1.9.11), and Pix4D (v4.6.4), their performances, advantages, and disadvantages, and finally summarizes the main takeaways from this experiment. The section utilizes data from both North Packery Channel and Mustang Island State Park (WingtraOne UAS, 75 m AGL). For both sets of data, PPK only corrections were applied, and checkpoints are used solely for model accuracy assessment. This experiment followed the workflow depicted in Figure 28.

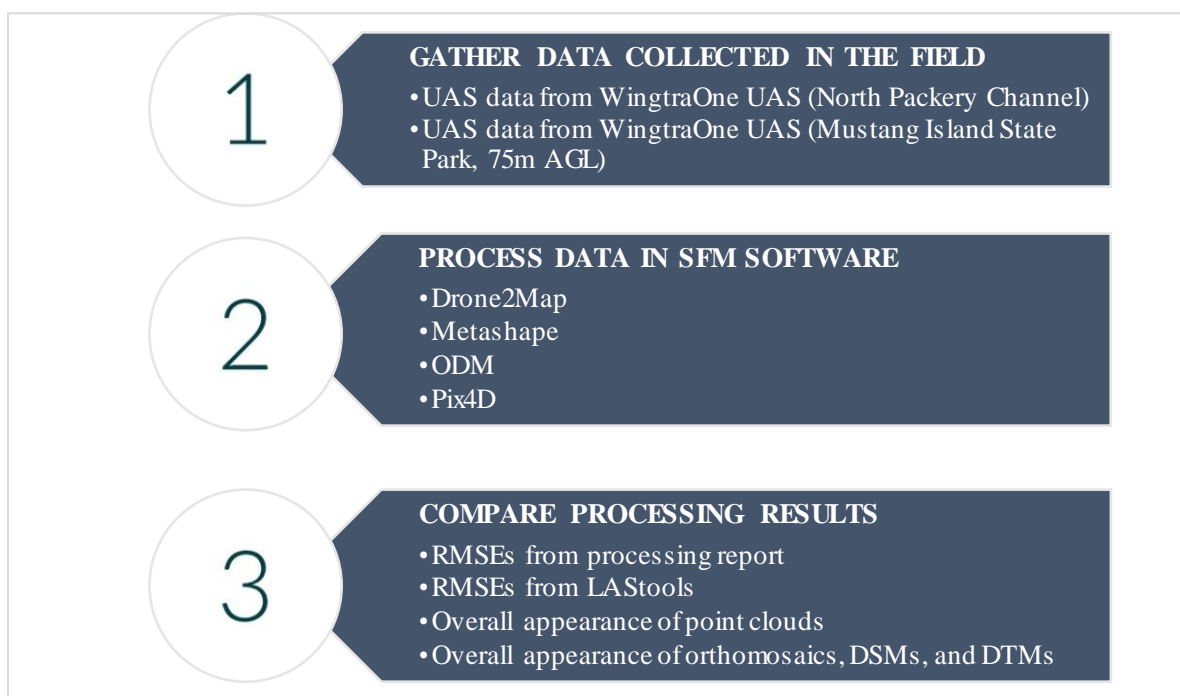


Figure 28. Workflow used for the SfM software experiment.

3.8.2. Agisoft Metashape

The Metashape workflow follows that documented in the United States Geological Survey workflow drafted by Over et al. (2021). The workflow starts with importing the UAS imagery into Metashape, importing the respective geotags, selecting the appropriate coordinate systems, and

calibrating the camera. The recommended camera and tie point accuracies were used, and the imagery aligned using the high accuracy setting so that the best estimates for camera positions were achieved. The keypoint limit was set to 60,000 and the tie point limit was set to 0 so that all matched points are kept for processing. Then, the camera was calibrated, and the camera and tie point accuracies were adjusted. The next step was to add and tag the control targets that were used as checkpoints. Next, a series of optimizations that use a least-squares bundle adjustment was employed to estimate internal and external camera orientations. Finally, the dense point clouds, DSMs, DTMs, and orthomosaics were generated. NAD83 (2011) was used as the input coordinate system and outputs referenced to NAD83 (2011) Texas South, ellipsoid heights, and a 5 cm resolution used to generate the orthomosaics, DSMs, and DTMs.

3.8.3. Pix4Dmapper

The Pix4D workflow followed mostly its default settings, with minor changes when generating orthomosaics, DSMs, and DTMs. Processing starts with adding the imagery and geotags and selecting the Standard 3D processing template. Initial processing occurs during step 1. Here, the software extracts specific features as keypoints in the images, matches these features between various images, and calibrates the internal and external parameters of the camera. This step was completed using full image scale (which utilizes full image scale for precise results), aerial grid option used for matching image pairs (which optimizes image pairs for flights flown in grid/corridor pattern), and the standard calibration method (standard settings for optimization of internal and external parameters. This resulted in a sparse 3D model that is used in subsequent steps. Checkpoints were added after the initial processing, and then the model was reoptimized.

Densification and generation of point clouds and mesh occur in step 2. Here, the software densifies the 3D model created in the previous step to create a point cloud and mesh. In this step,

the point cloud was classified to improve the DTM, and the resulting files were merged into a single file. No 3D textured mesh was generated. All other settings were left as default (half image scale, optimal point density, 3 minimum number of matches). The image scale determines the scale of images at which additional 3D points are computed. The optimal (or default) point density means that a 3D point is computed by a ratio of 4 / (the image scale size) pixels of the image used (Pix4D, 2017). For example, if the image scale is 0.125, a 3D point is computed for every 32 pixels (equivalent to 4/0.125 pixels) of the original image. Orthomosaics, DSMs, and DTMs are created in step 3. The resolution of these products was adjusted as needed. All other settings were left as default. The noise filtering option corrects erroneous points with the median altitude of neighboring points. The sharp surface smoothing preserves the orientation of the surface and keeps the sharpness of corners and edges of features such as buildings. Inverse Distance Weighting interpolation is used, in which interpolation occurs in such a way that nearby points have a larger influence on the predicted value than points farther away. Output products were also referenced to NAD83 (2011) Texas South, ellipsoid heights, and a 5 cm resolution used for orthomosaics, DSMs, and DTMs.

3.8.4. Drone2Map

The Drone2Map workflow starts by loading the software and launching the 2D Full project template. Before this, users may be prompted to log into their ESRI account before having access to the software. The current version of Drone2Map has issues handling projected coordinate systems that are not WGS84, such as in the case of this study. This can be fixed by either using GCPs to georeference the model or converting the checkpoints to WGS84. This project used the latter option. This allowed the imagery to be loaded in WGS84 and final products georeferenced to WGS84 Universal Transverse Mercator (UTM) Zone 14N.

Because Drone2Map has the same algorithm as Pix4D, processing parameters were selected to match the choices described previously in the Pix4D section. However, Drone2Map has four major steps: initial, dense, 2D Products, and 3D Products. The initial and 2D Products steps are equivalent to Pix4D's steps 1 and 3, respectively. Unlike Pix4D, Drone2Map splits the densification step and the point cloud generation into two: first, the densification occurs, and then the 3D products (i.e., point cloud and mesh) are generated. Despite this difference, it was still possible to set the parameters between Drone2Map and Pix4D similar to each other. The resulting products were also referenced in ellipsoid heights and output using a 5 cm resolution.

After a brief correspondence with an ESRI representative at the American Geophysical Union Conference in 2021 and the ASPRS Conference in 2022, it was determined that ESRI is working to update the algorithm that is currently used by Drone2Map, which is likely to solve the issues it currently has with non-WGS84 systems. Part of this change includes the discontinuity of the Pix4D algorithm and the adoption of another that offers more robustness. This is a development that will be followed closely.

3.8.5. OpenDroneMap

Usage of ODM is pertinent to installing the required dependencies (GitHub, Docker, and Python). The process of installation followed the ODM installation guide scripted by Toffanin (2020). All processing is done on a web browser (hence the name WebODM, see Figure 29) and the first step is to change the processing node hostname from default (usually “webodm-node-odm-1”) to the IP address of the computer being used for processing. The IP address can be found by opening the Windows PowerShell and typing the command “docker network inspect odm_default.” This command will print information for various containers, and the IP address of interest here is the one under “odm_node-odm-1.” Copy and paste only the numbers that appear

before the backslash. Processing can start after changing the hostname to the IP address and saving the changes. Recall that ODM used imagery with PPK corrections embedded in their EXIF.

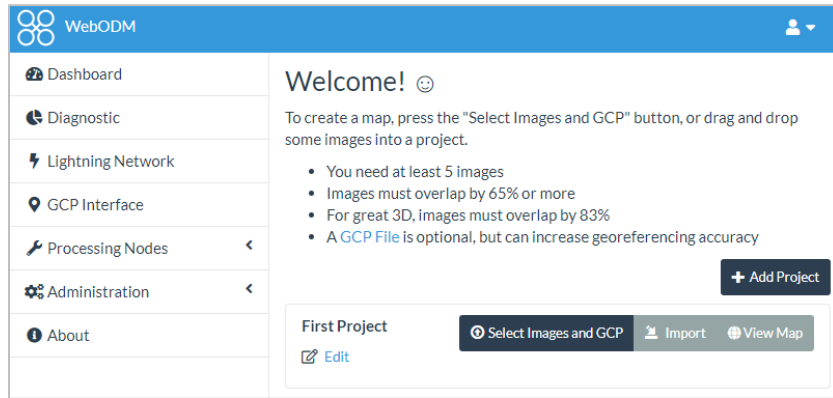


Figure 29. Screen capture of the Interface of ODM.

After starting a new project and importing the images, the user needs to adjust the processing parameters as needed. Unlike the other SfM software, the current version of ODM requires that this adjustment take place before processing begins, equivalent to batch processing. Table 19 shows the options that were changed from their defaults. Refer to Figure 30 for an example of the ODM user interface during parameter selection and processing, and Figure 31 shows an example of the ODM interface once processing begins.

Table 19. Processing parameters that were changed during ODM processing.

Parameter	Function	Changed to
debug	Prints error messages.	Enable
dem-resolution	Sets the resolution for DSM and DTM.	0.05 m
dsm	Generates a digital surface model.	Enable
dtm	Generates a digital terrain model.	Enable
force-gps	Forces imagery GPS data to be used for reconstruction even if GCPs are added to the project.	Enable
ignore-gsd	Caps the maximum resolution of image outputs.	Enable
optimize-disk-space	Deletes heavy intermediate files to optimize disk space usage. Helpful when using computers with limited disk space available.	Enable
orthophoto-resolution	Sets the resolution for the orthomosaic.	0.05 m
pc-classify	Classifies the point cloud outputs using a simple morphological filter.	Enable
pc-rectify	Rectifies point clouds: wrongly classified points are reclassified, and gaps are filled. Useful for DTMs.	Enable

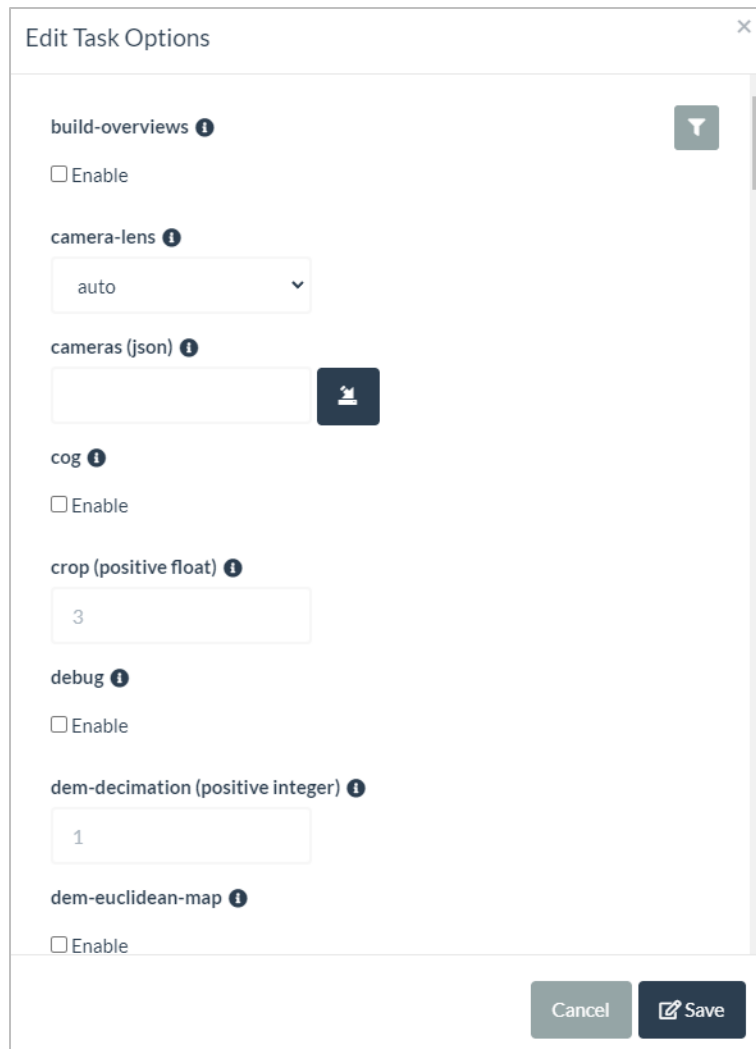


Figure 30. Example of ODM screen showing some of the processing parameters.

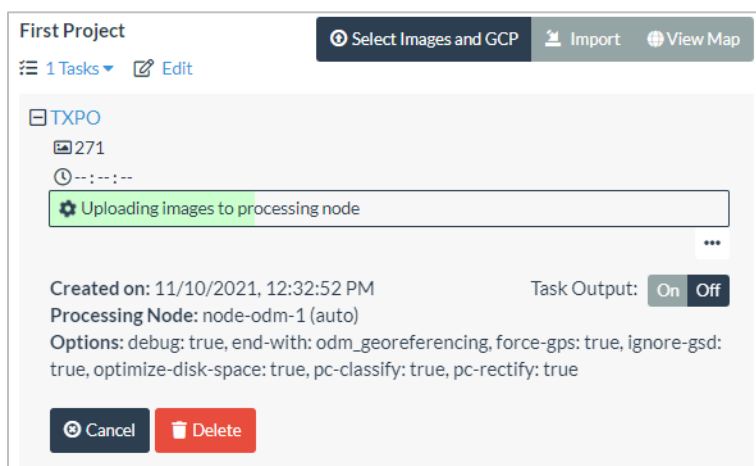


Figure 31. Example of ODM interface during processing.

As mentioned previously, ODM was processed using coordinate information embedded into the imagery EXIFs as opposed to an external CSV file. Attempts were made to use external CSVs, which led to processing failure. Furthermore, the process of ground control tagging in ODM is more complex than in its counterparts. Targets need to be tagged on the GCP Interface menu of the software, and tagging properties exported as a text file before being loaded along with the input imagery. A more efficient and increasingly popular alternative is to mark the first target, next export the text file, and finally reopen the file and continue to edit the file for the remaining targets. However, this process is more prone to blunders, thus extreme caution is needed.

The version of ODM tested in this study only supports the use of GCPs for georeferencing but not as checkpoints for evaluating the accuracy of UAS-SfM models. After correspondence with the software's lead developers, a feature request has been added that would enable this functionality, but there is currently no estimate of when that will be accomplished. In the interim, accuracy can be evaluated using other tools and software, hence the use of *LAScontrol* in this study. Moreover, ODM works in WGS84 by default, and the coordinate system used cannot be controlled or adjusted through the input parameters. This means that like Drone2Map, the resulting products were in WGS84 UTM Zone 14N, with ellipsoid heights, and a resolution of 5 cm. At the end of processing, products (i.e., point cloud) can be downloaded as a zip folder and extracted for use in software such as ArcGIS Pro and CloudCompare.

3.8.6. Accuracy Evaluation

The first accuracy evaluation in this section was made in terms of RMSEs from processing reports given by the software used. Processing reports, which rely on bundle block adjustment, are not used for ODM runs because the values provided in the report may not be accurate when using checkpoints, though they are when using GCPs. The second accuracy assessment is made via

results from *LAScontrol*. Recall from earlier sections that the processing report describes how well the SfM bundle adjustment solution fits the checkpoints tagged in the SfM software used, while *LAScontrol* directly measures the vertical accuracy of the dense point cloud exported from the SfM software. Figure 32 shows an example of *LAScontrol* being used to calculate the vertical accuracies of a UAS-SfM model using a point cloud generated within Pix4D.

```
lascontrol -i PointCloud_Low_Pix4D.las -cp Control_TS.csv -step 0.3048 -meter -parse xyz -cp_out  
PointCloudReport_Pix4D.txt
```

Figure 32. Example of *LAScontrol* prompt to calculate vertical RMSEs from the point cloud.

Metashape and Pix4D used the original control values as defined via RTK GNSS while Drone2Map and ODM used ground control that was converted to WGS84 UTM Zone 14N due to anomalies associated with the two software when using non-WGS84 systems. It must be emphasized that there is an issue with *LAScontrol* that yields the wrong units of measure when computing the RMSEs (i.e., showing 1.2 feet when it should be 1.2 meters). Manual RMSE computations were conducted to ensure that the value given is correct and only the unit label is wrong, and it was concluded that it was indeed the case: the value itself was correct but the label was not. This issue has been reported to the developers.

Finally, qualitative observations were made on the resulting point clouds, orthomosaics, DSMs, and DTMs generated with the different software. CloudCompare and ArcGIS Pro were used for visualization purposes.

CHAPTER IV

RESULTS AND DISCUSSION

4.1. GNSS Georeferencing Techniques

4.1.1. PPK Evaluation Results – WingtraOne UAS

Distance of Base Station

Overall, the accuracy of PPK processing was inversely proportional to the distance between the survey site and the base station utilized. Figure 33 shows the increase in RMSEs as the baseline distance increased. This figure uses the WingtraOne imagery at 120 m AGL and different base stations at a 1s sampling rate.

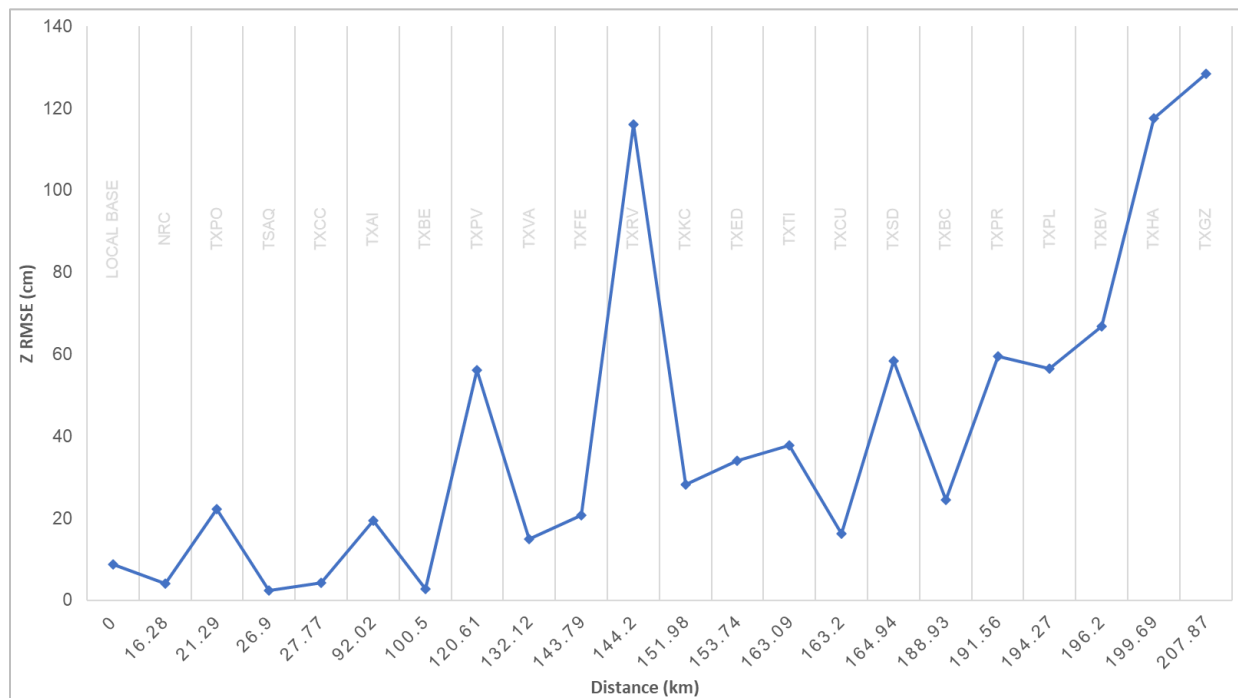


Figure 33. Vertical RMSEs for base stations located at different distances (WingtraOne UAS, 120m AGL, PPK only solutions, at 1s sampling rate. This chart is not scaled to account for the spatial distance between the stations). RMSEs from Pix4D processing report, accuracies relative to total station checkpoints.

Observe that the RMSEs for base stations located at shorter distances are lower than those at farther distances. For example, the local base yielded an RMSE of 8.85 cm while Gonzales had 1.28 m. Another example is the Corpus Christi station, which reached 4.31 cm compared to Kames City's 28.32 cm. Except for the local base (8.85 cm) and TXPLO (22.16 cm), the stations located within 30 m of the study area yielded vertical RMSEs of less than 5 cm. The slightly higher RMSEs at the local base are hypothesized to have been caused by its placement on sand/beach, which is not a stable structure. However, efforts were conducted to avoid or at least minimize displacement. After several processing runs, the 22.16 cm RMSE for TXPO is believed to have been a potential fault with the station at the time of the survey that affected the 1s sampling rate more than others.

Figure 34 shows the linear ($R^2 = 0.51$) and exponential ($R^2 = 0.63$) fits of the relationship between RMSEs and baseline distances. The figure uses the WingtraOne imagery at 120 m AGL and a 30s sampling rate and baseline distances. R^2 is the coefficient of determination and explains the correlation between two variables. The higher the R^2 the stronger the correlation.

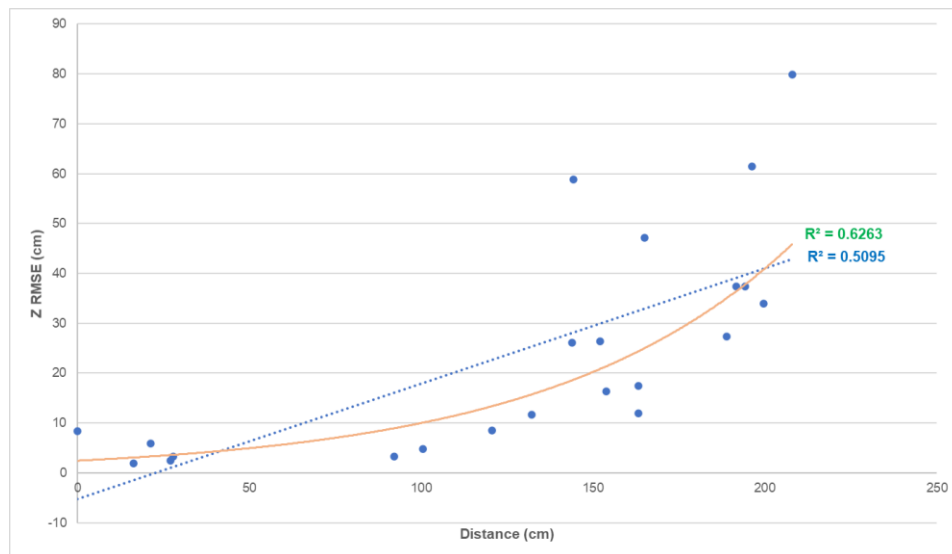


Figure 34. Trendlines for RMSE vs Distance (WingtraOne UAS, 120m AGL, PPK only solutions, 30s sampling rate). RMSEs from Pix4D processing report, accuracies relative to total station checkpoints.

Figure 35 shows the same relationship with the local base excluded. With the local base excluded, the linear and exponential fit changed slightly and the new R^2 values were 0.52 and 0.62, respectively.

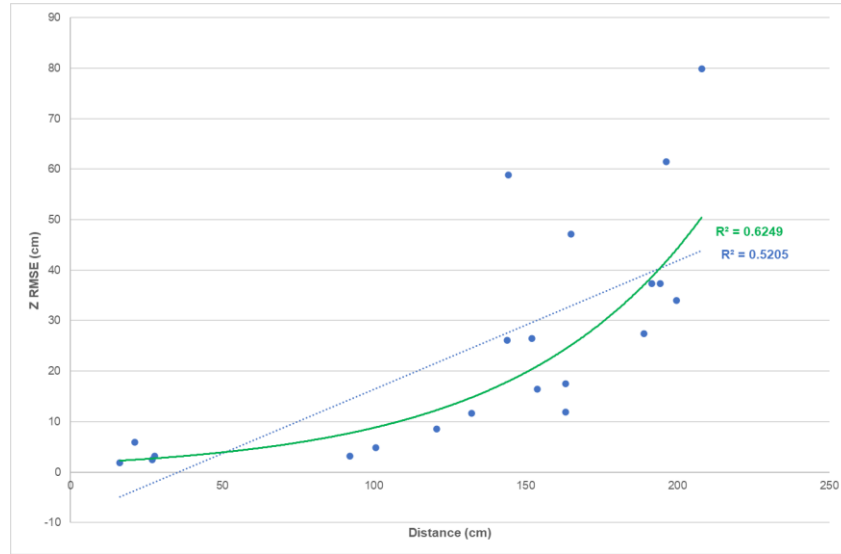


Figure 35. Linear and exponential fits for RMSE vs Distance with the local base excluded (WingtraOne UAS, 120m AGL, PPK only solutions, 30s sampling rate). RMSEs from Pix4D processing report, accuracies relative to total station checkpoints.

Observation Rate and PPK Fix Percentage

Interesting results were obtained when assessing the impact of different sampling rates on RMSEs. The results obtained were not as straightforward as anticipated since no clear pattern or uniformity was observed. As shown in Figure 36, a given sampling rate could lead to the highest accuracy in one station while failing to do so in another. For instance, at times when 30s performed better than 1s (i.e., the local base yielded 8.85 cm at 1s and 8.36 cm at 30s) and other times the contrary happened (i.e., the TXBC station yielded 24.56 cm at 1s and 27.38 cm at 30s). Although no clear pattern was achieved, overall, sampling rates of 5s and 30s achieved higher accuracies than 1s and 15s. The cumulative RMSEs for each of the sampling rates used yielded 900.03 cm for 1s, 619.77 cm for 5s, 648.79 cm for 15s, and 531.89 cm for 30s.

While this study ensured that the receivers were free of obstructions and operated as efficiently as possible, there are factors such as the presence of a brief storm on the day of the survey, and potential multipath that might have been present in some of the remote base stations, that may have contributed to receiver-recorded noise, which becomes more detectable at a higher sampling rate. This is similar to observations made by Erol et al. (2020), who gathered GNSS data for 4 hours and used TEQC to decimate a 0.1-second observation file into 0.2s, 1s, 5s, 15s, and 30s. They processed the static data using CSRS-PPP and found that higher sampling rates are essential to identify dynamic movements of structures but not necessary to achieve high GNSS accuracies. In their study, higher rates led to low-level solutions. While the study deviates slightly from this project for using PPP processing instead of PPK, the nature of the issue is comparable since it uses static GNSS data (observation, and GPS and GLONASS navigation files).

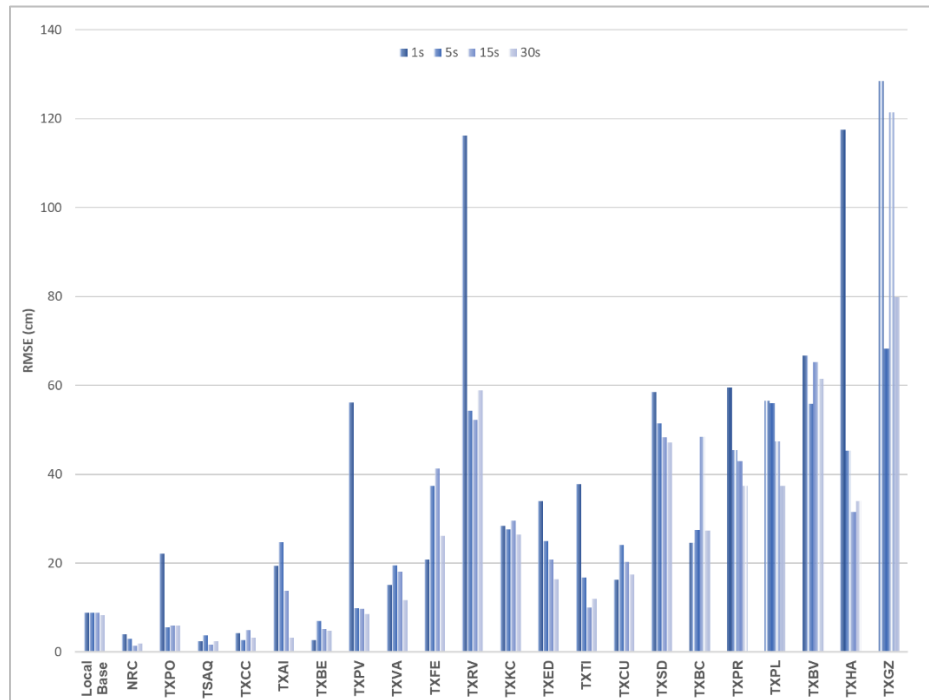


Figure 36. RMSEs results for different base stations and sampling rates (WingtraOne UAS, 120m AGL, PPK only solutions). RMSEs from Pix4D processing report, accuracies relative to total station checkpoints.

Tests suggest that when evaluating the use of different base stations, the PPK fix percentage may take precedence over the sampling rate. According to Wingtra (n.d.), the PPK fix percentage is the percentage of UAS images that have been corrected using PPK solutions. Results showed that higher percentages yield the lowest RMSEs. This is best described in Figure 37, where points located closer to a PPK fix of a hundred percent yielded lower RMSEs than others, regardless of the sampling frequency. Additional testing showed that the PPK fix percentage decreases as the base station distance increases (i.e., the local base has 100% fix at 1s while Gonzales had 0%) and can irregularly vary for the same station when using different sampling rates (i.e., Alice having 68.33% fix at 1s, 45.83% at 5s, 72.50% at 15s, and 69.17% at a 30s rate). Refer to the appendices for more information about each station's RMSE, distance, and PPK fix percentage.

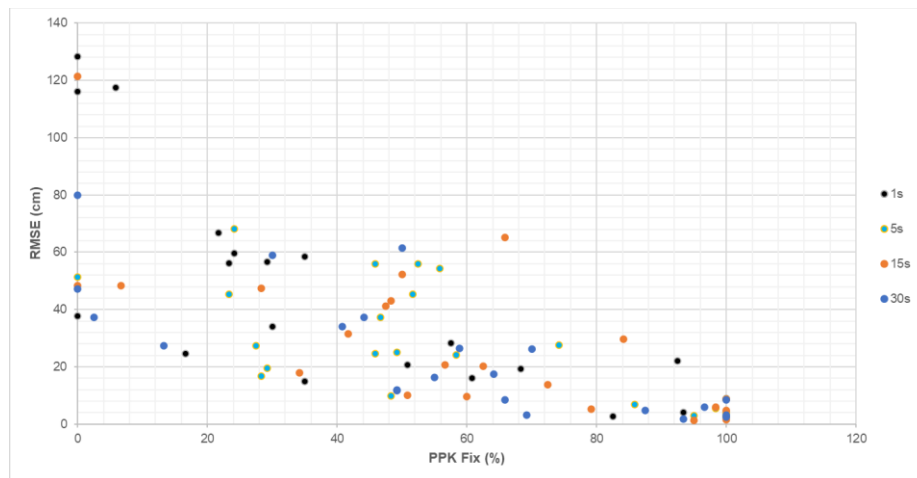


Figure 37. Influence of PPK fix percentage on vertical RMSEs (WingtraOne UAS, 120m AGL, PPK only solutions). RMSEs from Pix4D processing report, accuracies relative to total station checkpoints.

RTK GNSS vs Total Station

PPK solutions were also evaluated in terms of accuracy when using checkpoints surveyed with RTK GNSS in comparison to checkpoints surveyed with a total station. Minimal differences were observed: the total station measurements were more consistent than the RTK observations.

Tests were performed using 1 s and 30 s sampling rates at the local base using the WingtraOne flight at 120 m AGL, and the results are presented in Figure 38 and Table 20. The vertical RMSEs for the total station surveyed points were 8.85 cm at 1 s and 8.36 cm at 30 s. Similarly, the RMSEs for the RTK-observed targets were 8.66 cm at 1 s and 8.16 cm at 30 s. The standard deviation for the total station control was 1.42 cm at 1 s and 1.31 cm at 30 s. The standard deviation for the RTK measurements was 2.42 cm at 1 s and 2.27 cm at 30 s.

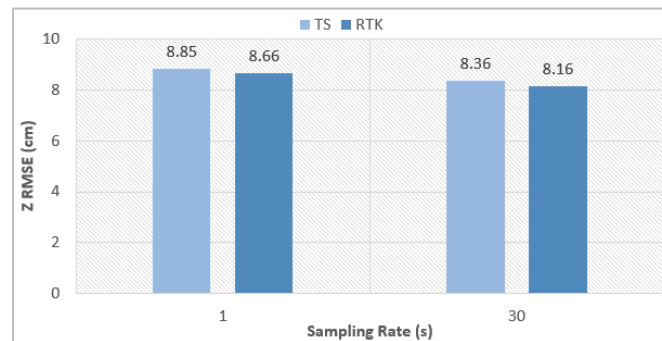


Figure 38. RMSEs for total station vs RTK surveyed control (WingtraOne UAS, 120m AGL, PPK only at 1 s and 30 s). Results from Pix4D processing report.

Table 20. Statistic measures for Total Station and RTK surveyed ground control using the local base station. Uses imagery of WingtraOne UAS flight at 120m AGL. Results from Pix4D processing report, accuracies relative to total station checkpoints.

Survey Mode	Rate	Mean	Sigma	Z RMSE
Total Station	1s	-8.74 cm	1.42	8.85
Total Station	30s	-8.26 cm	1.31	8.36
RTK	1s	-8.32 cm	2.42	8.66
RTK	30s	-7.84 cm	2.27	8.16

This is tied to the SurvNET material discussed in earlier sections. The lower standard deviation values suggest greater precision or consistency amongst the total station points, thus good local accuracy precision. The lower RMSEs for RTK surveyed points suggest that the RTK survey may have better global accuracy. It must be emphasized that the accuracy of the total station

survey ultimately depends on RTK GNSS because all results are tied to the temporary setup points that were established using GNSS

4.1.2. PPK Evaluation Results – DJI Phantom 4 RTK

PPK-only solutions for the Phantom 4 RTK imagery were obtained using REDtoolbox, and the local base station at Mustang Island State Park (1s sampling rate). Results obtained from the Pix4D processing report (Table 21) yielded a vertical RMSE of 8.44 cm, which was only 4 mm lower than its WingtraOne counterpart at the same base station and sampling rate.

Table 21. Statistic measures for DJI flight in PPK mode. Uses local base station, results from Pix4D processing report, accuracies relative to total station checkpoints.

Mode	Rate	Z RMSE
PPK	1s	8.44 cm

4.1.3. RTK Evaluation Results

RTK solutions were obtained using the TxDOT RTN. As explained earlier, the captured imagery's coordinates were automatically corrected using RTK as they were captured. Therefore, the images were ready for processing in Pix4D as soon as they were retrieved from the UAS platform. The vertical RMSE for this dataset was 7.27 cm. See results in Table 22.

Table 22. Statistic measures for DJI flight in RTK mode. Uses results from Pix4D processing report, accuracies relative to total station checkpoints.

Mode	Rate	Z RMSE
RTK	1s	4.27

4.1.4. PPP Evaluation

PPP tests consisted of using WingtraOne UAS imagery at 75 m AGL and 120 m AGL. As read from the Pix4D processing report, PPP processing results (Figure 39) were 32.86 cm and 90.80 cm for flying heights of 75 m and 120 m, respectively. As expected, larger RMSEs are

experienced when flying the platform at a higher altitude. After PPP processing, Inertial Explorer contains several plots that help users understand how well the workflow performed. While there are several plots available, the next paragraphs in this section explore some of the plots obtained from the 120 m flight that are worth discussing. The first of these plots is the number of satellites available, and as shown in Figure 40, there was indeed a good availability of satellites throughout the entire flight, except for a brief period right after takeoff when no satellites were detected.

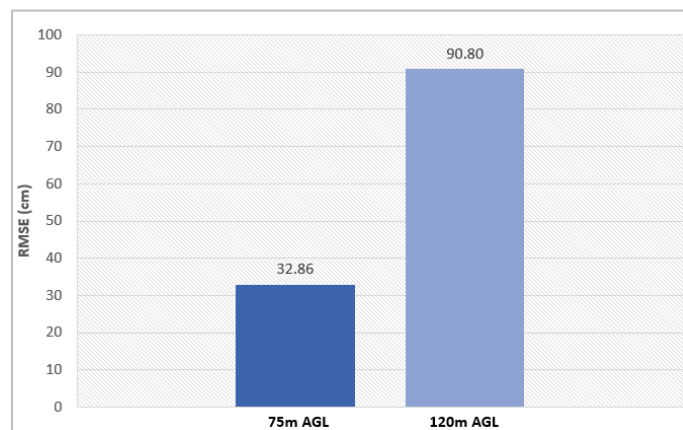


Figure 39. PPP results for WingtraOne UAS flights at altitudes 75m and 120m AGL. RMSEs from Pix4D processing report, accuracies relative to total station checkpoints.

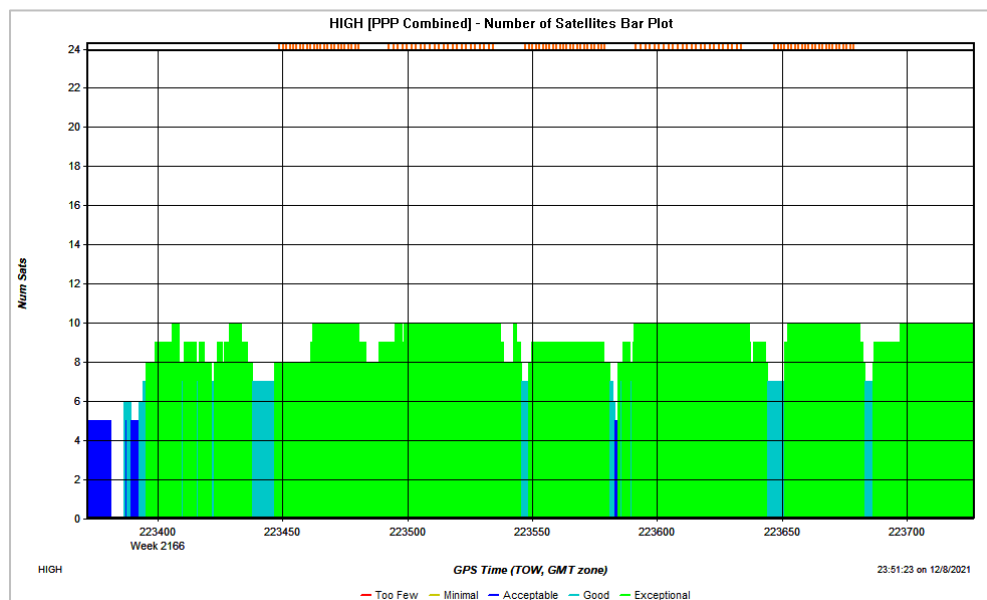


Figure 40. Number of satellites available during flight time (generated in Inertial Explorer).

The PDOP graph in Figure 41 suggests that there was good satellite geometry for most of the flight duration. The green color represents exceptional geometry. As seen in the graph, the PDOP value was mostly under 1.45. Apart from a few peaks that reached 1.65, the only gap occurred at the same time while no satellite was detected and there was a relatively higher peak (2.70) immediately before the end of the flight. Observe that the PDOP values in this figure are mostly less than 2, which is consistent with the predictions obtained from Trimble GNSS planning before the field survey (recall Figure 14). Once again, this consistency suggests good satellite geometry for the period that the survey was conducted.

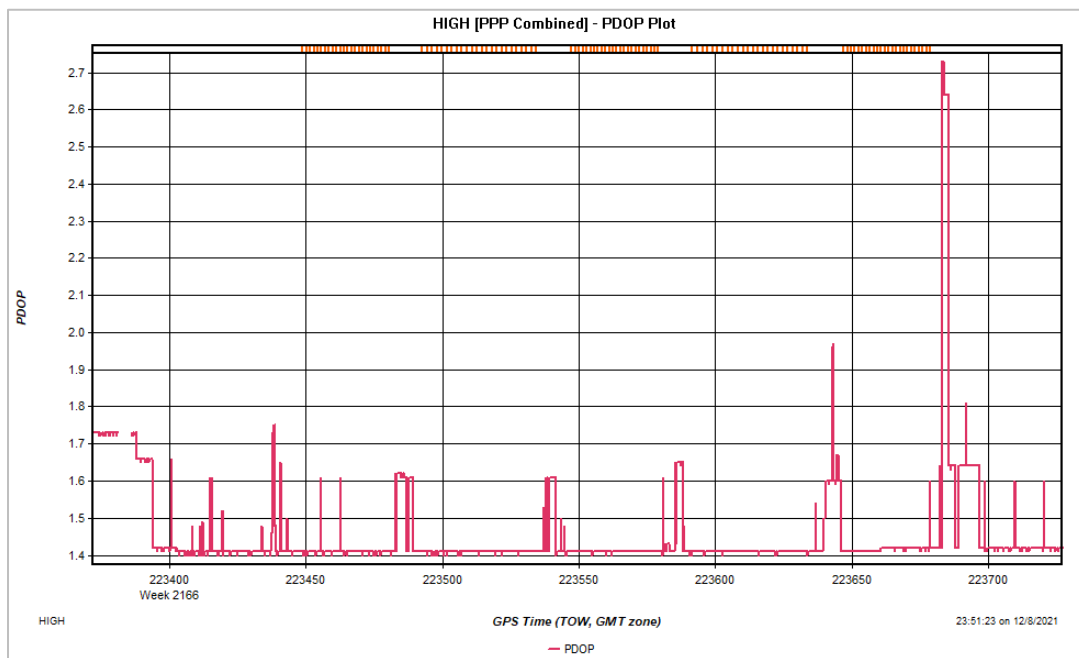


Figure 41. PDOP measure throughout flight time. Graph generated in Inertial Explorer.

Finally, the height profile in Figure 42 shows the expected flight pattern, as its height relative increases from approximately -23 m relative to the ellipsoid (which represents ground level) to roughly 105 m (± 4 m) also relative to the ellipsoid and holds that approximate height until the end of the flight. Therefore, this plot can serve as confirmation of that flying altitude. The height profile also reflects the brief period when no satellite information was available.



Figure 42. Height profile throughout flight time. Graph generated in Inertial Explorer.

4.1.5. Supplementary Results

DSM of Differences

DSMs from the low altitude WingtraOne UAS flight and the TLS were differenced to map the areas of Mustang Island State Park to map the performance of the two systems across the study area. The DSMs used for the DoD are shown in Figure 43 and the result from the calculation is shown in Figure 44. Comparable results were obtained from the DoD, however, differences in height were observed along the western edge of the mapped area. This was caused by the UAS and the TLS having different reach. Because the UAS was operated above the study area, it was able to thoroughly see the top of vegetation and the man-made structures (i.e., picnic tables and chairs) that were located in the area better than the TLS, consequently leading to a range of -6.58 m and 3.31 m. For this specific clipped area, the DoD yielded a mean of approximately 8 mm. These values are summarized in Table 23.

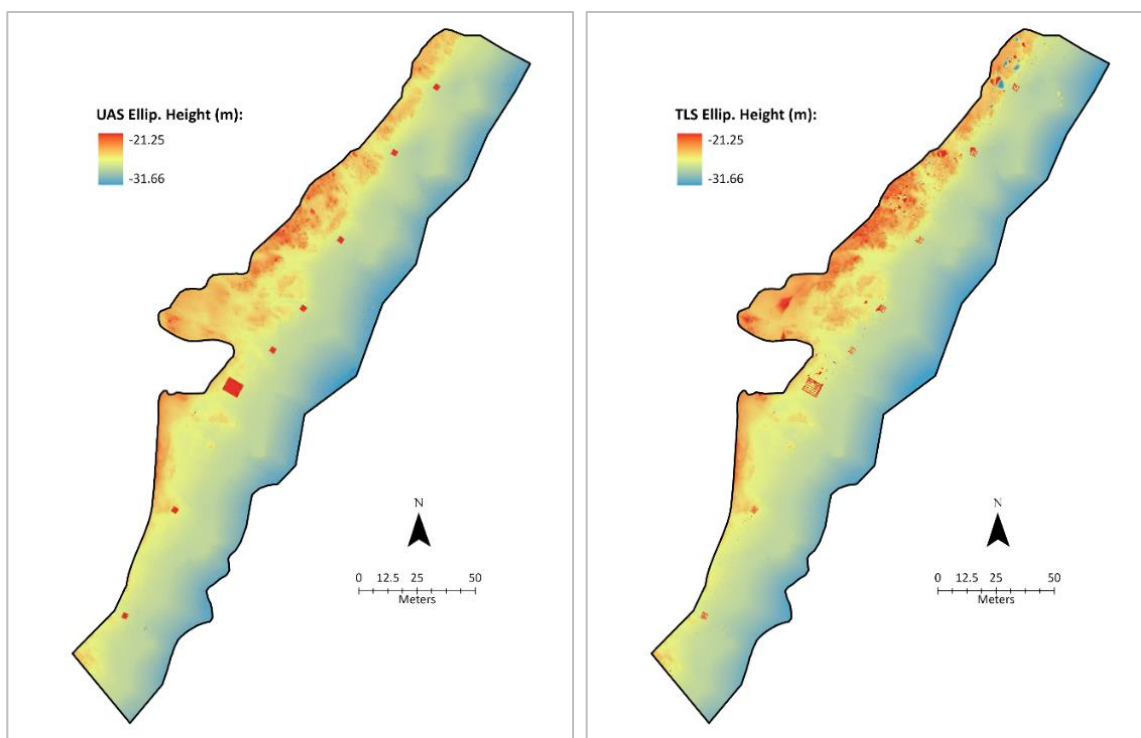


Figure 43. WingtraOne UAS DSM (75 m AGL) vs TLS DSM. DSMs of 5 cm resolution.

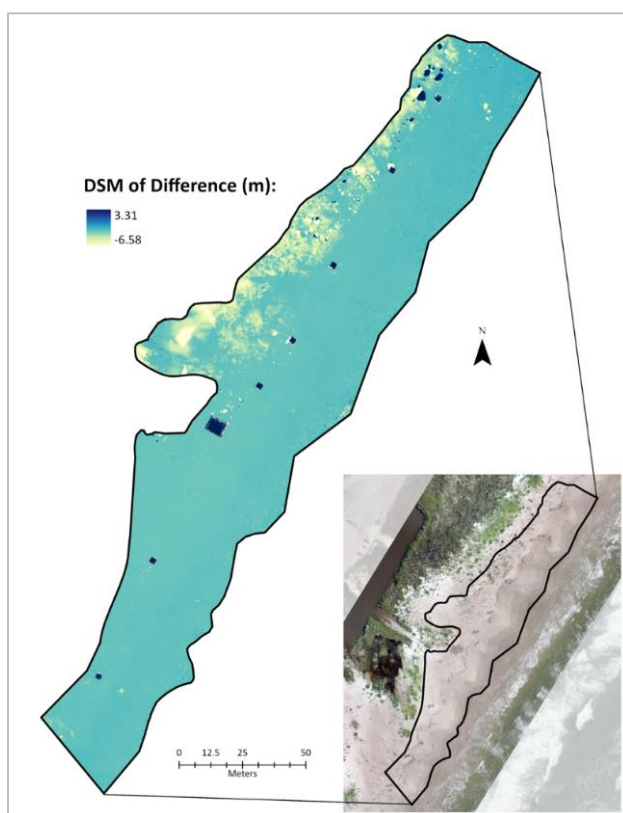


Figure 44. DSM of Differences (5 cm resolution).

Table 23. Statistics of DSM of Differences.

Range (m)	-6.58 to 3.31
Mean (m)	0.008
RMSE (m)	0.16

These statistics are influenced by the extent of the clipping area. For example, reducing the western region would reduce the range between minimum and maximum values as it would further remove noisy points from the dataset and likely have an impact on the overall mean and RMSE. Nevertheless, the results obtained from this DoD serve as good measures that the UAS flight and the TLS accuracies do not differ significantly.

DSM vs RTK GNSS

Overall, the differences between the two were within centimeter-level, with means across all transects between 0.055 m and 0.093 m. The mean of differences yielded 0.08 m (transect 1), 0.055 m (transect 2), 0.072 m (transect 3), and 0.093 m (transect 4). Table 24 and Table 25 summarize these differences, and Figure 45 shows the height profiles for each of the transects.

Table 24. Height differences between WingtraOne UAS DSM (75m AGL) and RTK GNSS measurements.

	TRANSECT 1 (m)					TRANSECT 2 (m)					TRANSECT 3 (m)					TRANSECT 4 (m)				
	Point #	UAS	RTK	Diff	DiffSqd	Point #	UAS	RTK	Diff	DiffSqd	Point #	UAS	RTK	Diff	DiffSqd	Point #	UAS	RTK	Diff	DiffSqd
	Point 1	-25.359	-25.490	0.131	0.017	Point 12	-25.504	-25.525	0.021	0.000	Point 26	-25.511	-25.548	0.037	0.001	Point 38	-25.383	-25.471	0.088	0.008
	Point 2	-25.208	-25.282	0.074	0.005	Point 13	-25.241	-25.286	0.045	0.002	Point 27	-25.203	-25.228	0.025	0.001	Point 39	-25.178	-25.290	0.112	0.012
	Point 3	-24.896	-24.983	0.087	0.008	Point 14	-25.028	-25.099	0.071	0.005	Point 28	-24.952	-25.030	0.077	0.006	Point 40	-24.923	-25.028	0.105	0.011
	Point 4	-24.697	-24.775	0.077	0.006	Point 15	-25.028	-24.926	-0.102	0.010	Point 29	-24.741	-24.816	0.075	0.006	Point 41	-24.720	-24.809	0.089	0.008
	Point 5	-24.532	-24.609	0.077	0.006	Point 16	-24.697	-24.766	0.069	0.005	Point 30	-24.602	-24.678	0.076	0.006	Point 42	-24.611	-24.700	0.089	0.008
	Point 6	-24.440	-24.510	0.070	0.005	Point 17	-24.598	-24.658	0.060	0.004	Point 31	-24.542	-24.615	0.072	0.005	Point 43	-24.536	-24.619	0.083	0.007
	Point 7	-24.333	-24.394	0.061	0.004	Point 18	-24.461	-24.533	0.072	0.005	Point 32	-24.352	-24.413	0.061	0.004	Point 44	-24.311	-24.374	0.062	0.004
	Point 8	-24.423	-24.498	0.075	0.006	Point 19	-24.341	-24.391	0.050	0.003	Point 33	-24.541	-24.618	0.077	0.006	Point 45	-24.257	-24.352	0.095	0.009
	Point 9	-24.305	-24.375	0.069	0.005	Point 20	-24.344	-24.415	0.072	0.005	Point 34	-24.303	-24.401	0.098	0.010	Point 46	-24.236	-24.317	0.081	0.007
	Point 10	-24.137	-24.209	0.072	0.005	Point 21	-24.304	-24.379	0.075	0.006	Point 35	-24.227	-24.318	0.091	0.008	Point 47	-24.044	-24.143	0.099	0.010
	Point 11	-24.017	-24.103	0.086	0.007	Point 22	-24.258	-24.343	0.085	0.007	Point 36	-24.324	-24.412	0.088	0.008	Point 48	-23.957	-24.058	0.101	0.010
	-	-	-	-	-	Point 23	-24.210	-24.297	0.087	0.007	Point 37	-24.401	-24.493	0.092	0.009	Point 49	-23.827	-23.910	0.083	0.007
	-	-	-	-	-	Point 24	-24.078	-24.158	0.081	0.007	-	-	-	-	-	Point 50	-23.647	-23.764	0.117	0.014
	-	-	-	-	-	Point 25	-24.186	-24.278	0.092	0.008	-	-	-	-	-	-	-	-	-	-
Mean	-	-24.577	-24.657	0.080	-	-	-24.591	-24.647	0.055	-	-	-24.642	-24.714	0.072	-	-	-24.433	-24.526	0.093	-
Std Dev.	-	0.406	0.417	0.018	-	-	0.427	0.403	0.047	-	-	0.380	0.362	0.021	-	-	0.502	0.502	0.014	-
RMSE		0.082					0.073					0.075					0.094			

Table 25. Mean, standard deviation, and RMSEs of height differences between WingtraOne UAS DSM (75m AGL) and RTK GNSS.

	Transect 1	Transect 2	Transect 3	Transect 4
Mean of differences (m)	0.080	0.055	0.072	0.093
Std. dev. of differences (m)	0.018	0.047	0.021	0.014
RMSE (m)	0.082	0.073	0.075	0.094

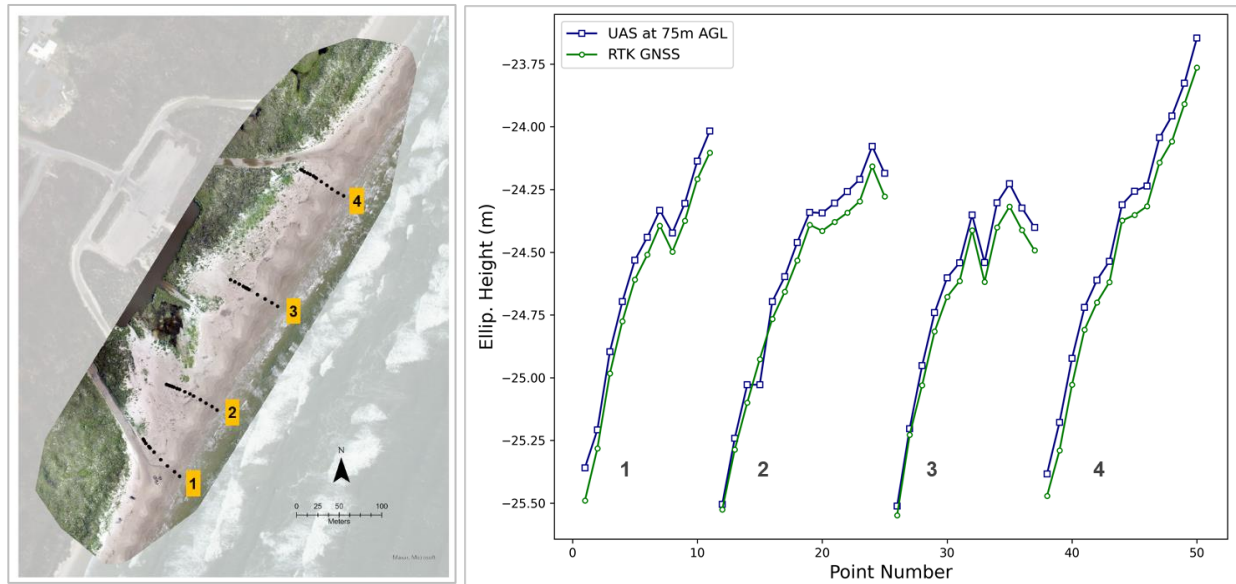


Figure 45. Height difference among four RTK GNSS transects compared to the WingtraOne UAS flight (75 m AGL).

Autonomous vs GCPs

For comparative purposes, it was important to show how accuracy is affected by using GCPs for georeferencing the UAS imagery both on autonomous or uncorrected imagery and on PPK-corrected imagery. To generate autonomous geotags, WingtraHub was used without selecting the “PPK processing option,” as discussed in the methodology. Recall that when not using this option, no base station or base location is needed in WingtraHub.

Pix4D was used for this stage of the study. Both the autonomous and the PPK-corrected imagery (local base, 1-second sampling rate) were processed first without any GCPs, and then

with all twenty-five GCPs. The vertical RMSEs were 15.66 m for autonomous only, 0.87 cm when adding GCPs to the autonomous dataset, 8.85 cm for PPK-corrected only using the local base at 1s, and 1.02 cm when adding GCPs to the PPK-corrected imagery. These results showed the significant extent to which GNSS correction techniques improve results compared to the autonomous mode. In addition, they verified the information described in the literature review about indirect georeferencing providing far better results than direct georeferencing. Table 26 summarizes the influence of using GCPs to aid with georeferencing of imagery on autonomous and PPK-corrected UAS data. Observe that the vertical RMSE decreased by 15.65 m after adding GCPs to the autonomous dataset, and 7.83 cm after adding GCPs to PPK corrected imagery. This is a testament to the efficiency of GCPs in improving the accuracies of surveys.

Table 26. Difference in vertical RMSEs for autonomous and PPK-corrected imagery (WingtraOne UAS imagery at 120 m AGL) before and after adding GCPs for georeferencing.

RMSEs from Pix4D processing report, relative to total station checkpoints.

Method	RMSE (cm)
Autonomous	1566.09
Autonomous + GCP	0.87
PPK (local base 1s)	8.85
PPK (local base 1s) + GCP	1.02

4.1.6. Summary of Results (GNSS Techniques)

This section used data from Mustang Island State Park to evaluate the impact that different GNSS techniques would have on vertical accuracies of UAS-generated products. As outlined in the preceding sections, imagery from a WingtraOne UAS was used to conduct PPK, PPP, and autonomous tests. Imagery from a Phantom 4 RTK UAS was used for PPK and RTK assessments. The PPK results presented here use local base corrections at a sampling rate of 1s.

Results showed that the choice of georeferencing technique affects accuracies in different ways. When using imagery from the WingtraOne (at 75 m AGL), the RMSEs yielded were 9.51 m (autonomous), 5.29 cm (PPK), and 32.86 cm (PPP). In contrast, WingtraOne imagery acquired at 120 m AGL yielded RMSEs of 15.66 m (autonomous), 8.85 cm (PPK), and 90.80 cm (PPP). The discrepancy between corrected and uncorrected GNSS is consistent with studies such as González-García et al. (2020) that observed as much as a 98% reduction in positional errors after implementing RTK corrections. Figure 46 summarizes the accuracy results achieved with the various techniques.

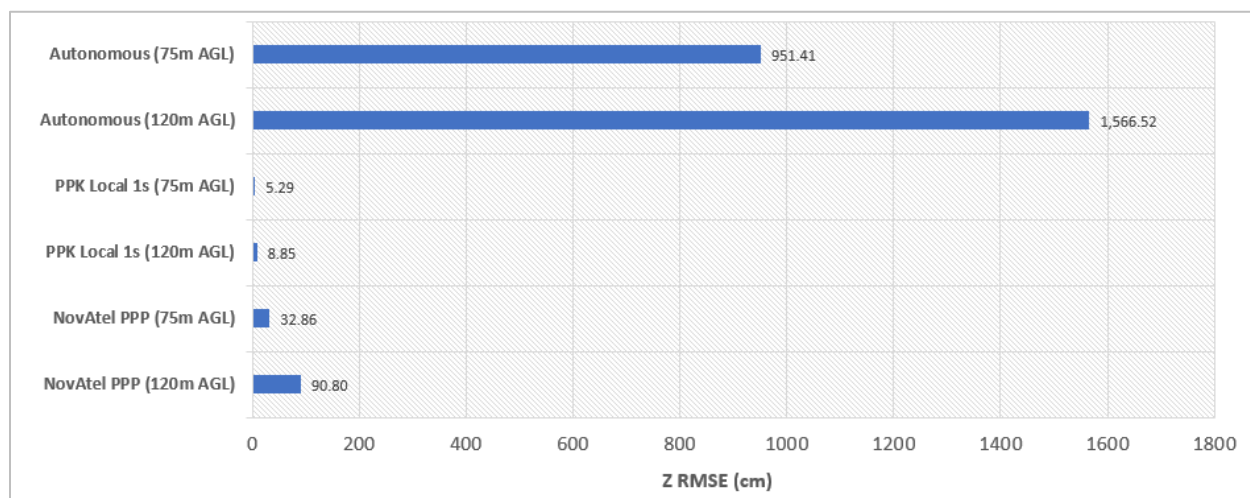


Figure 46. Accuracy comparison of autonomous, PPK, and PPP GNSS techniques using WingtraOne UAS imagery (75 m and 120 m AGL). RMSEs from Pix4D processing report, relative to total station checkpoints.

Results also showed minor differences between the RTK and PPK techniques using DJI Phantom 4 RTK imagery. Both the PPK and RTK alternatives provided vertical accuracies at the centimeter level, thus suggesting that they are suitable for survey-grade work. Figure 48 summarizes the acquired RMSEs of 8.44 cm (PPK) and 7.27 cm (RTK).

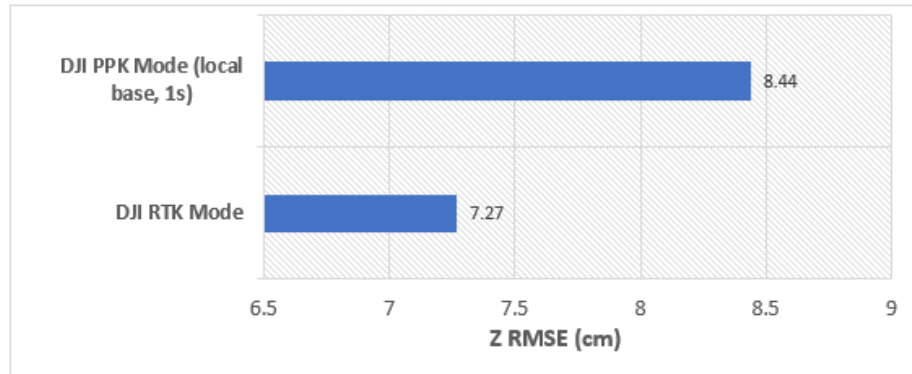


Figure 47. Comparison of PPK vs RTK accuracies using DJI Phantom 4 RTK imagery (59 m AGL). RMSEs obtained from Pix4D processing report, relative to total station checkpoints.

4.2. SfM Processing Software

This section evaluates the quantitate and qualitative impact of different SfM processing software on UAS-SfM.

Results from SfM processing software are presented according to the survey site. The next subsections will show that the SfM software used to process UAS imagery has a greater impact on the accuracy of a model than it does on the overall appearance of DSMs, DTMs, and orthomosaics.

4.2.1. Results Using Dataset from North Packery Channel (September 04, 2020)

Results from North Packery Channel yielded the highest accuracies when using Metashape and Pix4D. Overall, performances were influenced by both the software and the assessment measure used (processing report versus LAStools).

The processing reports yielded RMSEs of 6.13 cm (Pix4D), 6.49 cm (Metashape), and 11.59 cm (Drone2Map). LAStools yielded RMSEs of 6.54 cm (Metashape), 7.29 cm (Pix4D), 10 cm (ODM), and 10.96 cm (Drone2Map). These results are summarized in Table 27 and Figure 48. Since the test version of ODM does not have a concept of checkpoints, no RMSEs from the processing report are presented. All results from North Packery Channel use checkpoints relative to RTK GNSS, as no total station was used for data acquisition.

Table 27. Difference in vertical accuracies for North Packery Channel dataset (WingtraOne UAS, 100 m AGL, RMSEs relative to RTK GNSS checkpoints).

	RMSE (cm) Processing Report	RMSE (cm) LAStools
Drone2Map	11.59	10.96
Metashape	6.49	6.54
ODM	N/A	10.00
Pix4D	6.13	7.29

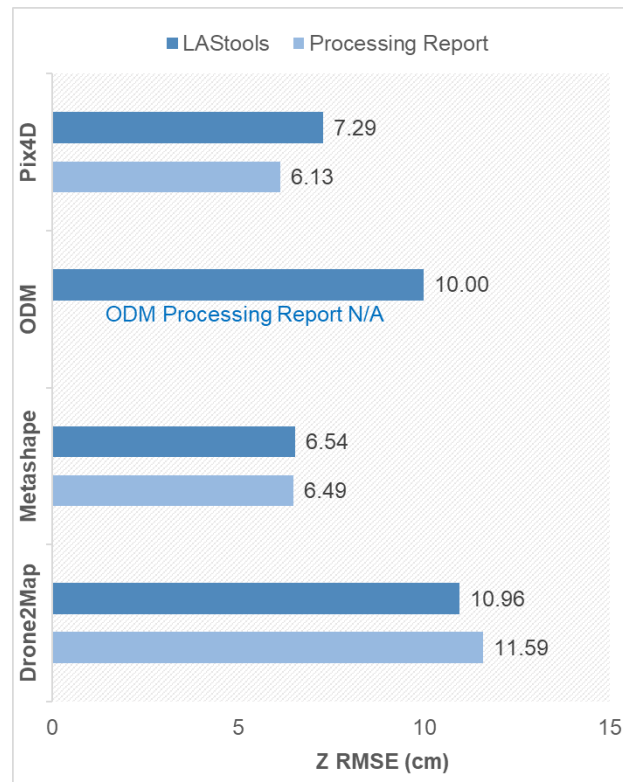


Figure 48. Vertical RMSEs for different SfM software for North Packery Channel dataset (WingtraOne UAS, 100 m AGL, RMSEs relative to RTK GNSS checkpoints).

The software used also impacts the quality of generated UAS-SfM products, as observed in Figure 49. As the figure shows, the edges of the mapped areas are much less smooth with Metashape than the remaining software. This happens because, unlike the others, Metashape does not smooth out the edges of the mapped area. Refer to the appendices for examples of DTMs, orthomosaics, and point clouds.

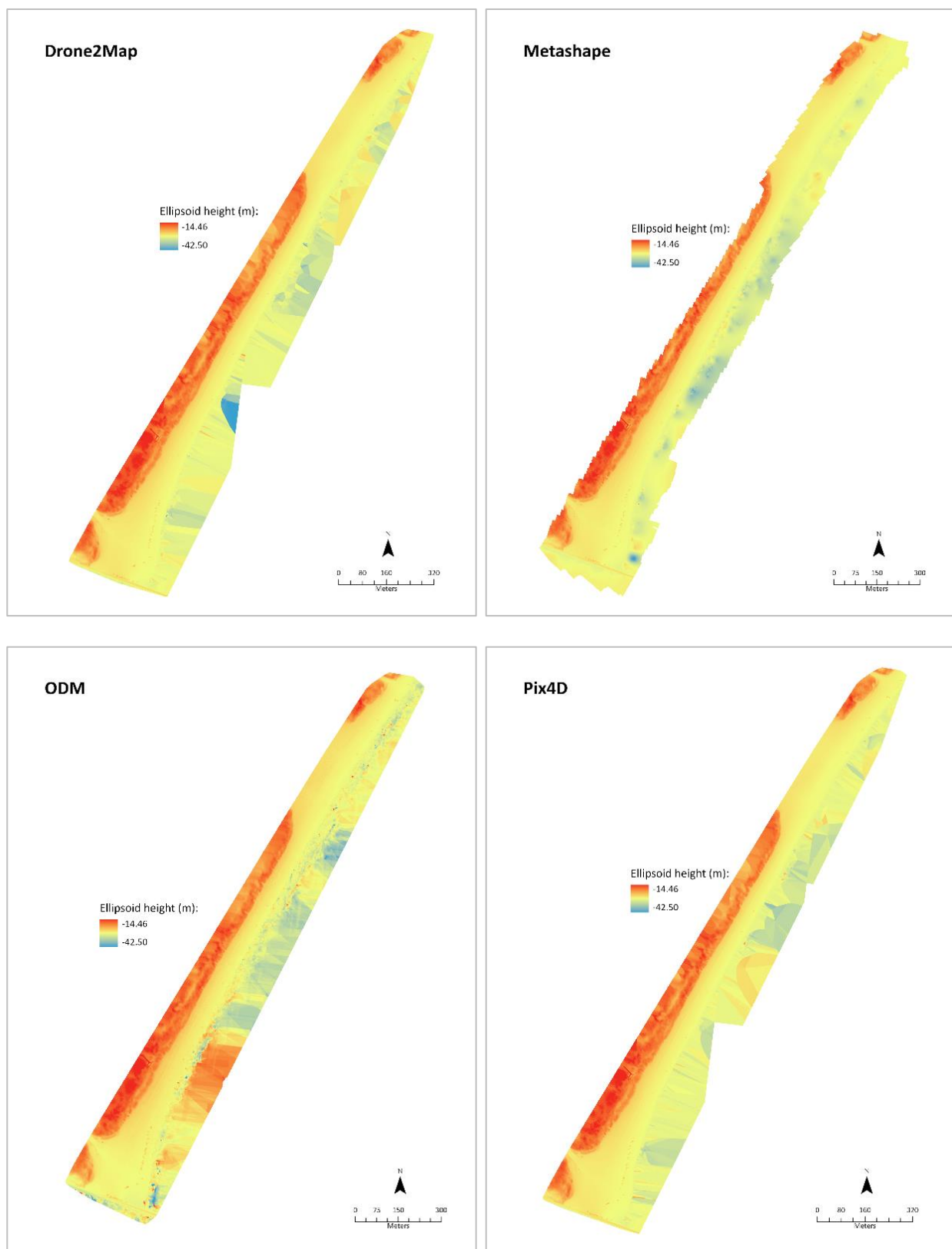


Figure 49. Resulting DSMs for North Packery Channel (WingtraOne UAS, 100 m AGL).

The ability to mask unwanted or noisy features within Metashape was also of interest to this study. When using masks during UAS-SfM data processing, noisy points are ignored and subsequently disregarded when generating the resulting products. Tests showed that masks are powerful in excluding noise from final products, especially when mapping areas that encompass non-static features (i.e., water and vegetation). Masking has also proved to impact vertical accuracies (6.49 cm without masking, 6.40 cm after masking). Figure 50 shows the difference between the unmasked and masked DSMs. Observe that the masked DSM is cleaner than the unmasked DSM. Figure 51 shows the Metashape interface before and after masking.

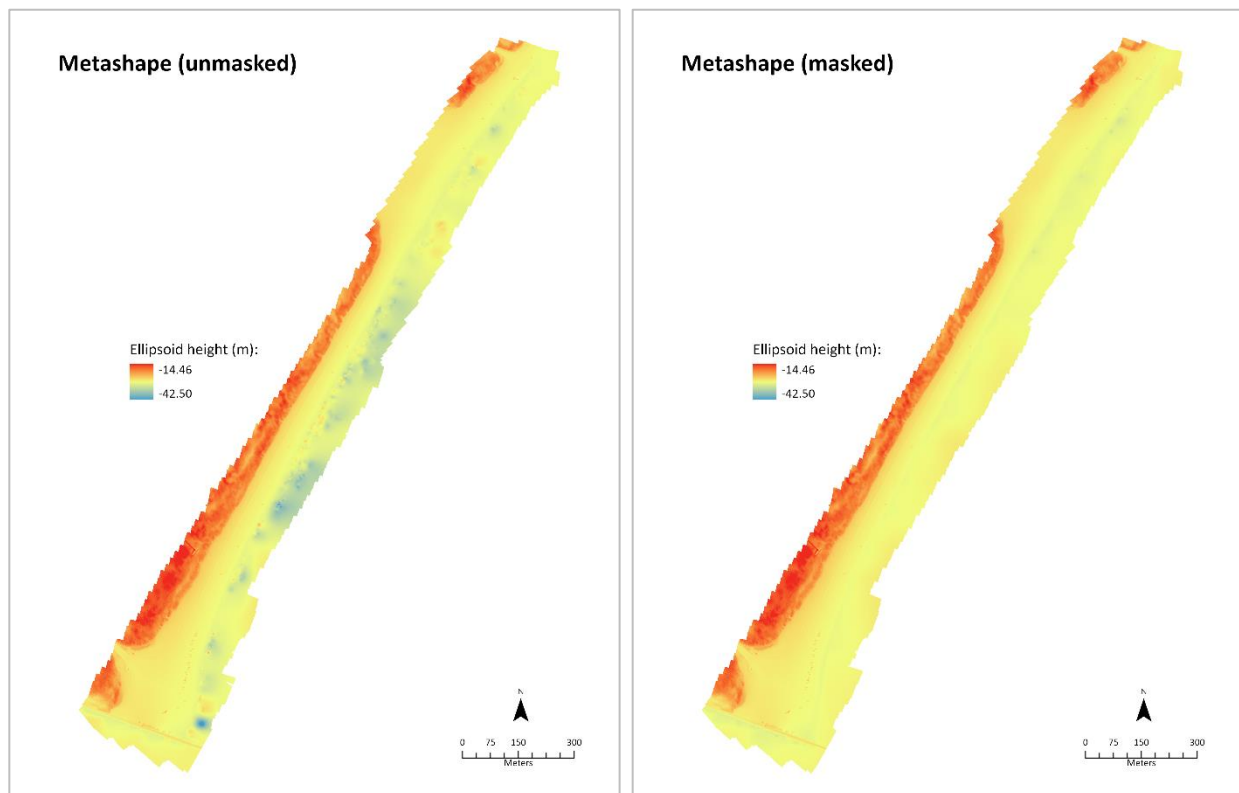


Figure 50. Unmasked vs masked DSMs for North Packery Channel (WingtraOne UAS, 100 m AGL, RMSEs relative to RTK GNSS checkpoints).

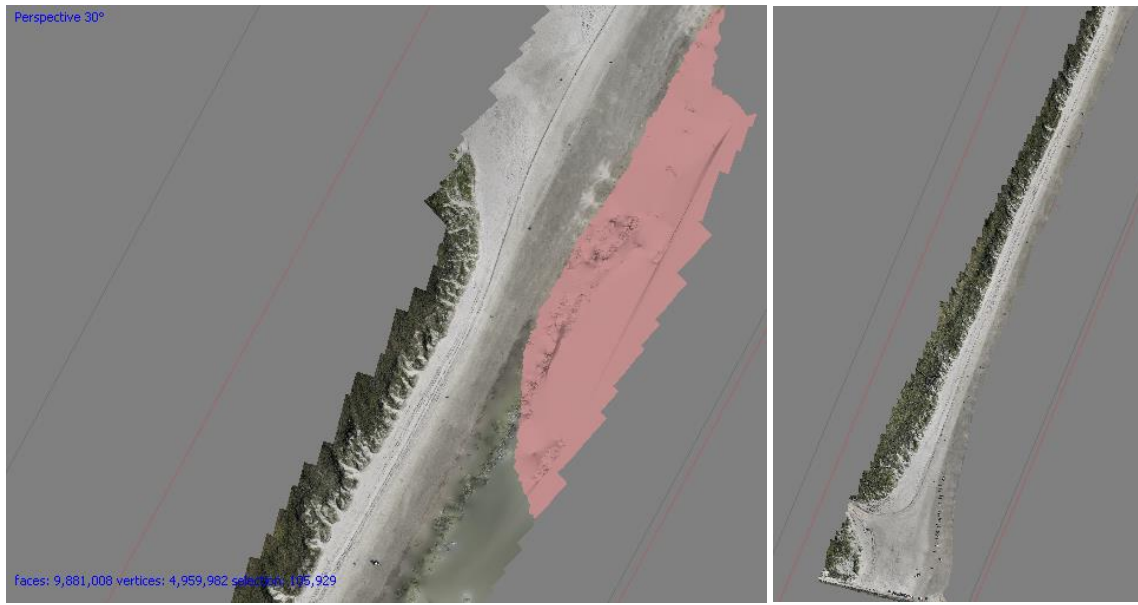


Figure 51. Screen capture of Metashape interface showing the point cloud before masking (left) and after masking (right) of water features at North Packery Channel.

4.2.2. Results Using Dataset from Mustang Island State Park (July 13, 2021)

Mustang Island State Park results also yielded the lowest RMSEs when using Metashape and Pix4D. All processing for this dataset used imagery from the WingtraOne UAS flight at 75 m AGL and checkpoints relative to the total station. The vertical RMSEs from processing reports were 5.29 cm (Pix4D), 6.55 cm (Metashape), and 12.63 cm (Drone2Map). On the other hand, the vertical RMSEs from LAStools were 6.74 cm (Pix4D), 6.77 (Metashape), 13.67 cm (Drone2Map), and 1.45 m (or 145.69 cm for ODM). These results are summarized in Table 28.

Table 28. Difference in vertical accuracies for Mustang Island State Park (WingtraOne UAS, 75 m AGL, RMSEs relative to total station checkpoints).

	RMSE (cm) Processing Report	RMSE (cm) LAStools
Drone2Map	12.63	13.67
Metashape	6.55	6.77
ODM	N/A	145.69
Pix4D	5.29	6.74

The most unexpected performance from Mustang Island State Park was the vertical RMSE reported in ODM (1.45 m), which differed significantly from results using the North Packery Channel dataset. Several processing runs were conducted to examine potential reasons behind this issue, including processing the same set of imagery in Pix4D (yielding an RMSE of 5.17 cm). Given the much lower RMSE in Pix4D with the same dataset, including photos with the coordinates embedded in the imagery EXIFs, it was determined that this was not due to a blunder or human error. At this time, the hypothesis is that ODM is having an issue with the data itself. Further investigation is needed to better understand these inconsistencies. For comparative purposes, GCPs were used for ODM alone, to evaluate its performance if GCPs were to be used. Figure 52 summarizes the RMSEs for all software, including ODM with and without GCPs.

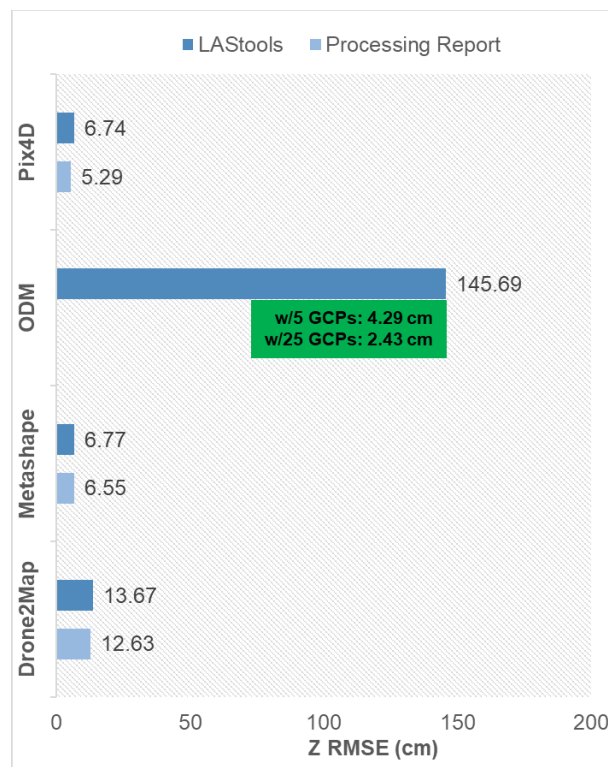


Figure 52. Processing results for different SfM software using data from Mustang Island State Park (WingtraOne UAS, 75 m AGL, RMSEs relative to total station checkpoints, although there are two examples of using GCPs for ODM).

The resulting products were also very similar between all four SfM software. Figure 53 shows the similarities between the DSMs. Once again, Metashape generated products with a slightly different shape than its counterparts.

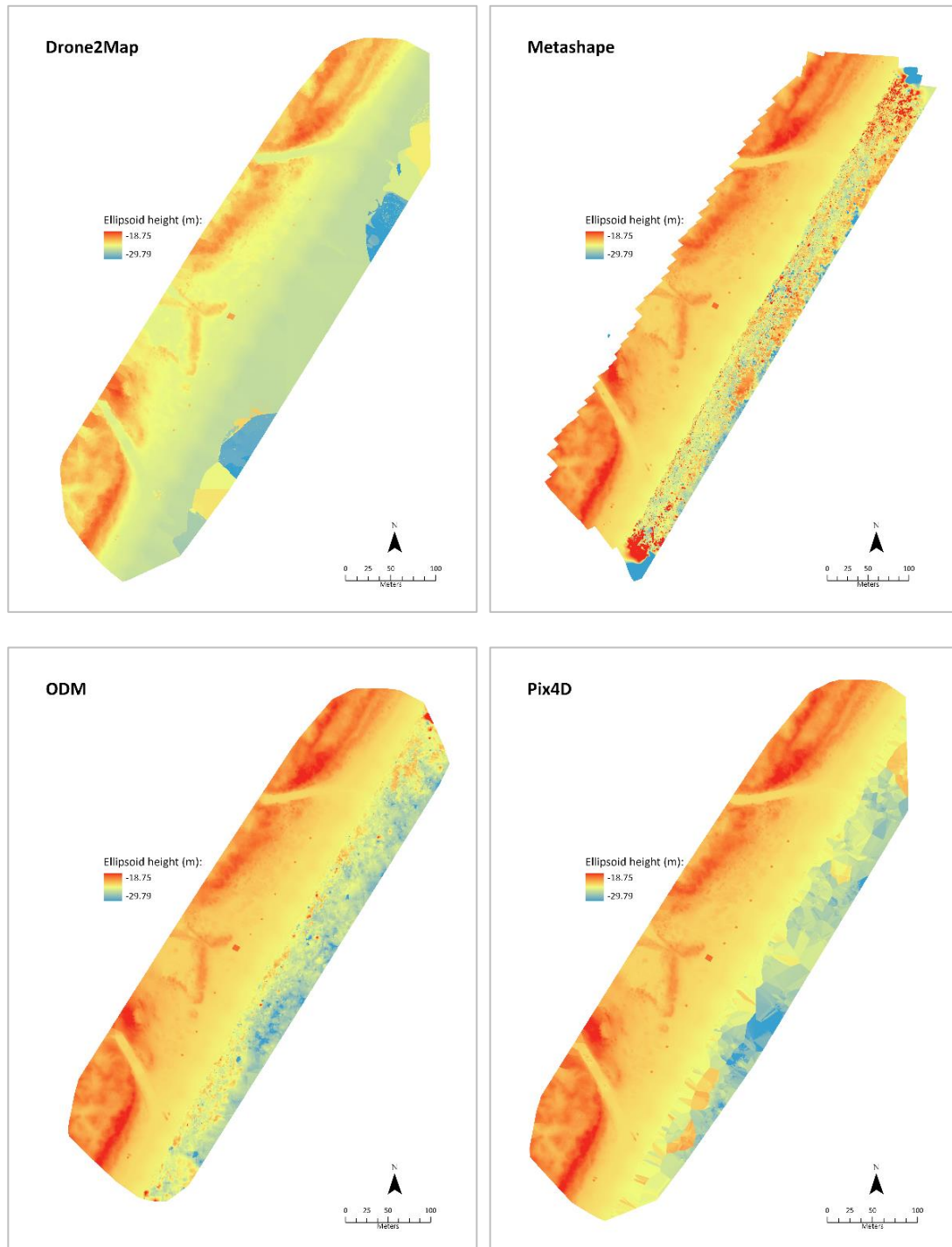


Figure 53. Resulting DSMs from Mustang Island State Park (WingtraOne UAS, 75 m AGL).

4.2.3. Summary of Results (SfM Software Comparison)

As observed in the preceding sections, Metashape and Pix4D were the best performing of the software tested, having achieved centimeter-level accuracy. Drone2Map consistently yielded vertical RMSEs below 14 cm, and ODM led to surprising results as it performed well with the North Packery Channel dataset, yet poorly with the Mustang Island State Park dataset.

Drone2Map and ODM were of significant interest for this study, because of the former's compatibility with ArcGIS, and the latter's feasibility. Some of the advantages of Drone2Map include fast rendering in ArcGIS Pro, creation of project files that can be accessed and processed in Pix4D, ease of area and volumetric measurements, and the ability to export features for ArcGIS online use. Some of the disadvantages of Drone2Map are abrupt closures, common freezing during tagging of ground control, known issues when using non-WGS84 reference systems, and a slightly longer processing time. Other advantages and disadvantages of Drone2Map as shown in Table 29 below, in its comparison with Pix4D.

Table 29. Comparison between Drone2Map and Pix4D.

	DRONE2MAP	PIX4D
Advantages	<ul style="list-style-type: none"> • Bulk disabling of uncalibrated images • Creates project files accessible through Pix4D • Faster rendering in ArcGIS Pro • User-friendly interface • Good support from ESRI • Able to open projects in ArcGIS • Easy integration with ArcGIS online • Retains property of control export • Easy to make area/volume measurements • Control marks exported as .zip, less prone to unintentional alterations 	<ul style="list-style-type: none"> • Easier tagging of ground control • Shows GCP residuals during tagging • GCP marks export similar to other SfM software (excluding Drone2Map) • Has shortcut for DSM and DTM generation • Works well with EXIF and CSVs • Lower vertical RMSEs • Shows orientation accuracy of input imagery • Faster rendering of point cloud
Disadvantages	<ul style="list-style-type: none"> • Abrupt closures • Common freezing during GCP tagging • Often requires internet access • Does not show orientation accuracy of input imagery • Does not show GCP residuals during tagging • Known issues with non-WGS84 systems • Struggles with geotags in external CSV • Longer processing time • Slow rendering of 3D point cloud within software 	<ul style="list-style-type: none"> • No bulk disabling of uncalibrated images • Annotation not improving RMSEs (research ongoing) • Control export always defaults to 3D GCPs

One of the biggest advantages of ODM is that it is open-source. Other benefits include powerful visualization options through web viewing, batch processing, and the ability to add multiple processing jobs to the queue. Disadvantages of ODM include complex installation procedures, reliance on several other tools (i.e., Docker, GitHub), and issues with non-WGS84 reference systems. In addition, the time taken to process data in ODM can be very irregular, even when using the same dataset. There were times when the data was processable within 30 minutes, and when reprocessing the same dataset, it could take hours to process. At times, ODM requires the processing window to remain active or maximize for the user to see progress in processing time, otherwise, it could process for days. Table 30 compares the advantages and disadvantages of Metashape, ODM, and Pix4D, and Table 31 summarizes the strengths and weaknesses of all four SfM software examined in this study.

Table 30. Comparison between Metashape, ODM and Pix4D.

	METASHAPE	ODM	PIX4D
Advantages	<ul style="list-style-type: none"> • Bulk disabling of uncalibrated images • Easy to use batch processing • Has shortcut for rematching/reoptimizing • No supplementary software needed • Clean orthomosaics/DSMs • Shows GCP residuals • Batch processing 	<ul style="list-style-type: none"> • Open-source (WebODM) • Web viewer • Mainly batch processing • Easy to make area/volume measurements • Powerful visualization options via browser • Small size files • Allows to queue different processing jobs • Outputs products to virtual directory (can be downloaded as zip) 	<ul style="list-style-type: none"> • Easier GCP targeting • Shows GCP residuals when tagging • No supplementary software needed • Straightforward processing • Automatically outputs products to working directory
Disadvantages	<ul style="list-style-type: none"> • Repetitive workflow • Extra steps for DTM generation • Occasional lagging after mesh generation • Does not output products to working directory (must export manually) • Commercial 	<ul style="list-style-type: none"> • Outdated documentation • Irregular processing times • Fails when using external PPK CSV • Does not show GCP residuals during tagging • Does not show orientation accuracy • Complex to install • No rematching/reoptimizing shortcut • Known issues with host IP • Supplementary software needed (GIT, Linux, Docker) • Requires familiarity with programming • Struggles with point classification • Docker uses a lot of storage • Unsuitable for non-WGS84 • No built-in checkpoint accuracy calculator (must use alternative tools for calculation, such as LAStools, when not using GCPs). 	<ul style="list-style-type: none"> • No bulk disabling of uncalibrated images • No bulk disabling of uncalibrated images • Commercial

Table 31. Strengths and weaknesses of Drone2Map, Metashape, ODM, and Pix4D.

	Drone2Map	Metashape	ODM	Pix4D
<i>Automatic classification of points</i>	Yes	No	Yes	Yes
<i>Available documentation online</i>	Very good	Very good	Good	Very good
<i>Batch processing</i>	Yes	Yes	Yes	Yes
<i>Built-in masking/annotation functionality</i>	No	Yes	No	Yes
<i>Bulk disabling of uncalibrated images</i>	Yes	Yes	No	No
<i>Can create DTMs and DSMs</i>	Yes	Yes	Yes	Yes
<i>Can be used offline</i>	Yes	Yes	No	Yes
<i>Can use corrections in CSV</i>	Yes	Yes	No	Yes
<i>Category</i>	Commercial	Commercial	Open-source	Commercial
<i>Export of final products to local directory</i>	Automatic	Manual	Manual	Automatic
<i>Exports marks for future use</i>	Yes	Yes	Yes	Yes
<i>Has point cloud classifier</i>	Yes	Yes	Yes	Yes
<i>Responsiveness from forums</i>	Poor	Not used	Good	Good
<i>Shortcut for rematching/reoptimization</i>	No	Yes	No	Yes
<i>Shows residuals of marked targets</i>	No	Yes	No	Yes
<i>Works well in NAD83 (2011)</i>	No	Yes	No	Yes

CHAPTER V

SUMMARY OF LESSONS LEARNED

5.1. Lessons Learned from GNSS Evaluation

The major lessons learned from the impact of GNSS solutions on UAS-SfM vertical accuracies are summarized as follows:

- PPK and RTK GNSS solutions without the aiding of GCPs can achieve vertical accuracies that consistently meet and exceed the objectives of this study. Vertical accuracies of 0.5 meter at the 95% confidence level are required, and these techniques showed to fulfil such requirement.
- RTK corrections of UAS image geolocations can achieve centimeter-level vertical accuracy based on the computed RMSEs relative to high accuracy control points. However, RTK performance is affected by the coverage area of the RTN (i.e., TxDOT RTN) used for data collection as well as availability of the cellular network at the time of the survey. Because RTN coverage is limited along coastlines, it is important to ensure that the UAS operates within close range of the base station transmitter to receive real-time corrections.
- PPK corrections on image geolocations can also achieve vertical accuracies at the centimeter level based on the computed RMSEs relative to high accuracy control points. Performance is affected by factors such as the distance between base station and the survey site, the percentage of images that undergo PPK fix, and the quantity and quality of GNSS observations acquired at a given sampling rate. Also, the accuracy of PPK can potentially suffer when setting up a local base station on non-stable environments such as sandy beach surfaces.

- Remote station distance, PPK fix percentage and sampling rate:
 - Overall, vertical RMSEs increase as the baseline distance of the GNSS reference station increases. Results from this study recommend using a base station within 30 km of the survey region for PPK processing. When deploying a local base station on unstable surfaces such as sandy beach sediments, a stabilized nearby CORS station may be a more viable alternative, if available, leading to a better PPK solution as demonstrated in this study.
 - In terms of accuracy impact, the PPK fix percentage reported by the respective PPK processing software is an important metric to consider in addition to baseline distance. On several occasions, remote stations located closer to the survey area with a lower PPK fix percentage yielded higher RMSEs than those farther away with a higher fix percentage.
 - Estimating the influence of GNSS baseline distance on PPK accuracies can be an unfair comparison if not considering contributing factors such as potential multipath or receiver specific noise, signal obstruction, antenna quality, and weather conditions at where the base stations are located.
 - When evaluating the influence of GNSS base station sampling rate on the accuracy of PPK solutions, there was no consistent pattern favoring one sampling rate over another. While higher frequencies (e.g., 1 Hz) are typically favored, they can be prone to capturing more signal noise if present, which can negatively affect data accuracy. Results observed in this study are similar to those reported in other studies. When ground control is available for accuracy

validation, a best practice is to evaluate multiple PPK solutions at different sampling rates and select the one providing the best vertical RMSE.

- PPK does not require maintaining a real-time connection during flight to receive broadcast corrections. Although RTK is efficient, if the signal coverage is lost during flight, those geolocation corrections cannot be retrieved, which degrades the quality of SfM processing solutions.
- Kinematic PPP solutions can reach at least decimeter-level vertical accuracy based on the computed RMSEs relative to high accuracy control points. PPP accuracy results obtained in this study did not meet the NOAA OCS requirement of a 0.5 m level vertical uncertainty at the 95% confidence level, and the results showed significant differences in vertical RMSE between the 75 m AGL and 120 m AGL WingtraOne UAS flights at Mustang Island State Park. Several factors can contribute to the quality of a PPP solution, including atmospheric conditions at the time of flight, satellite geometry, and the observation time of the rover GNSS.
- While open-source alternatives do exist for Kinematic PPP processing, such as CSRS-PPP and RTKLIB, there is currently limited information about the use of such services for application to UAS technology. This happens mainly because these alternatives were primarily developed for static purposes and adjusted to allow kinematic processing. In addition, they often do not offer synchronization between the timestamps of image capture and processing time as obtained from the tool or software.
- This study used NovAtel Inertial Explorer as a straightforward Kinematic PPP alternative. Although commercial, it can synchronize the timestamps from the UAS platform and the time information from the geolocation processing results to correctly

apply image corrections. It also provides various useful plots for evaluating the quality of a PPP processing result. Before processing in SfM software, each row of a PPK solution needs to be matched to the respective image they represent. The camera events used for time synchronization only show when those events happened, but they do not generate geotags that are tied to the image names, which is needed for processing in software like Pix4D and Drone2Map. This is a straightforward process as the order in which the solutions are given matches the order that the photos were taken; except they are not matched as they are in RTK or PPK processing.

- Further test is recommended to determine the optimal workflow for applying PPP to UAS-SfM surveys for surveying shorelines and remote areas. One test to consider is whether recording static GNSS observations on the UAS for extended periods before flight will improve the PPP solution.
- Autonomous GNSS flights reached vertical RMSEs as high as 15 meters in this study. Based on these results, uncorrected GNSS solutions for UAS-SfM are not a viable alternative for NOAA OCS surveying purposes.
- RTK GNSS versus total station surveyed ground control:
 - When comparing differences in UAS-SfM vertical accuracies, lower standard deviations of error were observed with the total station surveyed checkpoints. This suggests that the total station survey control provides higher precision and more consistency point-to-point relative to RTK GNSS.
 - Although the total station control may offer higher precision, its absolute georeferencing is only as accurate as the instrument points it uses as a reference. Because this study used RTK GNSS to establish the instrument points, the total

station coordinates are also influenced by the accuracy of the RTK at the time the temporary points were established.

- Differences in accuracies observed between total station and RTK GNSS control in this study were minimal. Although one may gain more precision with a total station, RTK is a more practical solution for validating UAS-SfM accuracies in most cases. This is especially true when performing UAS surveys over dynamic sandy beaches in coastal zone where sediment flux is constantly changing, and differences of a few centimeters in elevation are acceptable.

5.2. Lessons Learned from SfM Software Evaluation

- Both case studies showed that Metashape and Pix4D produced the lowest vertical RMSEs, thus suggesting that they are the most robust of all alternatives explored. Based on PPK only solutions and no GCP adding, both software continuously yielded vertical accuracies at the centimeter level.
- Drone2Map and ODM failed to achieve similar vertical accuracies to Metashape and Pix4D. Drone2Map consistently yielded RMSEs within the 10-15 cm range. ODM was able to reach approximately 10 cm RMSE with the North Packery Channel dataset while reaching errors greater than 1 m with the Mustang Island State Park dataset. Subsequent use of GCPs within ODM resulting in that error dropping down to centimeter-level vertical accuracy.
- The choice of software also influences the qualitative appearance of the derivative mapping products generated from the imagery and point cloud data, including DSMs, DTMs, and orthomosaics. These differences ranged from subtle differences to more substantial, such as when comparing Metashape to the other software tested. Choice in

resolution, interpolation function, smoothing, color blending, and other parameter settings can influence the appearance of derivative mapping products.

- Tested versions of Drone2Map and ODM evaluated in this study do not properly support non-WGS84 coordinate systems when using checkpoints. Checkpoints needed to be converted from NAD83(2011) Texas South to WGS84 UTM Zone 14N to enable more accurate results for comparison to Pix4D and Metashape results.
- ODM has no concept of checkpoints within the software interface as the software currently supports GCPs only. To evaluate the accuracy of models, the data was first processed without any ground control, and then the *LAScontrol* module of LAStools used to obtain accuracy results based on the exported dense cloud.
- Drone2Map, Metashape, and Pix4D can take coordinate information in either an external file or embedded into the imagery EXIF. ODM processing repetitively failed when using external geotag files. Drone2Map may experience shifting of some of the input images to the Prime Meridian when using geotags from an external CSV file. In addition, slightly lower RMSEs were observed when using geotags embedded into the imagery EXIF. Although, this may be within random numerical variability.
- RMSE values reported in the processing reports are based on how well the SfM bundle adjustment solution fits to the tagged checkpoints within the software. In contrast, the LAStools approach provides a direct measure of the vertical accuracy of the exported dense point cloud. Accuracy results based on both methods were very consistent and generally within a centimeter difference. Results show that the RMSEs based on checkpoint comparisons in the processing report are also a good indicator of the positional accuracy of the densified point cloud. However, caution must be taken

because reconstruction accuracy can vary by image texture. Distinct features (i.e., aerial control targets) may not be representative of point cloud fidelity in other regions of the reconstructed scene.

- When using checkpoints for evaluation of UAS-SfM accuracy, the number and distribution of checkpoints throughout the scene is a key factor to consider. The reader is recommended to refer to the ASPRS (2015) for more guidance. As an example, a minimum of 20 checkpoints distributed throughout the scene is a recommendation.
- Some software applications filter out noisy features or keypoints automatically with little or no user input. This is the approach that Pix4D uses. The advantage of this method is that users do not need to worry about the internal workings of the SfM software, enabling a more efficient, easier processing workflow. The disadvantage is having to depend on the capability of the software to filter out noisy point features automatically and accurately, which can vary for different environments. Alternatively, some software allows the user to filter out the points based on a set of accuracy metrics. This feature enables the user to tune the feature matching and removal of spurious points based on the terrain being mapped. Agisoft Metashape uses this approach. Whichever software suite is used for SfM processing, it is necessary to follow proper software guidelines and select proper processing settings.

CHAPTER VI

CONCLUSION AND FUTURE WORK

6.1. Conclusion

As part of an investigation conducted by the Office of Coast Survey at the NOAA, this project sought to identify post-processing GNSS solutions for kinematic surveying without using GCPs. While GCPs provide very accurate results, they are unsuitable for surveying remote areas, particularly with regard to UAS deployment from ships. A series of surveys were conducted at North Packery Channel and Mustang Island State Park to evaluate the feasibility of various GNSS techniques and SfM processing software. Results showed that the choice of GNSS technique and SfM software can have a significant impact on the quality of UAS-generated products.

In terms of PPK and RTK led to the lowest vertical RMSEs, followed by PPP and then autonomous flights. PPK and RTK were able to achieve centimeter-level vertical accuracies and satisfy the objectives of this study of reaching RMSEs no greater than 50 cm when multiplying the RMSE by a factor of 1.96, so they can be utilized as alternatives to GCPs for surveying remote areas. Kinematic PPP reached decimeter-level accuracies, with the promise to perform even better with improved convergence. Autonomous GNSS led to several meters of error and is unsuitable for survey-grade applications. Both PPP and autonomous failed to satisfy the goals of this study.

When using remote base stations for PPK processing, the best results were achieved with stations located within 30 km of the survey site. Although no clear relationship was observed between sampling rate and accuracy, tests showed that better accuracies are achievable with higher PPK fix percentages. The study also showed that the method used to survey ground control can also influence accuracies. While RTK surveyed control yielded lower RMSEs, total station measurements were more consistent and suggest greater local accuracy between the targets.

Moreover, Drone2Map, Metashape, and Pix4D were the most consistent processing software options. Metashape and Pix4D led to the highest accuracies and reached centimeter-level vertical accuracies. Inconsistencies found with tested versions of Drone2Map and ODM included substantially higher RMSEs when using non-WGS84 coordinate systems with no GCPs, which fails to meet the requirements of this project since no use of GCPs is intended.

The solutions herein explored also drastically reduce the amount of time taken for SfM data acquisition and processing. Eliminating reliance on GCPs means that no time is invested into distributing GCPs across the survey area and taking measurements on them, thus no time is needed to mark them during post-processing, thus expediting the process of UAS surveying. The highest accuracies are reached with the right combination of RTK or PPK and Pix4D or Metashape. The results discussed in this study are limited to the survey site and equipment used.

6.2. Recommendations

This study has been of extreme significance to the author as it helped to understand ways to optimize UAS data acquisition and processing for mapping shorelines and remote areas. The challenges encountered during this study help to make a few recommendations in terms of both GNSS solutions and SfM processing software.

First, it is recommended to fly at lower altitudes and utilize PPK or RTK corrections. If using different UAS platforms for comparison purposes, it is recommended to adjust the flight heights to ensure that similar GSDs are obtainable with the various platforms. Second, it is recommended to use base stations located as close to the survey site as possible. The closer the better. While local base stations are favored, unstable land use (i.e., beaches) can lead to relatively higher RMSEs. Therefore, when occupying said environments, the use of remote base stations should be considered. Third, the percentage of PPK fixes is very important. When deciding the

sampling rate to use, consider using the rate that yields the highest fix percentage, which may not always be the highest sampling rate.

As for the processing software, the recommendation is to use Metashape or Pix4D, primarily because they can generate the lowest RMSEs and are compatible with non-WGS84 coordinate systems such as NAD83 (2011) Texas South. When attempting to produce DSMs and DTMs that are as free of noise as possible, Metashape is potentially a better alternative as it allows for the masking of non-static features such as water and vegetation. However, in doing so, it is recommended to generate the orthomosaics before masking because it helps to better visualize the survey area. Lastly, Drone2Map proved to be a powerful tool for online visualization, therefore it should be considered when planning projects that are intended to generate products that will be used online.

6.3. Future work

Future work consists of further exploring the applicability of Kinematic PPP for UAS surveys. Given that past studies have reached centimeter-level accuracies in the past, under slightly different workflows, it is of great interest to explore the impact that allowing longer convergence times can have on PPP accuracies. It is probable that allowing the UAS platform to stand static for some time before deployment might improve results.

Also, given the logistical ease that ODM can provide, it would be beneficial to explore and solve the challenges with its inconsistencies. Brief correspondence with developers showed that there is potential to collaborate on creating a more stable software that supports non-WGS84 reference systems when not using GCPs. Finally, changes within ESRI's Drone2Map are expected within one year of this writing. Future work could also evaluate how the upcoming algorithm performs in comparison with the one tested in this study.

REFERENCES

- AEROTAS. (2018, November). *Phantom 4 RTK PPK Processing Workflow*. AEROTAS, 3 303 Habor Blvd., St E B4 , Costa Mesa, California.
- Alkan, R. M., Erol, S., Ozulu, I. M., & Ilci, V. (2020, January). Accuracy Comparison of Post-Processed PPP and Real-Time Absolute Positioning Techniques. *Geomatics, Natural Hazards and Risk*, 11, 178-190. doi:10.1080/19475705.2020.1714752
- Alkan, R. M., Saka, M. H., Ozulu, I. M., & İlçi, V. (2017, October). Kinematic Precise Point Positioning Using GPS and GLONASS Measurements in Marine Environments. *Measurement*, 109, 36–43. doi:10.1016/j.measurement.2017.05.054
- Angrisano, A., Dardanelli, G., Innac, A., Pisciotta, A., Pipitone, C., & Gaglione, S. (2020, August). Performance Assessment of PPP Surveys with Open Source Software Using the GNSS GPS–GLONASS–Galileo Constellations. *Applied Sciences*, 10, 5420. doi:10.3390/app10165420
- ASPRS. (2015, March). ASPRS Positional Accuracy Standards for Digital Geospatial Data. *Photogrammetric Engineering & Remote Sensing*, 81, 1–26. doi:10.14358/pers.81.3.a1-a26
- Bandini, F., Sunding, T. P., Linde, J., Smith, O., Jensen, I. K., Köppl, C. J., . . . Bauer-Gottwein, P. (2020, February). Unmanned Aerial System UAS Observations of Water Surface Elevation in a Small Stream: Comparison of Radar Altimetry, LIDAR and Photogrammetry Techniques. *Remote Sensing of Environment*, 237, 111487. doi:10.1016/j.rse.2019.111487
- Berber, M., Munjy, R., & Lopez, J. (2021, January). Kinematic GNSS Positioning Results Compared Against Agisoft Metashape and Pix4dmapper Results Produced in the San

- Joaquin Experimental Range in Fresno County, California. *Journal of Geodetic Science*, 11, 48-57. doi:10.1515/jogs-2020-0122
- Bisnath, S., Wells, D., Santos, M., & Cove, K. (2004). Initial Results from a Long Baseline, Kinematic, Differential GPS Carrier Phase Experiment in a Marine Environment. *PLANS 2004. Position Location and Navigation Symposium IEEE Cat. No.04CH37556*). IEEE. doi:10.1109/plans.2004.1309052
- Chen, C., & Chang, G. (2020, November). PPPLib: An Open-Source Software for Precise Point Positioning Using GPS, BeiDou, Galileo, GLONASS, and QZSS with Multi-Frequency Observations. *GPS Solutions*, 25. doi:10.1007/s10291-020-01052-4
- Choy, S., & Harima, K. (2020, August). Design of a Compact, Multifrequency, Multiconstellation GNSS Precise Point Positioning Correction Format. *IEEE Transactions on Aerospace and Electronic Systems*, 56, 2990-2998. doi:10.1109/taes.2019.2958189
- Chu, T., Starek, M. J., Berryhill, J., Quiroga, C., & Pashaei, M. (2021, July). Simulation and Characterization of Wind Impacts on sUAS Flight Performance for Crash Scene Reconstruction. *Drones*, 5, 67. doi:10.3390/drones5030067
- Daakir, M., Pierrot-Deseilligny, M., Bosser, P., Pichard, F., Thom, C., Rabot, Y., & Martin, O. (2017, May). Lightweight UAV with On-Board Photogrammetry and Single-Frequency GPS Positioning for Metrology Applications. *ISPRS Journal of Photogrammetry and Remote Sensing*, 127, 115-126. doi:10.1016/j.isprsjprs.2016.12.007
- DJI. (2021). *Phantom 4 RTK User Manual*.

- Duo, E., Fabbri, S., Grottoli, E., & Ciavola, P. (2021, May). Uncertainty of Drone-Derived DEMS and Significance of Detected Morphodynamics in Artificially Scraped Dunes. *Remote Sensing*, 13, 1823. doi:10.3390/rs13091823
- Erol, S., Alkan, R. M., Ozulu, Í. M., & İlçi, V. (2020, November). Impact of Different Sampling Rates on Precise Point Positioning Performance Using Online Processing Service. *Geospatial Information Science*, 24, 302–312. doi:10.1080/10095020.2020.1842811
- ESRI. (n.d.). ArcGIS Drone2Map Help. *ArcGIS Drone2Map Help*. Retrieved from <https://doc.arcgis.com/en/drone2map/get-started/system-requirements.htm>
- Estey, L., & Wier, S. (2014, June). *TEQC Tutorial - Basics of TEQC Use and TEQC Products*.
- Forlani, G., Dall'Asta, E., Diotri, F., di Cella, U. M., Roncella, R., & Santise, M. (2018, February). Quality Assessment of DSMs Produced from UAV Flights Georeferenced with On-Board RTK Positioning. *Remote Sensing*, 10, 311. doi:10.3390/rs10020311
- Fraser, C. S. (2013, April). Automatic Camera Calibration in Close Range Photogrammetry. *Photogrammetric Engineering & Remote Sensing*, 79, 381–388. doi:10.14358/pers.79.4.381
- Ghilani, C. D. (2017, January 24). *Elementary Surveying*. Pearson Education (US).
- Gonçalves, G., Andriolo, U., Pinto, L., & Bessa, F. (2020, March). Mapping Marine Litter Using UAS on a Beach-Dune System: A Multidisciplinary Approach. *Science of The Total Environment*, 706, 135742. doi:10.1016/j.scitotenv.2019.135742
- González-García, J., Swenson, R. L., & Gómez-Espinosa, A. (2020, October). Real-Time Kinematics Applied at Unmanned Aerial Vehicles Positioning for Orthophotography in Precision Agriculture. *Computers and Electronics in Agriculture*, 177, 105695. doi:10.1016/j.compag.2020.105695

- Halls, J. N., & Magolan, J. L. (2019, September). A Methodology to Assess Land Use Development, Flooding, and Wetland Change as Indicators of Coastal Vulnerability. *Remote Sensing*, *11*, 2260. doi:10.3390/rs11192260
- Hastaoğlu, K. Ö., Gül, Y., Poyraz, F., & Kara, B. C. (2019, November). Monitoring 3D Areal Displacements By a New Methodology and Software Using UAV Photogrammetry. *International Journal of Applied Earth Observation and Geoinformation*, *83*, 101916. doi:10.1016/j.jag.2019.101916
- Henkel, P., Iafrancesco, M., & Sperl, A. (2016). Precise Point Positioning with Multipath Estimation. *2016 IEEE/ION Position, Location and Navigation Symposium (PLANS)*, (pp. 144-149). doi:10.1109/PLANS.2016.7479694
- James, M. R., Robson, S., d'Oleire-Oltmanns, S., & Niethammer, U. (2017, March). Optimising UAV Topographic Surveys Processed with Structure-from-Motion: Ground Control Quality, Quantity and Bundle Adjustment. *Geomorphology*, *280*, 51-66. doi:10.1016/j.geomorph.2016.11.021
- Jamieson, M., & Gillins, D. T. (2018, November). Comparative Analysis of Online Static GNSS Postprocessing Services. *Journal of Surveying Engineering*, *144*, 05018002. doi:10.1061/(asce)su.1943-5428.0000256
- Kalacska, M., Arroyo-Mora, J. P., & Lucanus, O. (2021, May). Comparing UAS LiDAR and Structure-from-Motion Photogrammetry for Peatland Mapping and Virtual Reality (VR) Visualization. *Drones*, *5*, 36. doi:10.3390/drones5020036
- Li, P., & Zhang, X. (2013, October). Integrating GPS and GLONASS to Accelerate Convergence and Initialization Times of Precise Point Positioning. *GPS Solutions*, *18*, 461-471. doi:10.1007/s10291-013-0345-5

- Lillesand, T. M., Kiefer, R. W., & Chipman, J. W. (2015, February 18). *Remote Sensing and Image Interpretation*. WILEY.
- Lu, F., & Li, J. (2011, June). Precise Point Positioning Study to Use Different IGS Precise Ephemeris. *2011 IEEE International Conference on Computer Science and Automation Engineering*. 3. IEEE. doi:10.1109/csae.2011.5952748
- Martín, A., Anquela, A. B., Capilla, R., & Berné, J. L. (2011). PPP Technique Analysis Based on Time Convergence, Repeatability, IGS Products, Different Software Processing, and GPS+GLONASS Constellation. *Journal of Surveying Engineering*, 137, 99-108. doi:10.1061/(ASCE)SU.1943-5428.0000047
- Martínez-Carricondo, P., Agüera-Vega, F., Carvajal-Ramírez, F., Mesas-Carrascosa, F.-J., García-Ferrer, A., & Pérez-Porras, F.-J. (2018, October). Assessment of UAV-Photogrammetric Mapping Accuracy Based on Variation of Ground Control Points. *International Journal of Applied Earth Observation and Geoinformation*, 72, 1–10. doi:10.1016/j.jag.2018.05.015
- Mugnai, F., & Tucci, G. (2022, February). A Comparative Analysis of Unmanned Aircraft Systems in Low Altitude Photogrammetric Surveys. *Remote Sensing*, 14, 726. doi:10.3390/rs14030726
- Naanouh, Y., & Stanislava, V. (2021, October). Digital Documentation and a 3-D Model of Beaufort Castle via RTK GNSS, Terrestrial Laser Scanner and UAS-based Photogrammetry. In E. W. of Conferences (Ed.), *Annual International Scientific Conference "Spatial Data: Science, Research and Technology 2021*. 310. EDP Sciences, 2021. Retrieved from <https://doi.org/10.1051/e3sconf/202131005002>

- NGS. (2020, December). About OPUS. *About OPUS*. Retrieved from <https://geodesy.noaa.gov/OPUS/about.jsp>
- NovAtel. (2015). *An Introduction to GNSS* (2nd ed.). 1120-68th Avenue N.E., Calgary, Alberta, Canada, T2E8S5: NovAtel Inc.
- NovAtel. (2020, August). Process Data. Retrieved from https://docs.novatel.com/Waypoint/Content/Inertial_Explorer/Process_IMU_Data.htm?TocPath=Inertial Explorer/GrafNav|Getting Started with Inertial Explorer|____3
- OCS. (2022). *Hydrographic Survey Specifications and Deliverables*. Tech. rep., NOAA. Retrieved from https://nauticalcharts.noaa.gov/publications/docs/standards-and-requirements/specs/HSSD_2022.pdf
- Oniga, V.-E., Breaban, A.-I., & Statescu, F. (2018, March). Determining the Optimum Number of Ground Control Points for Obtaining High Precision Results Based on UAS Images. *Proceedings*, 2, 352. doi:10.3390/ecrs-2-05165
- Over, J.-S. R., Ritchie, A. C., Kranenburg, C. J., Brown, J. A., Buscombe, D. D., Noble, T., . . . Wernette, P. A. (2021). Processing Coastal Imagery With Agisoft Metashape Professional Edition, Version 1.6 - Structure from Motion Workflow Documentation. *Processing Coastal Imagery With Agisoft Metashape Professional Edition, Version 1.6 - Structure from Motion Workflow Documentation*. US Geological Survey. doi:10.3133/ofr20211039
- Padró, J.-C., Muñoz, F.-J., Planas, J., & Pons, X. (2019, March). Comparison of four UAV georeferencing methods for environmental monitoring purposes focusing on the combined use with airborne and satellite remote sensing platforms. *International Journal*

- of Applied Earth Observation and Geoinformation*, 75, 130–140.
doi:10.1016/j.jag.2018.10.018
- Pix4D. (2017). *Pix4Dmapper 4.1 User Manual*. Retrieved from <https://support.pix4d.com/hc/en-us/articles/204272989-Offline-Getting-Started-and-Manual-pdf>
- Rabah, M., Basiouny, M., Ghanem, E., & Elhadary, A. (2018, May). Using RTK and VRS in Direct Geo-referencing of the UAV Imagery. *NRIAG Journal of Astronomy and Geophysics*, 7, 220-226. doi:10.1016/j.nrjag.2018.05.003
- Rogers, S. R., Manning, I., & Livingstone, W. (2020, August). Comparing the Spatial Accuracy of Digital Surface Models from Four Unoccupied Aerial Systems: Photogrammetry Versus LiDAR. *Remote Sensing*, 12, 2806. doi:10.3390/rs12172806
- Rokaha, B., Gautam, B. P., & Kitani, T. (2019). Building a Reliable and Cost-Effective RTK-GNSS Infrastructure for Precise Positioning of IoT Applications. *2019 Twelfth International Conference on Mobile Computing and Ubiquitous Network (ICMU)*, (pp. 1-4).
- Sanz-Ablanedo, E., Chandler, J., Rodríguez-Pérez, J. R., & Ordóñez, C. (2018, October). Accuracy of Unmanned Aerial Vehicle (UAV) and SfM Photogrammetry Survey as a Function of the Number and Location of Ground Control Points Used. *Remote Sensing*, 10, 1606. doi:10.3390/rs10101606
- Schwind, M., & Starek, M. (2017, October). Structure-from-Motion Photogrammetry: How to Produce High-Quality 3D Point Clouds. *GIM International*, 31(10), 36-37.
- Sickle, J. V. (2015, June 1). *GPS for Land Surveyors*. Taylor & Francis Inc.

- Slocum, R. K., & Parish, C. E. (2017, April). Simulated Imagery Rendering Workflow for UAS-Based Photogrammetric 3D Reconstruction Accuracy Assessments. *Remote Sensing*, 9, 396. doi:10.3390/rs9040396
- Smith, D., Choi, K., Prouty, D., Jordan, K., & Henning, W. (2014, November). Analysis of the TXDOT RTN and OPUS-RS from the Geoid Slope Validation Survey of 2011: Case Study for Texas. *Journal of Surveying Engineering*, 140, 05014003. doi:10.1061/(asce)su.1943-5428.0000136
- Smith, H. (2020, February). Geographic vs Projected Coordinate Systems. *Geographic vs Projected Coordinate Systems*. Retrieved from https://www.esri.com/arcgis-blog/products/arcgis-pro/mapping/gcs_vs_pcs/#:text=What is the difference between, map or a computer screen.
- Sony. (n.d.). RX1R II Professional Compact Camera with 35 mm Sensor - Full Specifications and Features. *RX1R II Professional Compact Camera with 35 mm Sensor - Full Specifications and Features*. Retrieved from <https://www.sony.com/electronics/cyber-shot-compact-cameras/dsc-rx1rm2/specifications>
- Starek, M. J., Gingras, M., & Jeffress, G. (2019). Application of Unmanned Aircraft Systems for Coastal Mapping and Resiliency. In A. Rajabifard (Ed.). CRC Press. Retrieved from <https://library.oapen.org/handle/20.500.12657/24929>
- Thomas, O., Stallings, C., & Wilkinson, B. (2020, March). Unmanned Aerial Vehicles Can Accurately, Reliably, and Economically Compete with Terrestrial Mapping Methods. *Journal of Unmanned Vehicle Systems*, 8, 57-74. doi:10.1139/juvs-2018-0030

- Tmušić, G., Manfreda, S., Aasen, H., James, M., Gonçalves, G., Ben-Dor, E., . . . McCabe, M. (2020, March). Current Practices in UAS-Based Environmental Practices. *Remote Sensing*, 12. doi:10.3390/rs12061001
- Toffanin, P. (2020). Installation and Getting Started. *Installation and Getting Started*.
<https://docs.opendronemap.org/installation/>. Retrieved from
<https://docs.opendronemap.org/installation/>
- Trimble. (2018). Trimble GNSS Planning Online. *Trimble GNSS Planning Online*.
<https://www.gnssplanning.com/#/settings>. Retrieved from
<https://www.gnssplanning.com/#/settings>
- Turner, D., Luciee, A., & Wallace, L. (2014, May). Direct Georeferencing of Ultrahigh-Resolution UAV Imagery. *IEEE Transactions on Geoscience and Remote Sensing*, 52, 2738–2745. doi:10.1109/tgrs.2013.2265295
- Uysal, M., Toprak, A. S., & Polat, N. (2015, September). DEM Generation with UAV Photogrammetry and Accuracy Analysis in Sahitler Hill. *Measurement*, 73, 539–543. doi:10.1016/j.measurement.2015.06.010
- Wingtra. (n.d.). PPK Geotagging. *PPK Geotagging*. Retrieved from
<https://knowledge.wingtra.com/en/ppk-geotagging>
- Wingtra. (n.d.). WingtraOne Drone: Technical Specifications. *WingtraOne Drone: Technical Specifications*.
- Wolf, P. R., Dewitt, B. A., & Wilkinson, B. E. (2014, January 7). *Elements of Photogrammetry with Application in GIS, Fourth Edition*. McGraw-Hill Education - Europe.
- Xu, Z., Yang, J., Peng, C., Wu, Y., Jiang, X., Li, R., . . . Tian, B. (2014, July). Development of an UAS for Post-Earthquake Disaster Surveying and Its Application in Ms7.0 Lushan

Earthquake, Sichuan, China. *Computers & Geosciences*, 68, 22-30.

doi:10.1016/j.cageo.2014.04.001

APPENDIX A

FIELD NOTES AND SUMMARY OF WORKFLOW

Field notes from Mustang Island State Park survey (July 13, 2021).

MUSTANG ISLAND STATE PARK		07/13/2021
21-07-13-MUSTANG NOAA		240713c
STATIC UP: 08:00		88°F, cloudy
STATIC DOWN: 13:49		
Wingtra flight 1		
Wind: 7.5 mph onshore		
partially cloudy		
Lower plotter	Direction: 32°	Start: 8:42am
GSD: 1cm/px	Sidelap: 80%	End: 8:52am
Flying height: 75m	Frontlap: 70%	
Flight 2 (Wingtra)	Direction: 32°	Start: 9:02am
GSD: 1.6 cm/px	Sidelap: 80%	End: 9:10am
Flying height: 120m	Frontlap: 70%	
<u>DJI DDK</u>		<u>DJI RTK</u>
Start: 11:12am		Start: 12:05pm
End: 11:51am		End: 12:36pm
Flying height: 59m		Flying height: 59m
TLS Start: 5:29pm		
TLS End: 6:15pm		
3 scanning setups		
Fast		
GCPs in 2-1-2 staggered pattern ~20m spacing		
10" observations		
Elevation profiles → shore to dunes		
# of lines: 4		

Figure 54. Mustang Island State Park survey field notes.

Summarized workflow for planning, data collection, post-collection, and processing phases of the Mustang Island State Park Survey.

Pre-Survey Preparation

- Use GNSS Planner to select an adequate survey date/time.
- Design the WingtraOne UAS flight missions (75m AGL + 120m AGL, PPK mode).
- Design the DJI Phantom 4 RTK flight missions (59m AGL, RTK + PPK modes).
- Charge all batteries for the equipment to be used.
- Load equipment into the truck (GNSS receivers, data collector, WingtraOne UAS, DJI Phantom 4 RTK, remote controller, aerial targets, tripod for the base station, wind reader, memory cards, etc.)

Survey – Ground Truth

- Take notes about environmental/weather conditions (wind speed, survey location, etc.).
- Set up the base station at a location free of obstructions.
- Link data collector to the base receiver.
- Start collecting GNSS data on the base station at logging intervals of 1 second (1 hertz).
- Lay out aerial targets appropriately.
- Verify that the batteries are charged, and the memory cards are inserted.
- Connect to the TxDOT RTN.
- Survey ground control using RTK GNSS (10-second average).
- Survey ground control using a total station:
 - Use RTK GNSS to establish two temporary stations for the total station survey.
 - Set temporary stations just outside the area covered by all the ground control. Mark these points with rebar nailed to the ground as deeply as possible.

- Take total station measurements on each of the targets with the total station from one of the stations, and once complete, move the total station to the second station and re-survey all targets. Backsight the initial station.
- Collect laser scanner measurements from three pre-established stations, using TxDOT RTN for station locations with Riegl antenna.
- Collect RTK GNSS height profiles along four transects on the beach.

Survey - WingtraOne UAS flight (PPK mode)

- Select the 75m AGL PPK mission and double-check that it is in order.
- Place the platform on the site of deployment. Make sure that no obstructions are nearby.
- Deploy platform and start flight mission. Keep visual sight of the platform at all times and make sure to halt the mission for battery change as needed.
- Once completed, change batteries, and repeat this process with the 120m AGL design.

Survey - DJI Phantom 4 RTK flight (RTK mode + PPK mode)

- For RTK mode, make sure to enable the RTK functionality and connect to the TxDOT RTN. For PPK mode, make sure to disable the RTK functionality. Need not connect to TxDOT RTN.
- Place the platform on the site of deployment. Make sure that no obstructions are nearby.
- Deploy platform and start flight mission. Keep visual sight of the platform at all times and make sure to halt the mission for battery change as needed.

Post-Survey

- Make sure that all ground truth measurements have been collected.
- Collect all ground control and the base station.
- Back in the office, download the data acquired in the field then store the equipment.

- Generate RINEX files using SBF Converter (observation, GPS, and GLONASS).
- Retrieve precise ephemeris base station coordinates from OPUS (using the observation file from the base station).
- Separate the GNSS data from the rover into CGPs data and transect data.
- Use SurvNET to perform a least-squares adjustment on total station points holding to RTK GNSS 3D coordinates from the first temporary station and azimuth from both temporary stations 1 and 2.
- Clean the point cloud data generated using the laser scanner.
- Use RTK GNSS to establish two temporary stations for the total station survey.
- Data Processing
 - GNSS evaluation: process the acquired data using different combinations of GNSS techniques (PPK, RTK, PPP). Process supplementary data in autonomous mode as well as using GCPs.
 - SfM evaluation: process the acquired data using different combinations of SfM software (Drone2Map, Metashape, ODM, and Pix4D).

APPENDIX B

GNSS DATA PREPARATION

OPUS sample result (precise coordinates).

```

1  FILE: 210713c.210 OP1629349602198
2
3  1008  NOTE: You provided a zero or negative antenna height.
4  1008  If ARP HGT = 0.0, OPUS solves for the position of your selected antenna's reference point (ARP).
5  1008  If ARP HGT < 0.0, OPUS solves for a location inside or above the antenna
6  1008
7
8          NGS OPUS SOLUTION REPORT
9          =====
10
11 All computed coordinate accuracies are listed as peak-to-peak values.
12 For additional information: https://nam12.safelinks.protection.outlook.com/?url=https%3A%2F%2Fwww.ngs.noaa.gov
13
14 USER: jcongo@islander.tamucc.edu          DATE: August 19, 2021
15 RINEX FILE: 2107194n.21o                  TIME: 05:08:09 UTC
16
17 SOFTWARE: page5 2008.25 master51.pl 160321  START: 2021/07/13 13:00:00
18 EPHEMERIS: igs21662.eph [precise]          STOP: 2021/07/13 18:48:00
19 NAV FILE: brdc1940.21n                    OBS USED: 14126 / 15080 : 94%
20 ANT NAME: SEPALTUS_NR3 NONE                # FIXED AMB: 82 / 109 : 75%
21 ARP HEIGHT: 0.000                          OVERALL RMS: 0.026(m)
22
23
24 REF FRAME: NAD_83(2011) (EPOCH:2010.0000)  ITRF2014 (EPOCH:2021.5306)
25
26 X: -705740.101(m) 0.014(m) -705740.965(m) 0.014(m)
27 Y: -5608572.631(m) 0.049(m) -5608571.136(m) 0.049(m)
28 Z: 2944108.063(m) 0.023(m) 2944107.840(m) 0.023(m)
29
30 LAT: 27 40 10.21991 0.005(m) 27 40 10.23424 0.005(m)
31 E LON: 262 49 40.90706 0.020(m) 262 49 40.86898 0.020(m)
32 W LON: 97 10 19.09294 0.020(m) 97 10 19.13102 0.020(m)
33 EL HGT: -22.469(m) 0.052(m) -23.791(m) 0.052(m)
34 ORTHO HGT: 3.637(m) 0.081(m) [NAVD88 (Computed using GEOID18)]
35
36
37 UTM COORDINATES STATE PLANE COORDINATES
38 Northing (Y) [meters] UTM (Zone 14) SPC (4205 TX S)
39 Easting (X) [meters] 3061928.619 5222592.263
40 Convergence [degrees] 680299.401 431016.540
41 Point Scale 0.84911389 0.60293333
42 Combined Factor 1.00000127 0.99996262
43 1.00000480 0.99996615
44
45 US NATIONAL GRID DESIGNATOR: 14RPR8029961928(NAD 83)
46
47
48 BASE STATIONS USED
49 PID DESIGNATION LATITUDE LONGITUDE DISTANCE(m)
50 DF4377 TXCC CORPUS CHRISTI R2 CORS ARP N274426.855 W0972630.010 27748.1
51 DL7624 TXPV PORT LAVACA CORS ARP N283817.423 W0963706.661 120326.4
52 DM3533 TXBE BEEVILLE CORS ARP N282525.219 W0974407.622 100270.3
53
54 NEAREST NGS PUBLISHED CONTROL POINT
55 AC8450 C 1518 N274000021. W0971000029. 456.3
56
57 This position and the above vector components were computed without any
58 knowledge by the National Geodetic Survey regarding the equipment or
59 field operating procedures used.

```

Figure 55. Precise OPUS solution using the local base station at Mustang Island State Park.

GNSS data decimation using TEQC.

The first two lines show the decimation of 1s GNSS data for TXPO and TXCC into 5 seconds.

The third line shows the decimation of 1s TXPO data into 15 seconds.

The fourth line shows the decimation of 1s TXPO data into 30 seconds.

```
C:\Users\jcong\Downloads\teqc_mingw_64>teqc.exe -0.int 1 -0.dec 5 txpo_day194_1sec.21o > txpo_day194_5sec.21o
C:\Users\jcong\Downloads\teqc_mingw_64>teqc.exe -0.int 1 -0.dec 5 txcc_day194_1sec.21o > txcc_day194_5sec.21o
C:\Users\jcong\Downloads\teqc_mingw_64>teqc.exe -0.int 1 -0.dec 15 txpo_day194_1sec.21o > txpo_day194_15sec.21o
C:\Users\jcong\Downloads\teqc_mingw_64>teqc.exe -0.int 1 -0.dec 30 txpo_day194_1sec.21o > txpo_day194_30sec.21o
```

Figure 56. Command-line capture of 1s data decimation for TXPO and TXCC stations.

NRC GNSS data merge.

Because the NRC observation data is grouped into single hours, they had to be merged into a single observation file before submission into OPUS. This process was also performed with TEQC using the prompt displayed below.

```
C:\Users\jcong\Downloads\21_07_13_Antenna_On_NRC\194\1_second_obs>teqc.exe -0.dec 1 +obs + +nav +,+ -tbin 1d
2107130*.21o
teqc: creating file 'tbinoutput1940.21o' ...
! Notice ! splicing RINEX files
! Notice ! splicing RINEX files
! Notice ! splicing RINEX files
! Notice ! splicing RINEX files
! Notice ! splicing RINEX files
! Notice ! splicing RINEX files
! Notice ! splicing RINEX files
! Notice ! splicing RINEX files
! Notice ! splicing RINEX files
! Notice ! splicing RINEX files
C:\Users\jcong\Downloads\21_07_13_Antenna_On_NRC\194\1_second_obs>
```

Figure 57. Command-line capture of 1s data merge for the GNSS Trimble Antenna at
TAMUCC's NRC Building.

APPENDIX C

WINGTRAHUB OUTPUT FORMATS AND PROCESSING REPORTS

WingtraHub output formats for generating image geotags.

Geotag file format (CSV):	Agisoft Metashape	▼
image name, longitude [decimal degrees], latitude [decimal degrees], altitude [meter], yaw [degrees], pitch [degrees], roll [degrees], accuracy horizontal [meter], accuracy vertical [meter]		

Geotag file format (CSV):	Pix4D	▼
image name, latitude [decimal degrees], longitude [decimal degrees], altitude [meter], omega [degrees], phi [degrees], kappa [degrees], accuracy horizontal [meter], accuracy vertical [meter]		

Figure 58. Metashape and Pix4D geotag WingtraHub output formats.

Geotag file format (CSV):	Lat/Long/Alt	▼
image name, latitude [decimal degrees], longitude [decimal degrees], altitude [meter]		

Geotag file format (CSV):	Long/Lat/Alt	▼
image name, longitude [decimal degrees], latitude [decimal degrees], altitude [meter]		


Geotag file format (CSV):	Custom	▼ 
image name, latitude [decimal degrees], longitude [decimal degrees], altitude [meter], omega [degrees], phi [degrees], kappa [degrees], roll [degrees], pitch [degrees], yaw [degrees], accuracy horizontal [meter], accuracy vertical [meter], accuracy roll/omega [degrees], accuracy pitch/phi [degrees], accuracy yaw/kappa [degrees], coordinate system, coordinate system vertical, time		

Figure 59. Lat/Lon/Alt (top) vs Long/Lat/Alt vs Custom geotag WingtraHub output formats.

Example of WingtraHub processing reports (using WingtraOne UAS imagery at 120 m AGL and PPK processing using the local base station at various sampling rates).

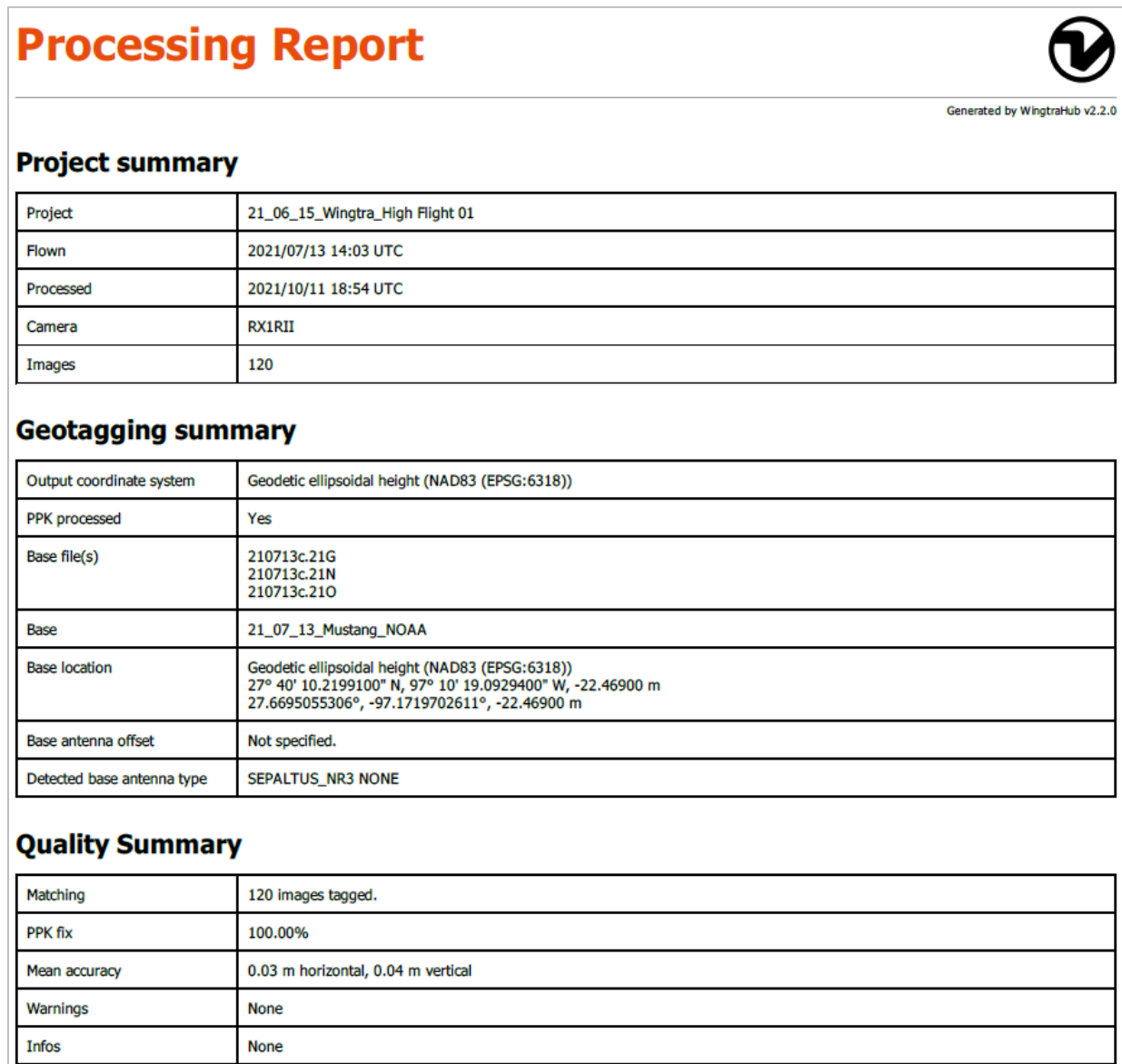


Figure 60. WingtraHub processing report using dataset from WingtraOne UAS at 120 m AGL, 1-second sampling rate, local base.

Processing Report



Generated by WingtraHub v2.2.0

Project summary

Project	21_06_15_Wingtra_High Flight 01
Flown	2021/07/13 14:03 UTC
Processed	2021/10/12 03:44 UTC
Camera	RX1RII
Images	120

Geotagging summary

Output coordinate system	Geodetic ellipsoidal height (NAD83 (EPSG:6318))
PPK processed	Yes
Base file(s)	210713c.21G 210713c.21N localbase_5sec.21o
Base	21_07_13_Mustang_NOAA
Base location	Geodetic ellipsoidal height (NAD83 (EPSG:6318)) 27° 40' 10.2199100" N, 97° 10' 19.0929400" W, -22.46900 m 27.6695055306°, -97.1719702611°, -22.46900 m
Base antenna offset	Not specified.
Detected base antenna type	SEPALTUS_NR3 NONE

Quality Summary

Matching	120 images tagged.
PPK fix	100.00%
Mean accuracy	0.03 m horizontal, 0.04 m vertical
Warnings	None
Infos	None

Figure 61. WingtraHub processing report using dataset from WingtraOne UAS at 120 m AGL, 5-second sampling rate, local base.

Processing Report



Generated by WingtraHub v2.2.0

Project summary

Project	21_06_15_Wingtra_High Flight 01
Flown	2021/07/13 14:03 UTC
Processed	2021/10/12 03:45 UTC
Camera	RX1RII
Images	120

Geotagging summary

Output coordinate system	Geodetic ellipsoidal height (NAD83 (EPSG:6318))
PPK processed	Yes
Base file(s)	210713c.21G 210713c.21N localbase_15sec.21o
Base	21_07_13_Mustang_NOAA
Base location	Geodetic ellipsoidal height (NAD83 (EPSG:6318)) 27° 40' 10.2199100" N, 97° 10' 19.0929400" W, -22.46900 m 27.6695055306°, -97.1719702611°, -22.46900 m
Base antenna offset	Not specified.
Detected base antenna type	SEPALTUS_NR3 NONE

Quality Summary

Matching	120 images tagged.
PPK fix	100.00%
Mean accuracy	0.03 m horizontal, 0.04 m vertical
Warnings	None
Infos	None

Figure 62. WingtraHub processing report using dataset from WingtraOne UAS at 120 m AGL, 15-second sampling rate, local base.

Processing Report



Generated by WingtraHub v2.2.0

Project summary

Project	21_06_15_Wingtra_High Flight 01
Flown	2021/07/13 14:03 UTC
Processed	2021/10/12 03:46 UTC
Camera	RX1RII
Images	120

Geotagging summary

Output coordinate system	Geodetic ellipsoidal height (NAD83 (EPSG:6318))
PPK processed	Yes
Base file(s)	210713c.21G 210713c.21N localbase_30sec.21o
Base	21_07_13_Mustang_NOAA
Base location	Geodetic ellipsoidal height (NAD83 (EPSG:6318)) 27° 40' 10.2199100" N, 97° 10' 19.0929400" W, -22.46900 m 27.6695055306°, -97.1719702611°, -22.46900 m
Base antenna offset	Not specified.
Detected base antenna type	SEPALTUS_NR3 NONE

Quality Summary

Matching	120 images tagged.
PPK fix	100.00%
Mean accuracy	0.03 m horizontal, 0.04 m vertical
Warnings	- The base file update interval is larger than 25s.
Infos	None

Figure 63. WingtraHub processing report using dataset from WingtraOne UAS at 120 m AGL, 30-second sampling rate, local base.

APPENDIX D

PPK PROCESSING

Base stations used for PPK processing.

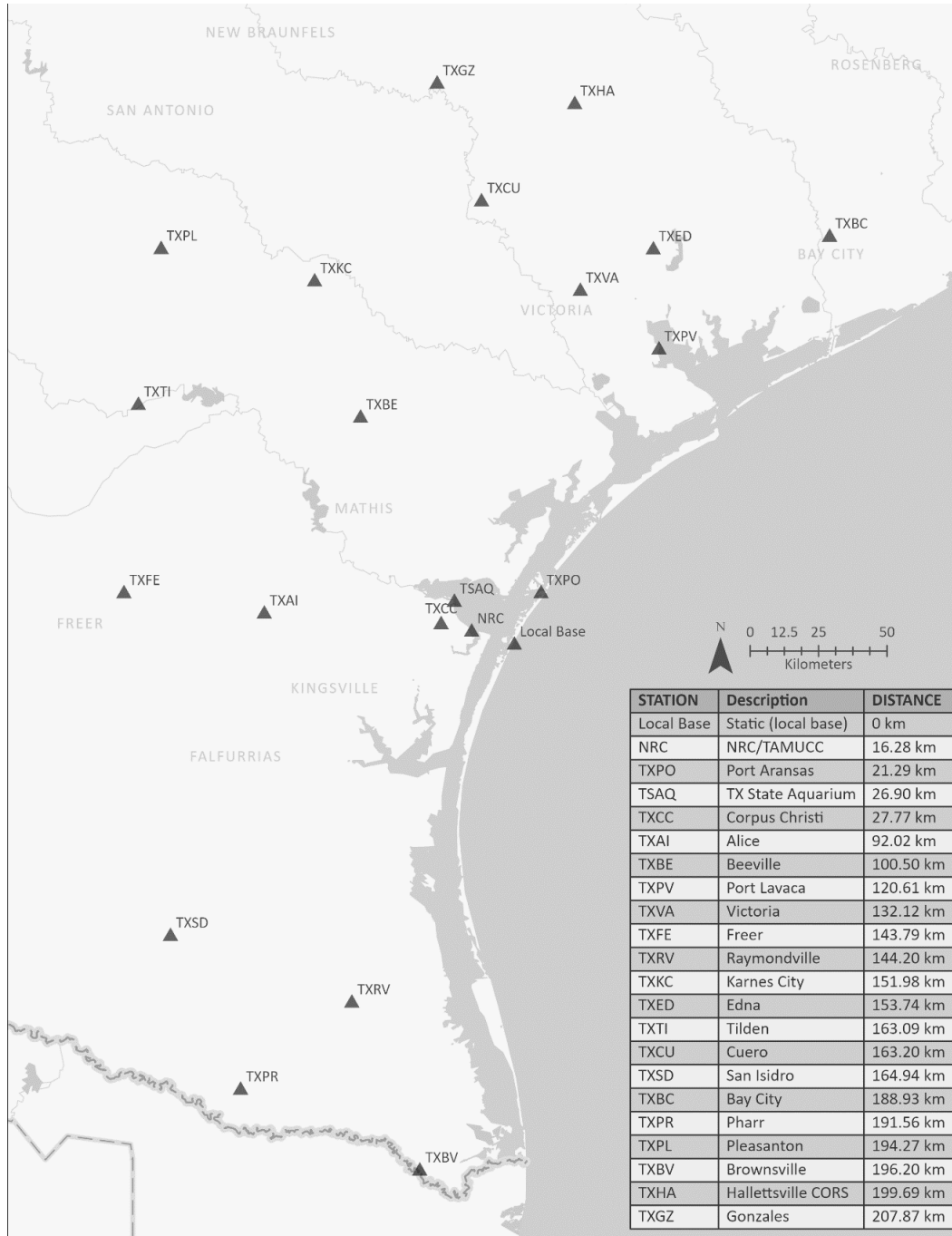


Figure 64. Map of all base stations used for PPK processing of the Mustang Island State Park dataset.

Local and remote base stations located within 30 km of Mustang Island State Park that were used for PPK processing.

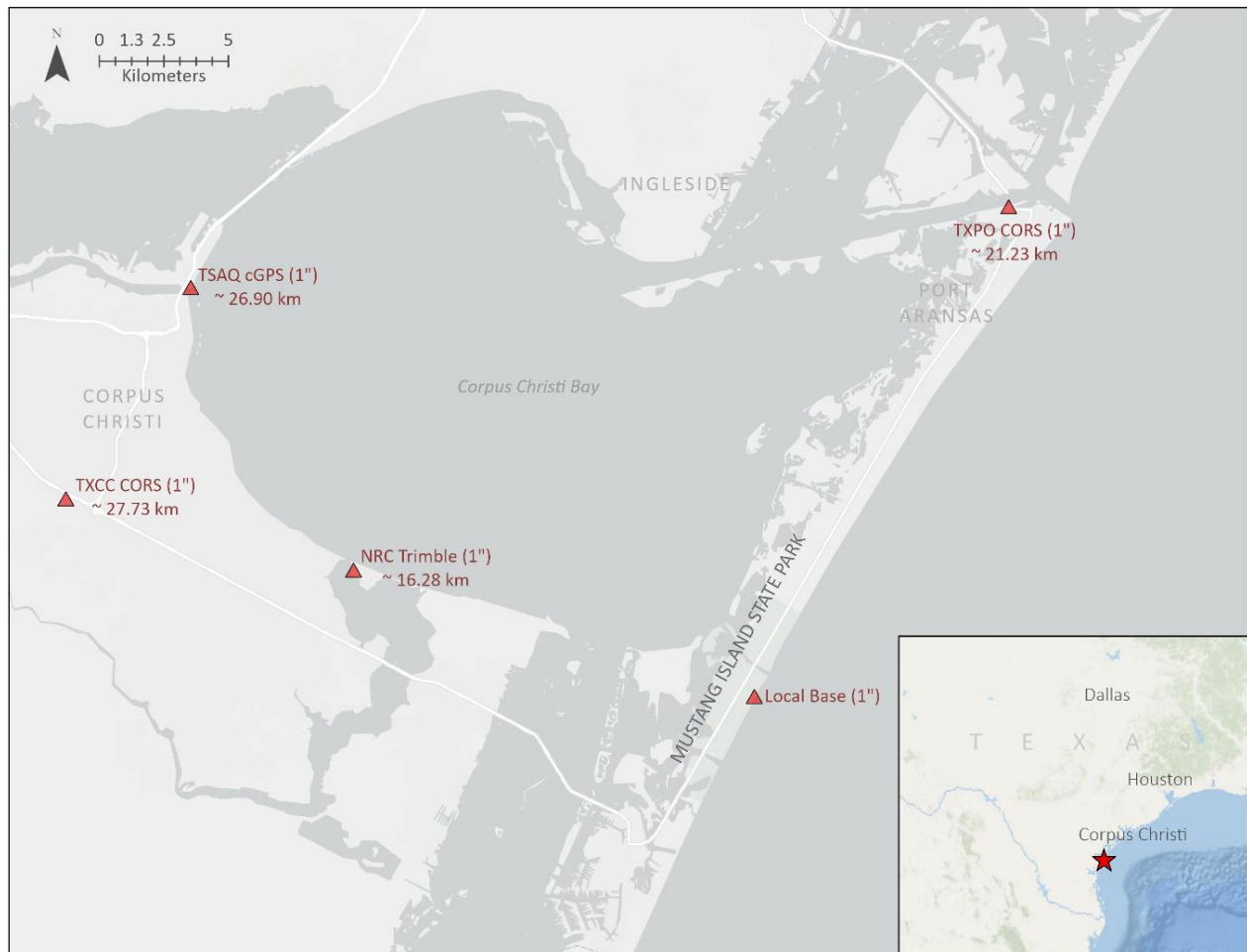


Figure 65. Base stations located within 30 km of the Mustang Island State Park survey site.

Combined tables summarizing PPK processing results from WingtraHub and Pix4D reports.

Table 32. WingtraHub and Pix4D PPK processing accuracies (Mustang Island State Park, 1s sampling rate WingtraOne UAS at 120 m AGL, RMSEs relative to total station control).

	Location	Distance (km)	PPK Fix (%)	Mean accuracy (horiz., m)	Mean accuracy (vert., m)	Z RMSE (cm)	Z Mean (cm)
Local Base	Mustang Island State Park	-	100.00	0.03	0.04	8.85	-8.74
NRC	NRC Trimble	16.28	93.33	0.06	0.14	4.01	3.78
TXPO	Port Aransas	21.29	92.50	0.16	0.22	22.16	22.09
TSAQ	TX State Aquarium cGPS	26.90	100.00	0.07	0.10	2.44	2.01
TXCC	Corpus Christi	27.77	100.00	0.07	0.10	4.31	4.09
TXAI	Alice	92.02	68.33	0.25	0.44	19.39	-19.31
TXBE	Beeville	100.50	82.50	0.24	0.41	2.69	-2.37
TXPV	Port Lavaca	120.61	23.33	1.30	1.49	56.14	-54.81
TXVA	Victoria	132.12	35.00	0.56	0.76	15.01	-14.47
TXFE	Freer	143.79	50.83	0.33	0.62	20.77	-20.73
TXRV	Raymondville	144.20	00.00	2.24	2.62	116.15	-115.85
TXKC	Karnes City	151.98	57.50	0.39	0.63	28.32	-28.28
TXED	Edna	153.74	30.00	0.85	1.08	34.01	-33.28
TXTI	Tilden	163.09	00.00	2.28	2.75	37.76	-37.68
TXCU	Cuero	163.20	60.83	0.39	0.65	16.19	-16.16
TXSD	San Isidro	164.94	35.00	0.43	0.81	58.48	-58.39
TXBC	Bay City	188.93	16.67	1.59	2.12	24.56	-23.55
TXPR	Pharr	191.56	24.17	2.38	3.23	59.54	-59.34
TXPL	Pleasanton	194.27	29.17	1.03	1.34	56.57	-56.39
TXBV	Brownsville	196.20	21.67	1.94	2.69	66.74	-66.68
TXHA	Hallettsville	199.69	5.83	2.76	3.18	117.52	-117.03
TXGZ	Gonzales	207.87	00.00	2.59	2.83	128.42	-128.13

Table 33. WingtraHub and Pix4D PPK processing accuracies (Mustang Island State Park, 5s sampling rate WingtraOne UAS at 120 m AGL, RMSEs relative to total station control).

	Location	Distance (km)	PPK Fix (%)	Mean accuracy (horiz., m)	Mean accuracy (vert., m)	Z RMSE (cm)	Z Mean (cm)
Local Base	Mustang Island State Park	-	100.00	0.03	0.04	8.79	-8.67
NRC	NRC Trimble	16.28	95.00	0.06	0.13	3.00	2.81
TXPO	Port Aransas	21.29	98.33	0.06	0.10	5.55	5.39
TSAQ	TX State Aquarium cGPS	26.90	100.00	0.07	0.10	3.78	3.39
TXCC	Corpus Christi	27.77	100.00	0.07	0.10	2.73	2.45
TXAI	Alice	92.02	45.83	0.26	0.48	24.67	-24.62
TXBE	Beeville	100.50	85.83	0.24	0.42	6.95	-6.82
TXPV	Port Lavaca	120.61	48.33	0.40	0.58	9.89	-9.66
TXVA	Victoria	132.12	29.17	0.54	0.82	19.49	-18.98
TXFE	Freer	143.79	46.67	0.86	1.11	37.37	-37.16
TXRV	Raymondville	144.20	55.83	0.46	0.77	54.31	-54.27
TXKC	Karnes City	151.98	74.17	0.38	0.62	27.58	-27.53
TXED	Edna	153.74	49.17	0.52	0.75	24.99	-24.69
TXTI	Tilden	163.09	28.33	0.70	1.08	16.83	-16.78
TXCU	Cuero	163.20	58.33	0.38	0.63	24.08	-24.04
TXSD	San Isidro	164.94	00.00	1.72	1.99	51.44	-50.57
TXBC	Bay City	188.93	27.50	0.98	1.30	27.43	-26.17
TXPR	Pharr	191.56	51.67	0.54	1.08	45.39	-45.33
TXPL	Pleasanton	194.27	45.83	1.05	1.34	55.95	-55.78
TXBV	Brownsville	196.20	52.50	0.69	1.15	55.91	-55.88
TXHA	Hallettsville	199.69	23.33	1.01	1.25	45.35	-45.06
TXGZ	Gonzales	207.87	24.17	1.25	1.48	68.29	-67.13

Table 34. WingtraHub and Pix4D PPK processing accuracies (Mustang Island State Park, 15s sampling rate WingtraOne UAS at 120 m AGL, RMSEs relative to total station control).

	Location	Distance (km)	PPK Fix (%)	Mean accuracy (horiz., m)	Mean accuracy (vert., m)	Z RMSE (cm)	Z Mean (cm)
Local Base	Mustang Island State Park	-	100.00	0.03	0.04	8.81	-8.69
NRC	NRC Trimble	16.28	95.00	0.06	0.13	1.38	0.97
TXPO	Port Aransas	21.29	98.33	0.06	0.10	5.98	5.86
TSAQ	TX State Aquarium cGPS	26.90	100.00	0.07	0.10	1.64	0.48
TXCC	Corpus Christi	27.77	100.00	0.07	0.10	4.89	4.74
TXAI	Alice	92.02	72.50	0.25	0.46	13.72	-13.64
TXBE	Beeville	100.50	79.17	0.24	0.41	5.23	-5.04
TXPV	Port Lavaca	120.61	60.00	0.33	0.53	9.67	-9.49
TXVA	Victoria	132.12	34.17	0.53	0.74	18.02	-17.34
TXFE	Freer	143.79	47.50	0.85	1.07	41.31	-41.12
TXRV	Raymondville	144.20	50.00	0.51	0.82	52.25	-52.20
TXKC	Karnes City	151.98	84.17	0.35	0.58	29.58	-29.54
TXED	Edna	153.74	56.67	0.42	0.65	20.78	-20.73
TXTI	Tilden	163.09	50.83	0.56	0.91	9.99	-9.89
TXCU	Cuero	163.20	62.50	0.45	0.70	20.32	-20.27
TXSD	San Isidro	164.94	00.00	1.72	1.99	48.26	-47.53
TXBC	Bay City	188.93	6.67	1.14	1.39	48.43	-47.19
TXPR	Pharr	191.56	48.33	0.57	1.08	42.94	-42.87
TXPL	Pleasanton	194.27	28.33	0.55	0.92	47.45	-47.44
TXBV	Brownsville	196.20	65.83	0.64	1.12	65.23	-65.17
TXHA	Hallettsville	199.69	41.67	0.76	1.05	31.55	-31.07
TXGZ	Gonzales	207.87	00.00	1.98	2.18	121.36	-120.95

Table 35. WingtraHub and Pix4D PPK processing accuracies (Mustang Island State Park, 30s sampling rate WingtraOne UAS at 120 m AGL, RMSEs relative to total station control).

	Location	Distance (km)	PPK Fix (%)	Mean accuracy (horiz., m)	Mean accuracy (vert., m)	Z RMSE (cm)	Z Mean (cm)
Local Base	Mustang Island State Park	-	100.00	0.03	0.04	8.36	-8.26
NRC	NRC Trimble	16.28	93.33	0.06	0.13	1.87	1.53
TXPO	Port Aransas	21.29	96.67	0.06	0.10	5.92	5.82
TSAQ	TX State Aquarium cGPS	26.90	100.00	0.07	0.10	2.47	2.13
TXCC	Corpus Christi	27.77	100.00	0.07	0.10	3.21	3.00
TXAI	Alice	92.02	69.17	0.25	0.44	3.22	-2.58
TXBE	Beeville	100.50	87.50	0.24	0.40	4.82	-4.60
TXPV	Port Lavaca	120.61	65.83	0.33	0.53	8.55	-8.47
TXVA	Victoria	132.12	49.17	0.54	0.74	11.68	-10.94
TXFE	Freer	143.79	70.00	0.36	0.62	26.11	-26.07
TXRV	Raymondville	144.20	30.00	0.63	0.96	58.89	-58.84
TXKC	Karnes City	151.98	58.83	0.58	0.89	26.42	-26.39
TXED	Edna	153.74	55.00	0.46	0.70	16.39	-16.15
TXTI	Tilden	163.09	49.17	0.57	0.90	11.90	-11.83
TXCU	Cuero	163.20	64.17	0.40	0.65	17.47	-17.44
TXSD	San Isidro	164.94	00.00	1.72	1.99	47.19	-46.23
TXBC	Bay City	188.93	13.33	1.09	1.64	27.38	-25.57
TXPR	Pharr	191.56	2.50	1.82	2.12	37.36	-35.78
TXPL	Pleasanton	194.27	44.17	0.45	0.77	37.39	-37.38
TXBV	Brownsville	196.20	50.00	0.94	1.40	61.47	-61.24
TXHA	Hallettsville	199.69	40.83	0.77	1.04	33.99	-33.62
TXGZ	Gonzales	207.87	00.00	1.14	1.84	79.83	-79.19

APPENDIX E

PRECISE POINT POSITIONING

Screenshot of Inertial Explorer processing settings.

Process GNSS

Processing Method

☐ Differential GNSS ☒ Precise Point Positioning (PPP)

Processing Direction

☐ Both ☐ Forward ☐ Reverse ☒ Multi-Pass

Processing Settings

Profile: GNSS UAV Advanced ...

Datum: NAD83(2011)

Processing Information

Description: Run (1) User: JPC

Process Save Settings Cancel

Figure 66. Settings used for PPP processing (Inertial Explorer)

Note about CSRS-PPP.

An attempt was made to perform PPP corrections using CSRS (interface shown in Figure 67). Although the CSRS-PPP workflow is not yet satisfactory and requires further assessment, the author deemed it important to briefly discuss it. The service is accessible through the Government of Canada website, under Geodetic Tools and Data. The first step is to create a user account on the Natural Resources Canada website. CSRS-PPP uses only the RINEX observation file from the rover for computing accurate positions for the onboard trajectory. Upon correspondence with the Canadian Geodetic Survey, two methods incorporating the CSRS-PPP service would be dependent on whether (i) the data used is from onboard GNSS data (in which case processing would be done in kinematic mode) or (ii) observations were collected on GCPs (data collected would be processed

in static mode). The former helps to increase the absolute accuracy of the imagery while having less impact on the relative accuracy. The latter would help increase both the absolute and the relative accuracy of the imagery. Although data collected was collected on GCPs, this project used the observation file from the onboard GNSS option because of its focus on eliminating reliance on GCPs.

When using this tool, the processing mode was set to static, and NAD83 Epoch 2010.0 and the Canadian Geodetic Vertical Datum of 2013 (CGVD2013) were selected as horizontal and vertical reference systems, respectively. Lastly, the observation file generated using SBF Converter is loaded into the RINEX space, and the default parameters are used for the rest. CSRS-PPP also decimates the observation file to a sampling rate of 30 seconds. The Canadian Geodetic Survey has a tool named GPS-H, which is often used to convert CGVD2013 elevations into NAD83 (2011). However, this tool was not used in this test because the position estimates generated through CSRS-PPP are initially relative to the ellipsoid as this is the nature of GNSS. The use of GPS-H is encouraged when using orthometric heights, however.

CSRS-PPP results are sent to the email used during registration within 10 minutes of submission as a zip file. The file includes information such as positioning data for each epoch processed, processed, clock offsets, zenith delay, and tropospheric gradient. Because CSRS-PPP solutions include every epoch observed during the flight (including lift and landing, see Figure 68), the user needs to develop a strategy to synchronize only the epochs that match the time in which the photos were taken. CSRS-PPP does not provide such functionality.

Email for results (required)

Processing mode
☒ Static ☐ Kinematic

NAD83 ITRF

Epoch (Adopted)

Vertical datum

Contribute to passive control maintenance? ([What is this?](#))
☐ Authorize the Canadian Geodetic Survey (CGS) to archive and publish CSRS-PPP submission and solution

Official marker station name

[More options](#)

RINEX observation file(s), 300 MB max (.zip, .gz, .Z, .tar, .??O)
 Note: You may submit multiple RINEX files in a single .zip or .tar archive
 No file chosen

☐ Remove plots from CSRS-PPP solution PDF report ([Why?](#))

Figure 67. Interface of CSRS-PPP.

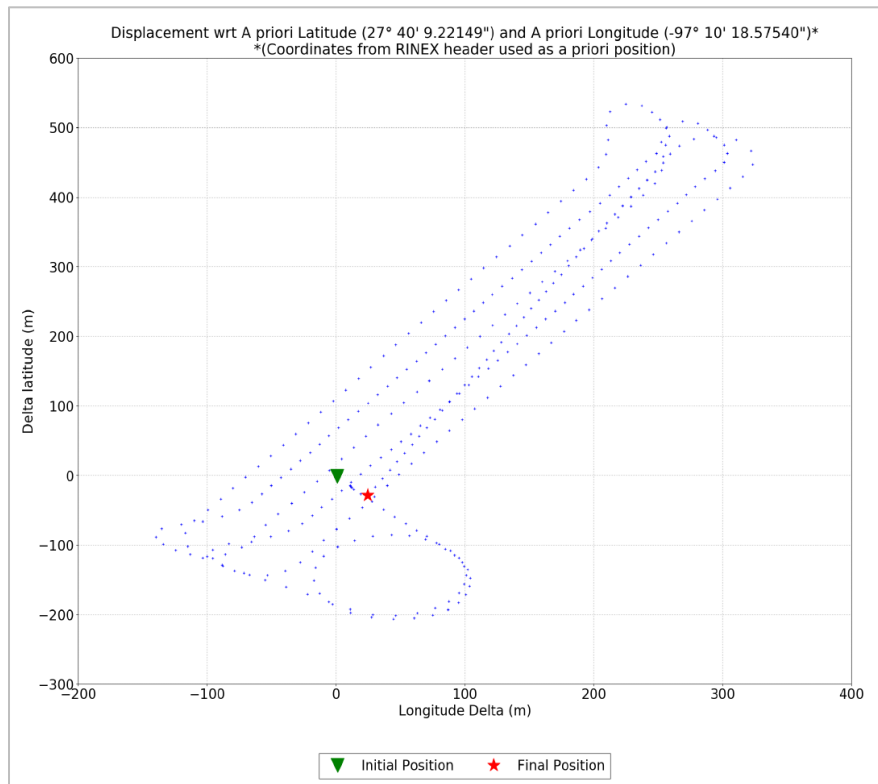


Figure 68. Epochs recorded WingtraOne UAS PPK (WingtraOne UAS at Mustang Island State Park, 120 m AGL, CSRS-PPP report).

APPENDIX F

HEIGHT TRANSECT DIFFERENCES

Excerpt of Python script used for height transect differences between UAS and RTK GNSS.

```
#-----
# Name:      Mustang Island State Park (RTK GNSS vs UAS Heights)
# Purpose:   Accessing ArcPy to list toolboxes and tools
# Created:   April 2022
# Copyright:  Pilartes Congo 2022 (c)
#-----

#import matplotlib library
import matplotlib.pyplot as plt

#variables containing transect data for uas and rtk gnss.
#four transects used altogether

#transect 1
Transect1_Pt_Number = [1, 2, 3, 4, 5, 6, 7, 8, 9, 10, 11];
Transect1_UAS = [-25.359, -25.208, -24.896, -24.697, -24.532, -24.440, -24.333, -24.423, -24.305, -24.137, -24.017];
Transect1_RTK = [-25.490, -25.282, -24.983, -24.775, -24.609, -24.510, -24.394, -24.498, -24.375, -24.209, -24.103];

#transect 2
Transect2_Pt_Number = [12, 13, 14, 15, 16, 17, 18, 19, 20, 21, 22, 23, 24, 25];
Transect2_UAS = [-25.504, -25.241, -25.028, -25.028, -24.697, -24.598, -24.461, -24.341, -24.344, -24.304, -24.258, -24.210, -24.078, -24.186];
Transect2_RTK = [-25.525, -25.286, -25.099, -24.926, -24.766, -24.658, -24.533, -24.391, -24.415, -24.379, -24.343, -24.297, -24.158, -24.278];

#transect 3
Transect3_Pt_Number = [26, 27, 28, 29, 30, 31, 32, 33, 34, 35, 36, 37];
Transect3_UAS = [-25.511, -25.203, -24.952, -24.741, -24.602, -24.542, -24.352, -24.541, -24.303, -24.227, -24.324, -24.401];
Transect3_RTK = [-25.548, -25.228, -25.030, -24.816, -24.678, -24.615, -24.413, -24.618, -24.401, -24.318, -24.412, -24.493];

#transect 4
Transect4_Pt_Number = [38, 39, 40, 41, 42, 43, 44, 45, 46, 47, 48, 49, 50];
Transect4_UAS = [-25.383, -25.178, -24.923, -24.720, -24.611, -24.536, -24.311, -24.257, -24.236, -24.044, -23.957, -23.827, -23.647];
Transect4_RTK = [-25.471, -25.290, -25.028, -24.809, -24.700, -24.619, -24.374, -24.352, -24.317, -24.143, -24.058, -23.910, -23.764];

#plotting of charts using variables/information for each of the transects.
plt.figure(figsize = (10, 8))
plt.plot(Transect1_Pt_Number, Transect1_UAS, '-s', markerfacecolor='white', markersize=5, label = 'UAS at 75m AGL', color='navy')
plt.plot(Transect1_Pt_Number, Transect1_RTK, '-o', markerfacecolor='white', markersize=4, label = 'RTK GNSS', color='green')

plt.plot(Transect2_Pt_Number, Transect2_UAS, '-s', markerfacecolor='white', markersize=5, color='navy')
plt.plot(Transect2_Pt_Number, Transect2_RTK, '-o', markerfacecolor='white', markersize=4, color='green')

plt.plot(Transect3_Pt_Number, Transect3_UAS, '-s', markerfacecolor='white', markersize=5, color='navy')
plt.plot(Transect3_Pt_Number, Transect3_RTK, '-o', markerfacecolor='white', markersize=4, color='green')

plt.plot(Transect4_Pt_Number, Transect4_UAS, '-s', markerfacecolor='white', markersize=5, color='navy')
plt.plot(Transect4_Pt_Number, Transect4_RTK, '-o', markerfacecolor='white', markersize=4, color='green')

#Legend and Labeling
plt.legend(fontsize = 12)
plt.xlabel('Point Number', size=15)
plt.ylabel('Ellip. Height (m)', size=15)
plt.savefig('Transects Combined.png', dpi = 300)
```

Figure 69. Excerpt of Python script used to plot transect height differences.

APPENDIX G

MULTI-STATION ADJUSTMENT REPORT

Multi-station adjustment report from the TLS.

Report for Multi-Station Adjustment

Report date: 2021-07-14
Generated by: jberryhill
Scope: full report

Host application: RiSCAN PRO 2.12
MSA module: 2.7.2-1858+352f3401
Report module: 1.5.0

Platform: Windows-10-10.0.19041-SP0
Hostname: BLUC1977458

1 Project Summary

Project name: 21_07_13_Mustang_NOAA
Global Coordinate Reference System (GLCS): NAD83(2011) / Geocentric (EPSG::6317)
Report GLCS: NAD83(2011) / Texas South / Geoid18 (M) (EPSG::0)

Project origin:

Easting [m]: 431078.2143
Northing [m]: 5222609.0794
Height [m]: 26.1056

Project Coordinate System (PRCS): levelled Cartesian east, north, up system
GNSS Coordinate Reference Systems:

CRS#1 ... NAD83(2011) / Geographic (EPSG::6319)
Report Coordinate System:

PRCS

number of scan positions: 3
bounding box of scanposition centers: (in PRCS)

direction	from [m]	to [m]	width [m]
east	18.945	109.099	90.155
north	100.316	182.222	81.906
height	-23.436	-22.678	0.758

instruments used:

instrument type: VZ-2000i
serial number: H2223746

Figure 70. Page 1 of the MSA report from the TLS (at Mustang Island State Park).

2 Data available in Project

Control point (CtrlP) – Point of known coordinates and accuracy. Control Points are used in multi-station adjustment / scan data adjustment to register pointclouds to a known control survey.

Check point (ChkP) – Check points are a freely selectable subset of the Control points to verify the success of the adjustment process. Check points are not used for pointcloud registration, but serve as an independent set of control.

2.1 Scandata

Name	Date	Time	Horiz. FoV [deg]	Resolution [mdeg]	Point Count	Image Count	Refl. Scans
ScanPos001	2021-07-13	17:36:03	360.00	19.9	35,707,924	9	0
ScanPos002	2021-07-13	17:47:00	360.00	19.9	37,027,225	9	0
ScanPos003	2021-07-13	17:59:43	360.00	19.9	35,650,307	9	0
Total					108,385,456		

2.2 GNSS Measurements

The VZ-2000i acquired the following GNSS measurements at the following scan positions:

Name	CRS	Latitude [deg]	Longitude [deg]	Altitude [m]	Horiz. Acc. [m]	Vert. Acc. [m]	Satel- lites	Nav. Sol.	Age of Corr.
ScanPos001	CRS#1	N27° 40' 10.745112"	W97° 10' 16.836075"	-23.6265	0.014	0.015	12	RTK fixed	1.000
ScanPos002	CRS#1	N27° 40' 14.004325"	W97° 10' 16.144480"	-22.6905	0.014	0.014	12	RTK fixed	1.000
ScanPos003	CRS#1	N27° 40' 16.664692"	W97° 10' 12.855393"	-23.4200	0.014	0.014	12	RTK fixed	1.000

CRS#1 ... NAD83(2011) / Geographic (EPSG::6319)

2.3 Orientation Measurements

The VZ-2000i acquired the following measurements for roll, pitch and yaw angles (all values in deg).

Name	Roll	Pitch	Yaw	Acc. Roll	Acc. Pitch	Acc. Yaw	PoseEstimation Type
ScanPos001	0.554	-1.337	22.239	0.011	0.011	1.240	static
ScanPos002	-0.375	0.886	-34.300	0.011	0.011	1.055	static
ScanPos003	0.991	-0.282	-23.272	0.011	0.011	1.272	static

2.4 Control Points defined in a coordinate reference system

No Control Points in a coordinate reference system used.

2.5 Check Points defined in a coordinate reference system

No Check Points in a coordinate reference system used.

Figure 71. Page 2 of the MSA report from the TLS (at Mustang Island State Park).

2.6 Control Points defined in a locally levelled coordinate system

No Control Points in a locally leveled coordinate system used.

2.7 Check Points defined in a locally levelled coordinate system

No Check Points in a locally leveled coordinate system defined.

3 Data used for Multi-station-Adjustment

3.1 Data per Scan Position

Name	Number of Plane Patches			Plane Patches of Phase 3		
	Phase 1	Phase 2	Phase 3	NS	WE	Horiz.
ScanPos001	521	550	999	7	4	988
ScanPos002	967	1,030	1,597	17	6	1,574
ScanPos003	618	640	853	0	5	848

NS ... North-South, WE ... West-East, Horiz. ... Horizontal

3.2 Control Points used for Multi-Station Adjustment

No Control Points used.

3.3 Tie Points used for Multi-Station Adjustment

No Tie Points used.

4 Results of MSA

4.1 General Information

User Settings:

use CRS control points: False
use SOCS tie points: False
use LLCS control points: False
GNSS measurement usage: yes
GNSS outliers: remove GNNS outliers
GNSS trust level: low
gap closure distance: 0.250 m
adjustment effort: standard
adjustment matches: planes to planes
reporting level: full

Observations Used:

project plane patches: 879
scan position plane patches: 3,449
GNSS measurements: 3

Figure 72. Page 3 of the MSA report from the TLS (at Mustang Island State Park).

```
# orientation measurements: 3
# control points in CRS: 0
# control points in LLCS: 0
# tie points in PRCS: 0
# LLCS: 0
project northing from: GNSS
Adjustment Info:
start time: 2021-07-14T16:14:04
run time: 00:00:42
# parameters estimated: 2,658
```

4.2 Final Poses of Scan Positions

The following positions and orientations have been estimated for the scan positions:

In the PRCS coordinate system:

Name	X [m]	Y [m]	Z [m]	Acc. X [m]	Acc. Y [m]	Acc. Z [m]
ScanPos001	0.016	-0.065	-23.570	0.034	0.025	0.018
ScanPos002	18.945	100.316	-22.678	0.029	0.018	0.018
ScanPos003	109.099	182.222	-23.436	0.045	0.043	0.018

Name	Roll [deg]	Pitch [deg]	Yaw [deg]	Acc. Roll [deg]	Acc. Pitch [deg]	Acc. Yaw [deg]
ScanPos001	0.557	-1.354	15.315	0.006	0.006	0.019
ScanPos002	-0.372	0.887	-41.900	0.006	0.006	0.016
ScanPos003	0.986	-0.278	-31.099	0.006	0.006	0.027

In the coordinate reference system:

Name	Easting [m]	Northing [m]	Height [m]	Acc. East [m]	Acc. North [m]	Acc. Up [m]
ScanPos001	431078.2307	5222609.0150	2.5353	0.034	0.025	0.018
ScanPos002	431096.1014	5222709.5860	3.4300	0.029	0.018	0.018
ScanPos003	431185.3857	5222792.4340	2.6763	0.045	0.043	0.018

4.3 Changes in Scan Positions

The following table reflects the change of scan positions with respect to position and orientation in comparison to positions and orientations wrt to prior to multi-station adjustment.

In the PRCS coordinate system:

Changes wrt to prior to multi-station adjustment						
Name	X [m]	Y [m]	Z [m]	Roll [deg]	Pitch [deg]	Yaw [deg]
ScanPos001	0.1963	-0.0162	0.0006	-0.0022	-0.0114	0.1451
ScanPos002	-0.0885	0.0286	0.0112	0.0027	0.0051	0.0542
ScanPos003	0.0997	-0.1910	0.0124	-0.0018	0.0004	-0.2310

Figure 73. Page 4 of the MSA report from the TLS (at Mustang Island State Park).

4.4 Residuals

For an assessment of the quality of the multi-station adjustment the following residual deviations (in short residuals) can be observed.

4.4.1 GNSS Measurements

Name	Deviations in PRCS			a priori Accuracies	
	Res. X [m]	Res. Y [m]	Res. Z [m]	Horiz. [m]	Vert. [m]
ScanPos001*	0.0156	-0.0646	0.0561	0.014	0.015
ScanPos002	-0.0085	-0.0077	0.0129	0.014	0.014
ScanPos003	0.0084	0.0076	-0.0124	0.014	0.014

* ... Observation classified as outlier that has not been used for adjustment

Statistics	mean	median	std. dev.	std(mad)	min	max	count
Res. X [m]	-0.0001	-0.0001	0.0085	0.0126	-0.0085	0.0084	2
Res. Y [m]	-0.0000	-0.0000	0.0077	0.0114	-0.0077	0.0076	2
Res. Z [m]	0.0003	0.0003	0.0127	0.0188	-0.0124	0.0129	2
Res. X [l]	-0.004	-0.004	0.601	0.890	-0.604	0.597	2
Res. Y [l]	-0.003	-0.003	0.546	0.809	-0.549	0.542	2
Res. Z [l]	0.012	0.012	0.924	1.370	-0.912	0.936	2
Res. X with outlier [m]	0.0052	0.0084	0.0101	0.0107	-0.0085	0.0156	3
Res. Y with outlier [m]	-0.0216	-0.0077	0.0311	0.0228	-0.0646	0.0076	3
Res. Z with outlier [m]	0.0189	0.0129	0.0283	0.0375	-0.0124	0.0561	3
Res. X with outlier [l]	0.367	0.597	0.718	0.758	-0.604	1.108	3
Res. Y with outlier [l]	-1.530	-0.549	2.205	1.618	-4.584	0.542	3
Res. Z with outlier [l]	1.239	0.936	1.891	2.740	-0.912	3.692	3

4.4.2 Orientation Measurements

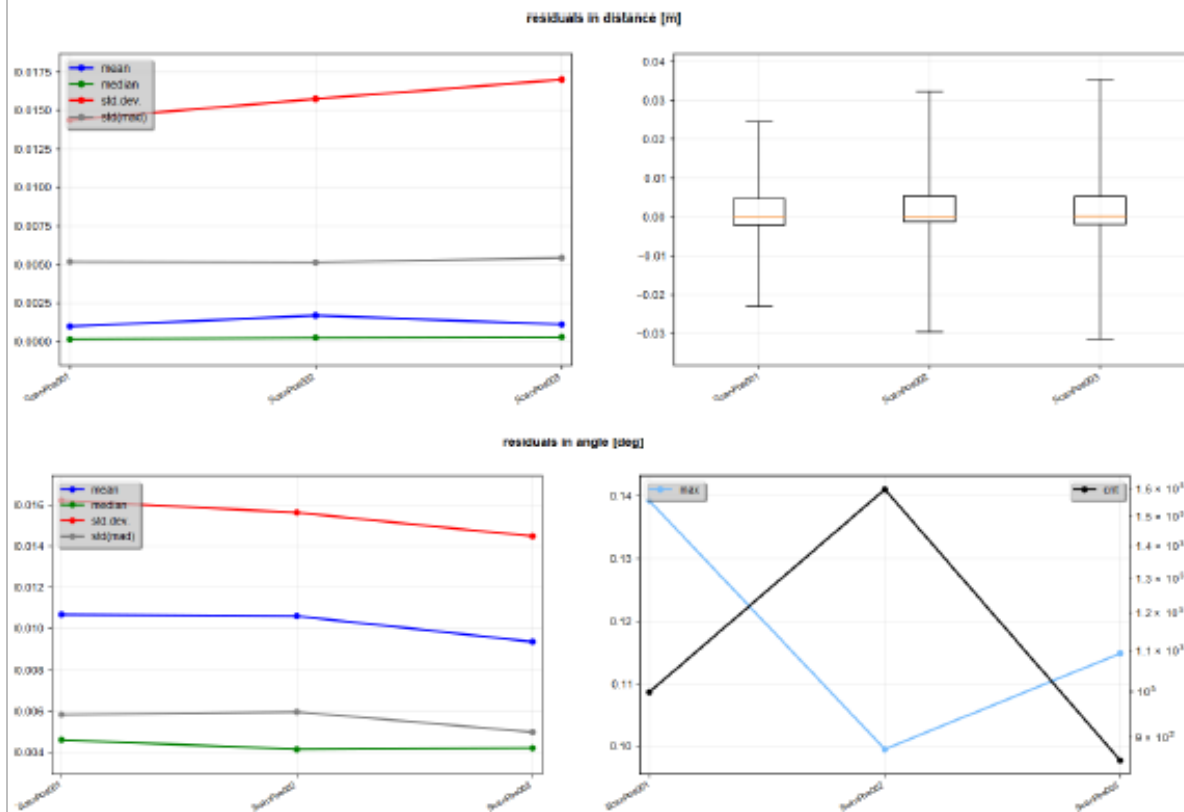
	Deviations in PRCS			a priori Accuracies			
Name	Roll [deg]	Pitch [deg]	Yaw [deg]	Roll [deg]	Pitch [deg]	Yaw [deg]	
ScanPos001	0.0025	-0.0167	-6.9246	0.011	0.011	10.000	
ScanPos002	0.0036	0.0008	-7.6008	0.011	0.011	10.000	
ScanPos003	-0.0046	0.0046	-7.8264	0.011	0.011	10.000	
Statistics	mean	median	std. dev.	std(mad)	min	max	count
Roll [deg]	0.0005	0.0025	0.0036	0.0016	-0.0046	0.0036	3
Pitch [deg]	-0.0038	0.0008	0.0093	0.0056	-0.0167	0.0046	3
Yaw [deg]	-7.4506	-7.6008	0.3832	0.3346	-7.8264	-6.9246	3
Roll [l]	0.043	0.224	0.342	0.175	-0.436	0.342	3
Pitch [l]	-0.325	0.077	0.834	0.530	-1.486	0.435	3
Yaw [l]	-0.745	-0.760	0.038	0.033	-0.783	-0.692	3

Figure 74. Page 5 of the MSA report from the TLS (at Mustang Island State Park).

4.4.3 Plane Patches

The subsequent figures show the residuals in distance and angle of all plane patches per scan position, expressed as mean, median, standard deviation and median absolute deviation (std(mad)). Additionally, the figures depict the number of plane patches available for every scan position.

For the residuals in distance of the plane patches the boxplot shows the median as orange line. The box is defined by the quantil 25% and 75%. This translates to 50 percent of the total amount of points lie in the range shown by the box. The whiskers are at the quantil 2.5% and 97.5%, containing 95% of all points.



Plane Patch Residuals of Distance [m]											
Name	# plane patches	mean	median	std. dev.	std(mad)	min	q2.5%	q25%	q75%	q97.5%	max
ScanPos001	999	0.0010	0.0001	0.0144	0.0052	-0.2373	-0.0230	-0.0021	0.0048	0.0245	0.1029
ScanPos002	1597	0.0017	0.0002	0.0157	0.0051	-0.1622	-0.0295	-0.0012	0.0054	0.0323	0.1633
ScanPos003	853	0.0011	0.0003	0.0170	0.0054	-0.1484	-0.0314	-0.0019	0.0053	0.0353	0.1714

Plane Patch Angular Residuals [deg]											
Name	# plane patches	mean	median	std. dev.	std(mad)	min	q2.5%	q25%	q75%	q97.5%	max
ScanPos001	999	0.0107	0.0046	0.0162	0.0058	0.0000	0.0000	0.0014	0.0126	0.0665	0.1392
ScanPos002	1597	0.0106	0.0042	0.0156	0.0060	0.0000	0.0000	0.0007	0.0131	0.0611	0.0995
ScanPos003	853	0.0094	0.0042	0.0145	0.0050	0.0000	0.0000	0.0015	0.0106	0.0593	0.1149

Figure 75. Page 6 of the MSA report from the TLS (at Mustang Island State Park).

APPENDIX H

UAS GENERATED DTMS, ORTHOMOSAICS, AND POINT CLOUDS

DTMs, orthomosaics, and point clouds for North Packery Channel using different software.

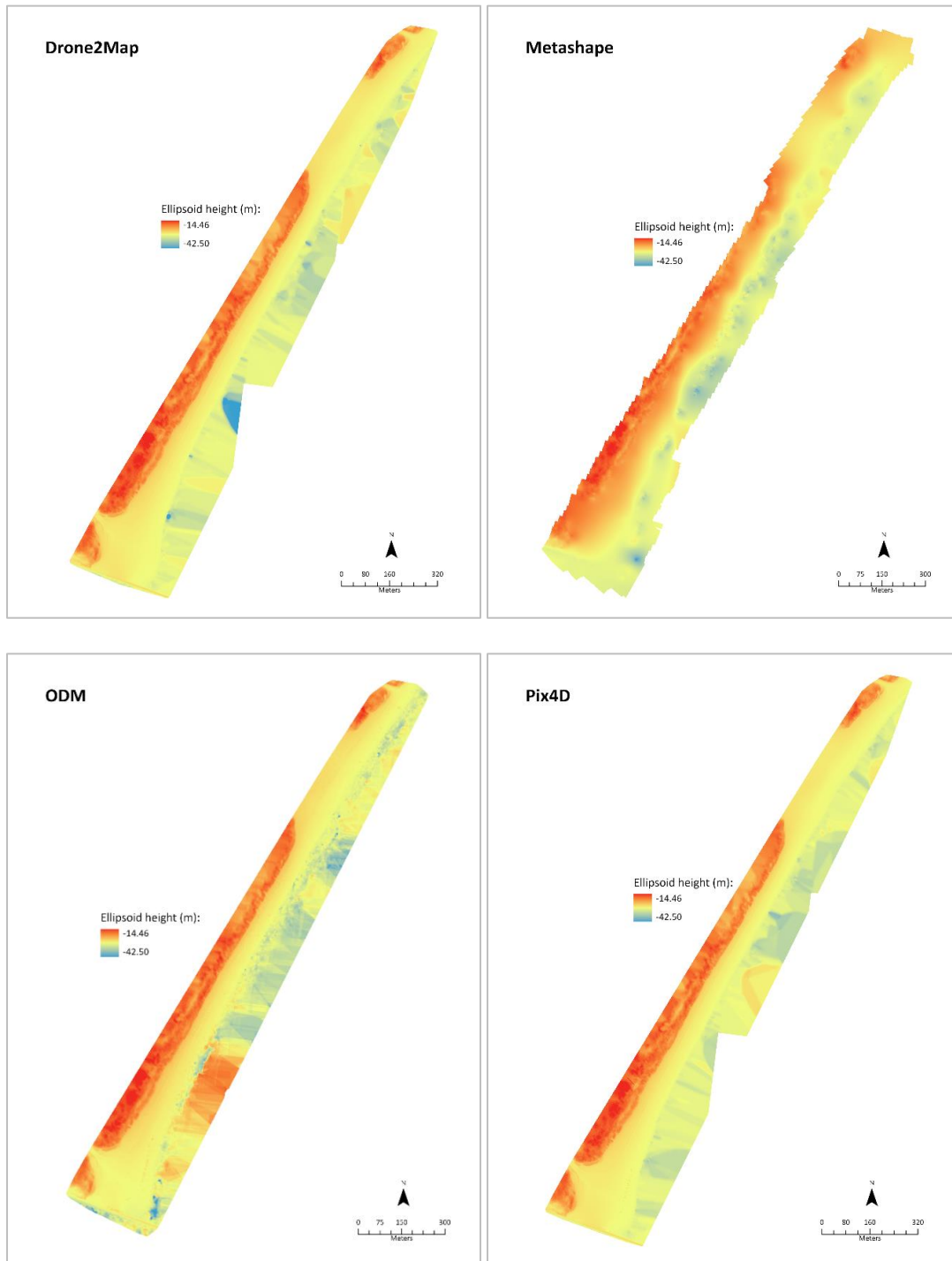


Figure 76. North Packery Channel DTMs (WingtraOne UAS dataset at 100 m AGL).

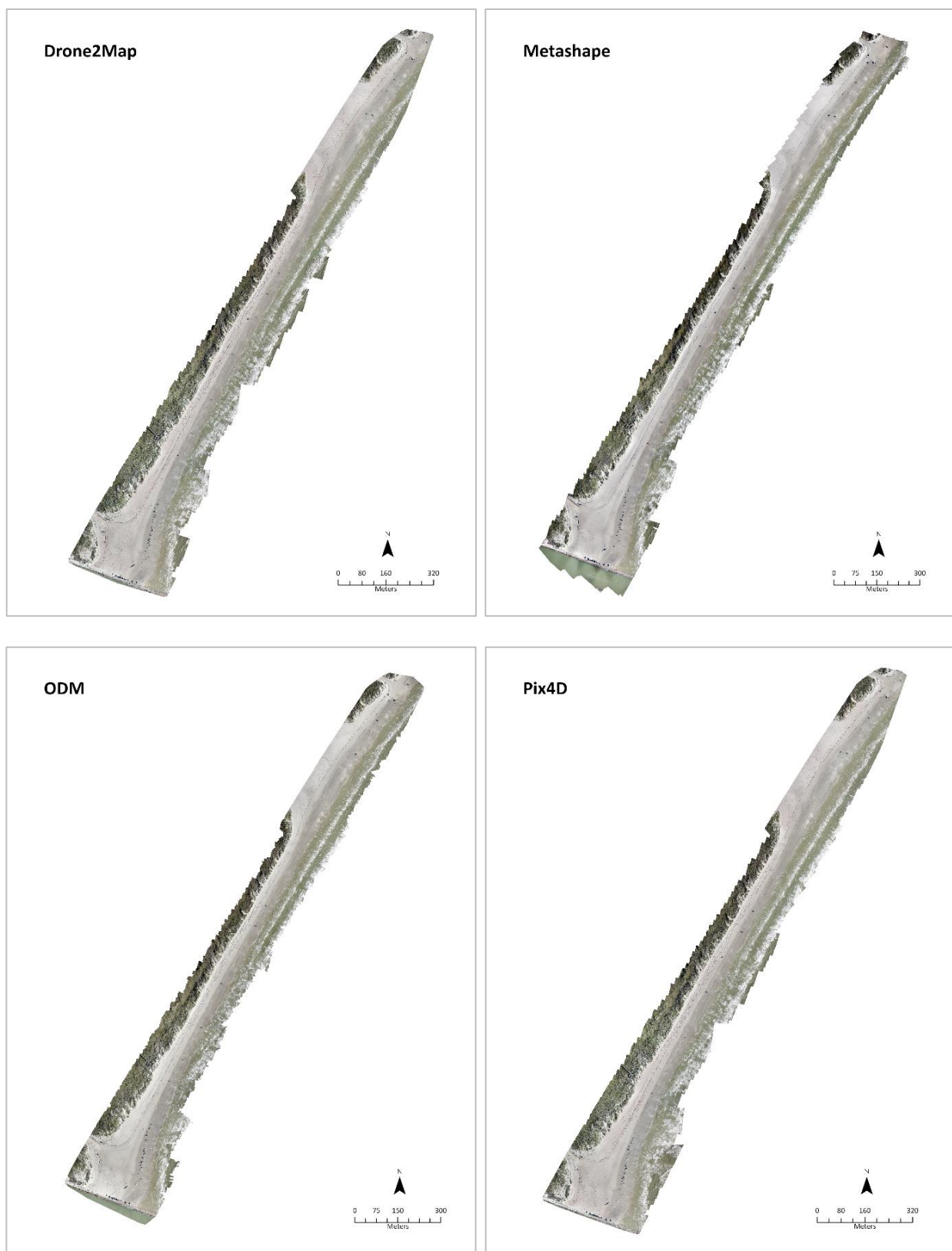


Figure 77. North Packery Channel orthomosaics (WingtraOne UAS dataset at 100 m AGL).

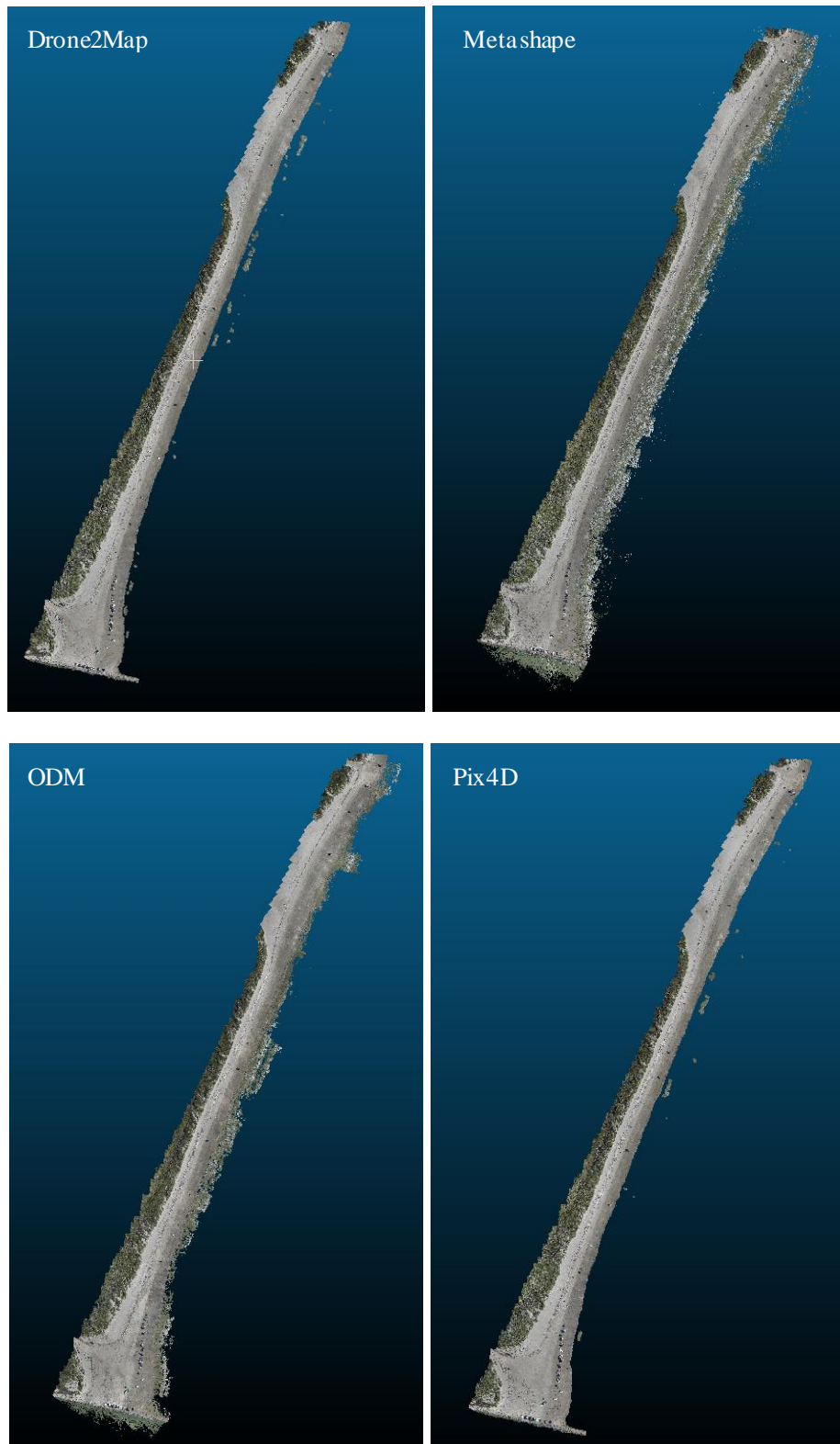


Figure 78. North Packery Channel point clouds (WingtraOne UAS dataset at 100 m AGL, screenshot from CloudCompare).

DTMs, orthomosaics, and point clouds for Mustang Island State Park using different software.

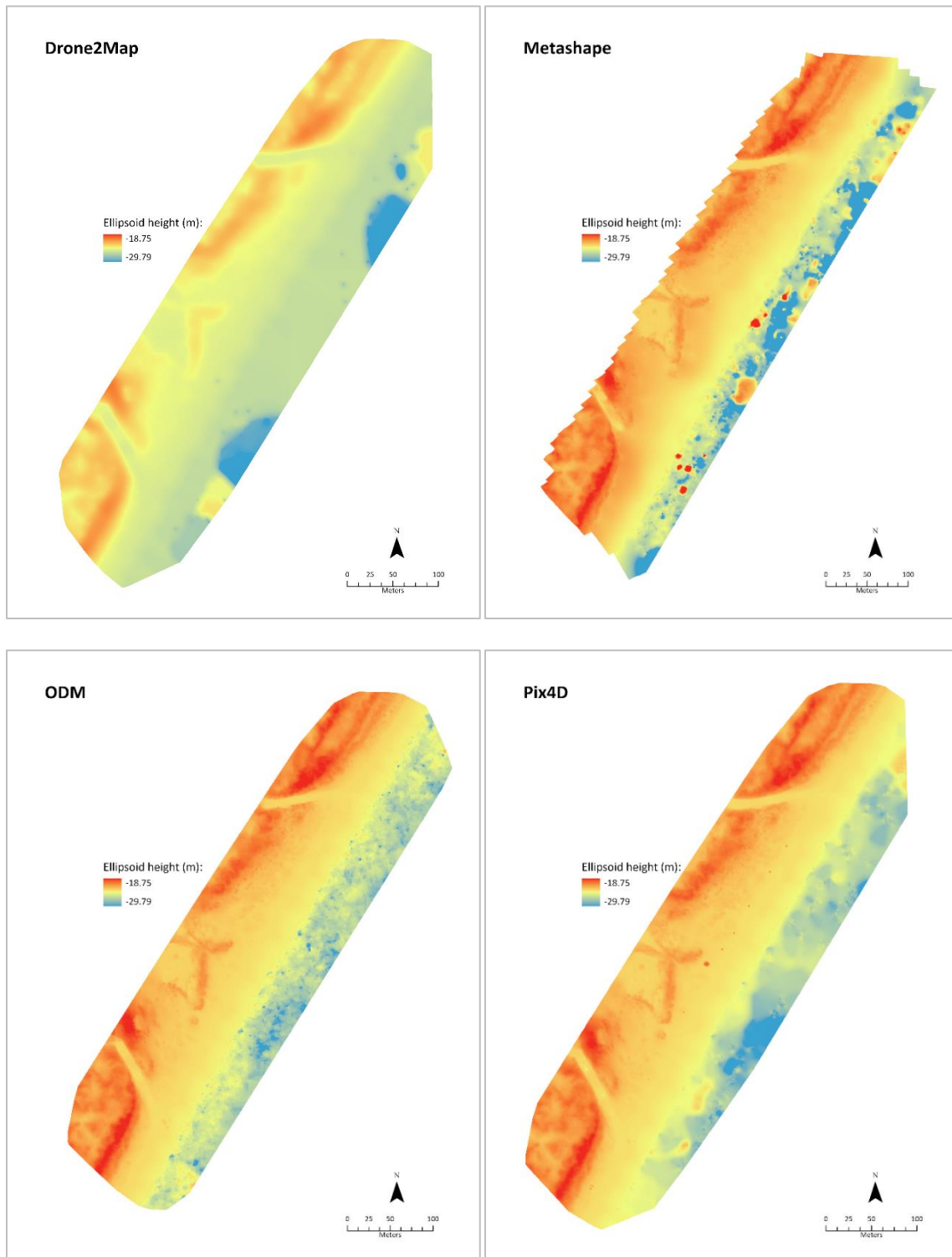


Figure 79. Mustang Island State Park DTMs (WingtraOne UAS dataset at 75 m AGL).

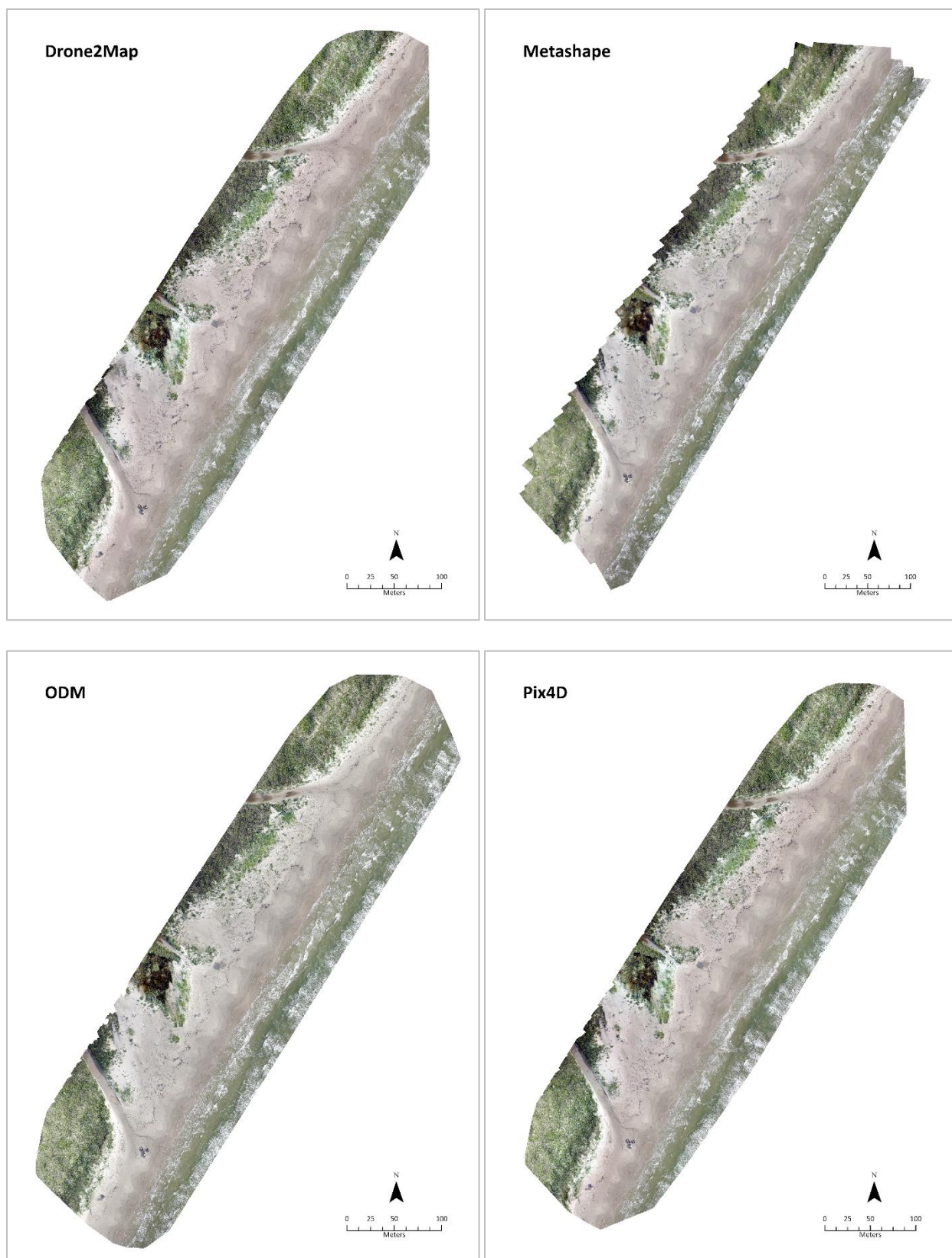


Figure 80. Mustang Island State Park orthomosaics (WingtraOne UAS dataset at 75 m AGL).

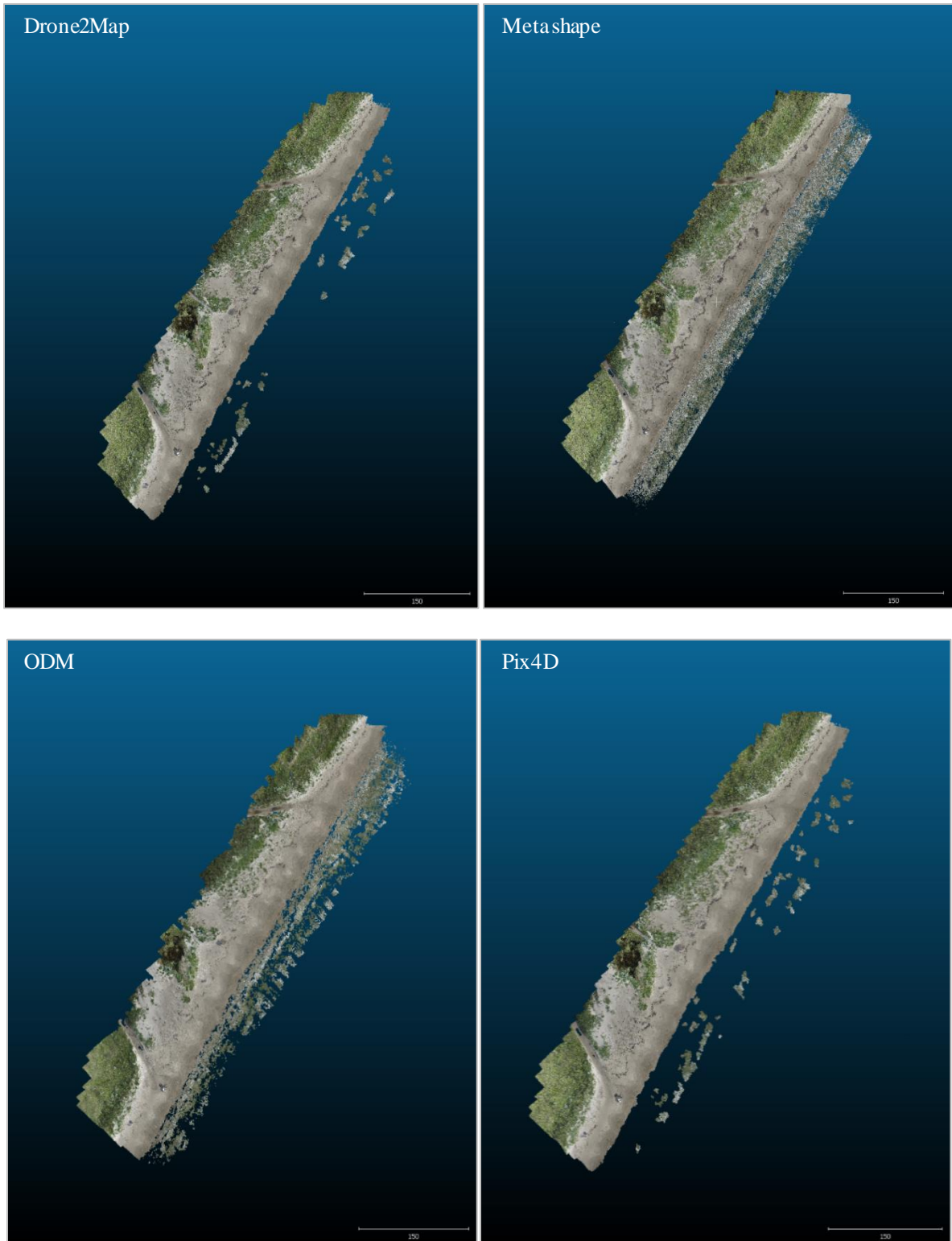


Figure 81. Mustang Island State Park point clouds (WingtraOne UAS dataset at 75 m AGL, screenshot from CloudCompare).

APPENDIX I

PROCESSING REPORTS FROM SFM SOFTWARE

Note that no accurate report is available for ODM when using checkpoints, as discussed throughout this thesis.

Checkpoint accuracy results from processing reports using the tested SfM software.

Geolocation Details						
Ground Control Points						
0 out of 25 check points have been labeled as inaccurate.						
Check Point Name	Accuracy XYZ [m]	Error X [m]	Error Y [m]	Error Z [m]	Projection Error [pixel]	Verified/Marked
GCPT1		0.908	-0.455	0.121	0.514	6 / 6
GCPT10		0.908	-0.441	0.113	0.402	5 / 5
GCPT11		0.912	-0.436	0.117	0.545	5 / 6
GCPT12		0.909	-0.436	0.143	0.423	5 / 5
GCPT13		0.921	-0.431	0.128	0.597	5 / 5
GCPT14		0.919	-0.436	0.138	0.367	5 / 5
GCPT15		0.910	-0.431	0.154	0.417	5 / 5
GCPT16		0.914	-0.439	0.104	0.330	5 / 5
GCPT17		0.915	-0.438	0.126	0.326	6 / 6
GCPT18		0.909	-0.435	0.115	0.510	6 / 6
GCPT19		0.914	-0.432	0.126	0.334	5 / 5
GCPT2		0.911	-0.458	0.137	0.358	5 / 5
GCPT20		0.907	-0.409	0.146	0.461	5 / 5
GCPT21		0.939	-0.423	0.134	0.460	6 / 6
GCPT22		0.927	-0.400	0.105	0.409	6 / 6
GCPT23		0.932	-0.394	0.123	0.410	6 / 6
GCPT24		0.922	-0.402	0.115	0.532	5 / 5
GCPT25		0.931	-0.398	0.128	0.401	5 / 5
GCPT3		0.905	-0.448	0.138	0.420	5 / 5
GCPT4		0.905	-0.449	0.111	0.417	6 / 6
GCPT5		0.907	-0.460	0.119	0.373	6 / 6
GCPT6		0.901	-0.450	0.109	0.357	5 / 5
GCPT7		0.904	-0.444	0.122	0.485	5 / 5
GCPT8		0.910	-0.443	0.128	0.461	6 / 6
GCPT9		0.903	-0.443	0.138	0.452	5 / 5
Mean [m]		0.913733	-0.433189	0.125630		
Sigma [m]		0.009717	0.018531	0.012962		
RMS Error [m]		0.913785	0.433585	0.126297		
Localisation accuracy per GCP and mean errors in the three coordinate directions. The last column counts the number of calibrated images where the GCP has been automatically verified vs. manually marked.						

Figure 82. Checkpoint accuracies from Drone2Map processing report (uses Mustang Island State Park local base at 1s, WingtraOne UAS at 75 m AGL). RMSEs relative to total station checkpoints.

Label	X error (cm)	Y error (cm)	Z error (cm)	Total (cm)	Image (pix)
GCPT1	-0.554175	-0.0440115	6.49489	6.51864	0.116 (6)
GCPT2	-0.935763	0.533347	7.00771	7.09	0.219 (5)
GCPT3	-0.56857	-0.442122	6.0807	6.12321	0.217 (5)
GCPT4	-0.322368	-0.520345	6.48277	6.5116	0.111 (7)
GCPT5	-0.348255	0.56724	6.79298	6.82551	0.223 (6)
GCPT6	0.0180948	-0.476271	5.59436	5.61463	0.175 (6)
GCPT7	0.0358535	-1.03518	6.0848	6.17233	0.206 (7)
GCPT8	-0.491383	-1.21665	6.22609	6.36285	0.154 (7)
GCPT9	0.204293	-1.04168	6.30527	6.39401	0.139 (8)
GCPT10	-0.471868	-1.14915	6.74535	6.85879	0.169 (7)
GCPT11	-0.603235	-1.66329	5.98797	6.2439	0.193 (6)
GCPT12	-0.202013	-1.76322	7.05439	7.27422	0.165 (8)
GCPT13	-1.40277	-2.48884	6.57209	7.1662	0.179 (6)
GCPT14	-1.21736	-2.41443	6.2186	6.78104	0.216 (7)
GCPT15	-0.0914248	-2.55341	6.59345	7.0712	0.157 (8)
GCPT16	-0.699099	-2.29024	6.0239	6.48238	0.162 (6)
GCPT17	-0.682087	-2.46638	6.35204	6.84812	0.182 (7)
GCPT18	0.210601	-3.0623	6.59098	7.2707	0.211 (6)
GCPT19	-0.643684	-3.15066	6.65633	7.39241	0.162 (7)
GCPT21	-3.05205	-4.1222	6.50363	8.28279	0.219 (6)
GCPT20	0.162865	-5.41902	7.12048	8.9495	0.142 (6)
GCPT22	-1.78692	-6.29461	6.17731	8.99857	0.204 (7)
GCPT23	-2.26303	-6.60352	8.12694	10.7133	0.209 (6)
GCPT24	-0.984048	-6.64995	6.86419	9.60766	0.169 (7)
GCPT25	-1.97775	-6.82526	6.53243	9.65237	0.173 (8)
Total	1.09636	3.3568	6.54558	7.43739	0.180

Figure 83. Checkpoint accuracies from Metashape processing report (uses Mustang Island State Park local base at 1s, WingtraOne UAS at 75 m AGL). RMSEs relative to total station checkpoints.

Geolocation Details

Ground Control Points

0 out of 25 check points have been labeled as inaccurate.

Check Point Name	Accuracy XY/Z [m]	Error X[m]	Error Y[m]	Error Z[m]	Projection Error [pixel]	Verified/Marked
GCPT1		0.010	0.010	-0.054	0.358	6 / 6
GCPT2		0.011	0.003	-0.046	0.281	5 / 5
GCPT3		0.008	0.010	-0.048	0.348	6 / 6
GCPT4		0.005	0.011	-0.043	0.347	6 / 6
GCPT5		0.003	0.005	-0.037	0.168	5 / 5
GCPT6		-0.000	0.010	-0.054	0.303	6 / 6
GCPT7		-0.001	0.016	-0.048	0.477	4 / 4
GCPT8		0.005	0.014	-0.049	0.330	5 / 5
GCPT9		-0.001	0.012	-0.041	0.311	6 / 6
GCPT10		0.003	0.014	-0.042	0.281	5 / 5
GCPT11		0.004	0.021	-0.040	0.225	5 / 5
GCPT12		0.002	0.020	-0.052	0.438	5 / 5
GCPT13		0.014	0.024	-0.041	0.249	5 / 5
GCPT14		0.010	0.024	-0.059	0.261	5 / 5
GCPT15		0.003	0.023	-0.056	0.330	6 / 6
GCPT16		0.004	0.020	-0.053	0.235	6 / 6
GCPT17		0.004	0.021	-0.044	0.202	5 / 5
GCPT18		-0.002	0.028	-0.054	0.494	5 / 5
GCPT19		0.005	0.024	-0.047	0.300	5 / 5
GCPT21		0.030	0.039	-0.071	0.320	6 / 6
GCPT20		-0.002	0.050	-0.056	0.603	5 / 5
GCPT22		0.020	0.058	-0.068	0.239	6 / 6
GCPT23		0.024	0.059	-0.074	0.127	5 / 5
GCPT24		0.009	0.064	-0.060	0.367	5 / 5
GCPT25		0.019	0.066	-0.062	0.365	6 / 6
Mean [m]		0.007467	0.025783	-0.051995		
Sigma [m]		0.008120	0.018553	0.009589		
RMS Error [m]		0.011032	0.031764	0.052872		

Localisation accuracy per GCP and mean errors in the three coordinate directions. The last column counts the number of calibrated images where the GCP has been automatically verified vs. manually marked.

Figure 84. Checkpoint accuracies from Pix4D processing report (uses Mustang Island State Park local base at 1s, WingtraOne UAS at 75 m AGL). RMSEs relative to total station checkpoints.